Investigating a PROTAC approach to NRF2 activation

William Robinson

University of East Anglia
School of Chemistry, Pharmacy and Pharmacology
2025

This Thesis is Submitted for the Degree of Master of Science by Research

Student number: 100301594

Abstract

Nuclear factor erythroid-2 related factor 2 (NRF2) is a transcription factor central to cellular defence against oxidative stress and inflammation. Under basal conditions, NRF2 is constitutively degraded by Kelch-like ECH-associated protein 1 (Keap1), which facilitates NRF2 ubiquitination and proteasomal degradation. Disruption of the Keap1-NRF2 protein-protein interaction (PPI) stabilises NRF2, allowing for nuclear accumulation and binding to the antioxidant response element of genes, including heme oxygenase-1 (HO-1) and NAD(P)H quinone dehydrogenase 1 (NQO1) amongst others. Small molecules and peptide-based protein-protein interaction (PPI) inhibitors targeting this pathway have demonstrated anti-inflammatory activity *in vitro* and *in vivo*. TAT-14, a previously reported peptide PPI inhibitor, binds Keap1 with nanomolar affinity and upregulates NRF2/ARE genes. More recently, proteolysis-targeting chimeras (PROTACs) have emerged as a novel strategy to activate NRF2 by degrading Keap1, offering enhanced potency, selectivity and duration of action compared to PPI inhibitors and small molecules.

In this project, TAT-14 was synthesised by Fmoc solid-phase peptide synthesis and confirmed to increase NRF2 protein expression and induce HO-1 and NQO1 mRNA expression with minimal cytotoxicity, consistent with previous reports. TAT-14 was therefore employed in PROTAC design to function as the Keap1-binding warhead. The VHL-recruiting ligand VH032 was successfully synthesised and linker optimisation enabled conjugation in PROTAC development. Synthesis of PROTAC1, which incorporated a PEG linker, was unsuccessful, whereas replacement with a glutaric anhydride-derived alkyl linker yielded PROTAC2 which was purified and characterised. *In vitro*, PROTAC2 elicited greater HO-1 and NQO1 mRNA induction than TAT-14, although with notable cytotoxicity found. These findings provide evidence that Keap1-targeting peptide PPI inhibitors can be adapted to PROTAC design to activate NRF2, although further studies are required to confirm robust NRF2 activation through Keap1 degradation.

Access Condition and Agreement

Each deposit in UEA Digital Repository is protected by copyright and other intellectual property rights, and duplication or sale of all or part of any of the Data Collections is not permitted, except that material may be duplicated by you for your research use or for educational purposes in electronic or print form. You must obtain permission from the copyright holder, usually the author, for any other use. Exceptions only apply where a deposit may be explicitly provided under a stated licence, such as a Creative Commons licence or Open Government licence.

Electronic or print copies may not be offered, whether for sale or otherwise to anyone, unless explicitly stated under a Creative Commons or Open Government license. Unauthorised reproduction, editing or reformatting for resale purposes is explicitly prohibited (except where approved by the copyright holder themselves) and UEA reserves the right to take immediate ‘take down’ action on behalf of the copyright and/or rights holder if this Access condition of the UEA Digital Repository is breached. Any material in this database has been supplied on the understanding that it is copyright material and that no quotation from the material may be published without proper acknowledgement.

Table of Contents

2.3 – TAT 14 *in vitro* Assays

2.10 – Chemical Methods

Supporting Data

List of Figures

List of Tables

Abbreviations

A20	TNF-α-induced protein 3
AD	Alzheimer's disease
AJ	Adherens junction
AKT	Protein kinase B
AML12	Alpha mouse liver 12 cell line
APAP	Acetaminophen
AR	Androgen receptor
ARE	Antioxidant response element
AUC_{last}	Area Under the Curve to the Last measurable concentration
BCL-XL	B-cell lymphoma-extra large
BET	Bromodomain and extra-terminal family
Boc	*Tert*-butyloxycarbonyl protecting group
Boc_2O	Di-*tert*-butyl dicarbonate
BRD4	Bromodomain-containing protein 4
BTB	Broad-complex Tramtrack Bric-à-brac domain
BTK	Bruton's tyrosine kinase
bZip	Basic leucine zipper
CAMs	Cell adhesion molecules
CAT	Catalase
CBP	CREB-binding protein
CDDO	2-Cyano-3,12-dioxooleana-1,9-dien-28-oic acid
CDDO-Im	CDDO-imidazolide
CDDO-Me	CDDO-methyl ester
CH_2Cl_2	Dichloromethane
ChIP	Chromatin immunoprecipitation
CKD	Chronic kidney disease
CLI	Cholestatic liver injury
C_{max}	Maximum observed plasma concentration
CNC	Cap 'n' collar transcription factor

CNS	Central nervous system
CO	Carbon monoxide
COX	Cyclo-oxygenase
CPP	Cell-penetrating peptide
CPP9	Cell-penetrating peptide 9
CRBN	Cereblon
CRL	Cullin-RING ligase
CTR	C-terminal region
CUL1	Cullin-1
CUL2	Cullin-2
CUL3	Cullin-3
CUL4	Cullin-4
CXA-10	10-nitro-oleic acid
CXCL8/IL-8	Interleukin 8
DAMPs	Damage-associated molecular patterns
DC_{50}	Half-maximal degradation concentration
DDB1	DNA damage-binding protein 1
DIDLID	Keap1-binding degron motif
DIPEA	*N,N*-diisopropylethylamine
DMAc	*N,N*-dimethylacetamide
DMF	Dimethyl fumarate / *N,N*-dimethylformamide
DMSO	Dimethyl sulphoxide
DUB	Deubiquitinating enzyme
E1	Ubiquitin-activating enzyme
E2	Ubiquitin-conjugating enzyme
E3	Ubiquitin ligase
EC_{50}	Half-maximal effective concentration
EpRE	Electrophile response element
ER	Estrogen receptor / Endoplasmic reticulum
EtOAc	Ethyl acetate
Fmoc	9-fluorenylmethyloxycarbonyl
FP	Fluorescence polarisation
GI	Gastrointestinal

GPX	Glutathione peroxidase
GSH	Reduced glutathione
GSK-3β	Glycogen synthase kinase-3 beta
GSR	Glutathione reductase
GST	Glutathione S-transferase
HATU	*O*-(7-azabenzotriazol-1-yl)-*N,N,N’,N’*-tetramethyluronium hexafluorophosphate
HBTU	*O*-(benzotriazol-1-yl)-*N,N,N’,N’*-tetramethyluronium hexafluorophosphate
HCl	Hydrochloric acid
HIF-1α	Hypoxia-inducible factor-1 alpha
HOBt	1-Hydroxybenzotriazole
HO-1	Heme oxygenase-1
HRD1	Hydroxymethylglutaryl-coenzyme A reductase degradation protein 1
HRP	Horseradish peroxidase
HPLC	High-performance liquid chromatography
HTRF	Homogeneous time-resolved fluorescence assay
IBD	Inflammatory bowel disease
IC_{50}	Half-maximal inhibitory concentration
IFN-γ	Interferon-gamma
IKKβ	IκB kinase beta
IL	Interleukin
IMiDs	Immunomodulatory imide drugs
ITC	Isothermal titration calorimetry
IκBα	Inhibitor of κB alpha
K_d	Dissociation constant
KD (mice)	Knockdown mice
KCN	Potassium cyanide
KLHL11	Kelch-like protein 11
KO (mice)	Knockout mice
Keap1	Kelch-like ECH-associated protein 1

LPS	Lipopolysaccharide
MAPK	Mitogen-activated protein kinase
MEFs	Mouse embryonic fibroblasts
MeOH	Methanol
MetAP-2	Methionine aminopeptidase-2
$MgSO_4$	Magnesium sulphate
MMF	Monomethyl fumarate
MMP-12	Matrix metalloproteinase-12
mAbs	Monoclonal antibodies
mCRPC	Metastatic castration-resistant prostate cancer
mRNA	Messenger RNA
NETs	Neutrophil extracellular traps
NF-κB	Nuclear factor κB
NLRP3	NLR family-pyrin domain-containing protein 3
NMP	*N*-methyl-2-pyrrolidone
NOX	NADPH oxidase
NQO1	NAD(P)H quinone dehydrogenase 1
NRF2	Nuclear factor erythroid 2-related factor 2
NSAIDs	Non-steroidal anti-inflammatory drugs
PAMPs	Pathogen-associated molecular patterns
$Pd(OAc)_2$	Palladium(II) acetate
PDB	Protein Data Bank
PEG	Polyethylene glycol
PI3K	Phosphoinositide 3-kinase
PK	Pharmacokinetics
POI	Protein of interest
PPI	Protein-protein interaction
PROTAC	Proteolysis targeting chimera
PRR	Pattern-recognition receptor
PVDF	Polyvinylidene difluoride
RBX1	RING-box protein 1
RING	Really Interesting New Gene

RNS	Reactive nitrogen species
ROS	Reactive oxygen species
RPM	Revolutions per minute
RRMS	Relapsing–remitting multiple sclerosis
RTA-408	Omaveloxolone
RT	Room temperature
RXRα	Retinoid X receptor alpha
SAR	Structure-activity relationship
SCI	Systemic chronic inflammation
SOD	Superoxide dismutase
SPMs	Specialised pro-resolving mediators
SPR	Surface plasmon resonance
STAT3	Signal transducer and activator of transcription 3
sMaf	Small Maf protein
TAT	Trans-activator of transcription
TFA	Trifluoroacetic acid
TGF-β	Transforming growth factor-beta
TIPS	Triisopropylsilane
TJ	Tight junction
TNF-α	Tumor necrosis factor-alpha
$T_{1/2}$	Elimination half-life
TXN	Thioredoxin
UC	Ulcerative colitis
UPF	Ultra-processed food
UPS	Ubiquitin-proteasome system
VHL	von Hippel-Lindau protein
WDR23	WD repeat-containing protein 23
WGS	Whole-genome sequencing
WT	Wild type
ZFP91	Zinc finger protein 91
β-TrCP	β-transducin repeat-containing protein

Acknowledgements

I could not have completed this project without the support from Prof Maria O'Connell and Prof Mark Searcey who were brilliant throughout my time at UEA. Maria and the biology research team, especially Dr Emily Hobson, Emilia and Dasha, were a pleasure to work with and went above and beyond. I would also like to thank the Searcey and Beekman chemistry research groups, who were very welcoming and supportive. I am especially thankful to the PhD students Vicky Kamperi, Ellie Hyde and Owen Mullen, who went out of their way to help me with all aspects as a researcher. Finally, I would like to finally thank everyone in the School of Chemistry, Pharmacy and Pharmacology at UEA for their kindness, support and for making the experience worthwhile!

Chapter 1 Introduction

1.1 Inflammation and Oxidative Stress

1.1.1 The Inflammatory Response

The human immune system has evolved to mount an inflammatory response as a defence mechanism against harmful threats. Upon detection, the innate immune system mediates a rapid acute inflammatory response to eliminate the threat. If insufficient, the adaptive immune system contributes through a more targeted and sustained response [1]. However, when inflammation becomes dysregulated or persists, it can contribute to tissue damage and chronic inflammation. This is characterised by sustained immune cell activation and pro-inflammatory signalling, allowed to continue unchecked. This persistent tissue damage contributes to the onset and progression of various neurodegenerative, metabolic and cardiovascular diseases, which account for over 50% of deaths globally [2] [3]. For example, chronic kidney disease (CKD) is estimated to impact 11% of the global population [4], while inflammatory bowel disease (IBD) affected over 2.4 million people in the USA in 2023 alone, with incidence rates rising [5].

The acute inflammatory response is triggered through recognition of invading pathogens, tissue injury, exogenous toxins or pollutants. These stimuli express pathogen-associated molecular patterns (PAMPs) or host-derived damage-associated molecular patterns (DAMPs), which are recognised by monocytes, macrophages, dendritic cells and neutrophils through pattern recognition receptors (PRRs) [6]. PRRs transduce signals intracellularly through nuclear factor kappa B (NF-κB), mitogen-activated protein kinase (MAPK) and inflammasome pathways. This leads to the release of pro-inflammatory cytokines such as tumour necrosis factor-α (TNF-α), interleukin-1β (IL-1β), interleukin-6 (IL-6) and interferon-γ (IFN-γ) which drive the response through extracellular signalling [6] [7] [8]. Various cell types and cytokines participate in driving the inflammatory response (**Figure 1.1**). Cytokines bind endothelial cells which upregulate cell adhesion molecules (CAMs) on the cell surface. Concurrently, endothelial tight junctions (TJs) and adherens junctions (AJs) are disrupted, increasing cell permeability. This allows for the adhesion and transmigration of recruited leukocytes to the site of inflammation [9]. Neutrophils arrive first and constitute most recruited leukocytes. This is driven by interleukin-8 (IL-8/CXCL8), a potent neutrophil chemoattractant and activator [10] [11]. Activated neutrophils phagocytose the inciting target and produce reactive oxygen species (ROS), catalysed by NADPH oxidase (NOX) enzymes, which contributes to destruction of the inciting threat [12]. Monocytes arrive subsequently and differentiate into macrophages which also undergo phagocytosis and generate ROS. Intracellularly, ROS is beneficial for target destruction but extracellularly it can elevate oxidative stress and cause tissue damage, which will be discussed subsequently [13].

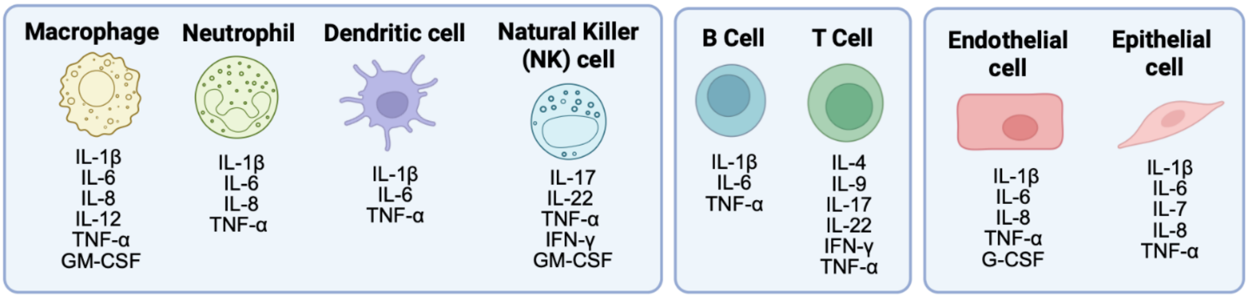

***Figure 1.1** Various cell types and associated key cytokines released during inflammation, including innate immune cells (left), adaptive immune cells (middle) and structural cells (right)* [14] [15] [16].

Pro-inflammatory signalling, through further leukocyte recruitment and cytokine release, is allowed to continue until the threat is removed. Removal of the inciting target suppresses DAMP/PAMP signalling, in turn dampening further cytokine and chemokine release. This triggers a series of events which actively promote a shift in signalling, from pro-inflammatory to anti-inflammatory [17]. IL-8/CXCL8 downregulation, mediated by macrophage matrix metalloproteinase-12 (MMP-12) cleavage, halts further neutrophil recruitment [18]. Activated neutrophils undergo apoptosis and are engulfed by macrophages via efferocytosis. Macrophages subsequently undergo a phenotypic shift from a pro-inflammatory M1, to an anti-inflammatory M2 transcriptional state. This results in the release of the cytokines IL-10 and TGF-β along with specialised pro-resolving mediators (SPMs), which promote resolution and tissue repair [19] [20]. SPMs, including lipoxins, resolvins and maresins, constitute a family of bioactive lipids that actively suppress leukocyte recruitment, ROS production and pro-inflammatory cytokine release [21] [22]. In parallel, the growth factor transforming growth factor-β (TGF-β) promotes fibroblast proliferation and angiogenesis, promoting tissue repair [23]. Macrophages finally undergo apoptosis or re-enter circulation, allowing tissue function to return, restoring homeostasis [24].

1.1.2 Chronic Inflammation and Disease

Acute inflammation is typically a protective, tightly regulated innate response which ultimately resolves. Failure of resolution or trigger persistence can result in chronic inflammation which is characterised by sustained M1 macrophage activation, elevated oxidative stress and continuous cytokine release. While short-lived in acute inflammation, the lifespan of neutrophils is extended, further contributing to ROS oxidative damage [25]. Cross-talk with the adaptive immune system amplifies the response, with T-cell recruitment implicated in the pathogenesis of several chronic disorders including hepatic, cardiovascular and inflammatory bowel diseases [26].

Inflammation is identified as a key driver in numerous diseases which affect various systems across the body (**Figure 1.2**). Amongst these diseases, cardiovascular disease (CVD) is a leading cause of deaths globally [27]. Central to pathogenesis is atherosclerosis, a chronic inflammatory disorder characterised by the accumulation of plaques within arterial walls alongside immune cell infiltration. M1 macrophages promote plaque formation and release cytokines, while neutrophils generate extracellular traps (NETs) which oxidise lipids, damage endothelium and further exacerbate plaque formation [28] [25]. Chronic hepatic inflammation similarly contributes to liver disease by hepatic M1 macrophage activation, which positively correlates with disease severity [29] [30].

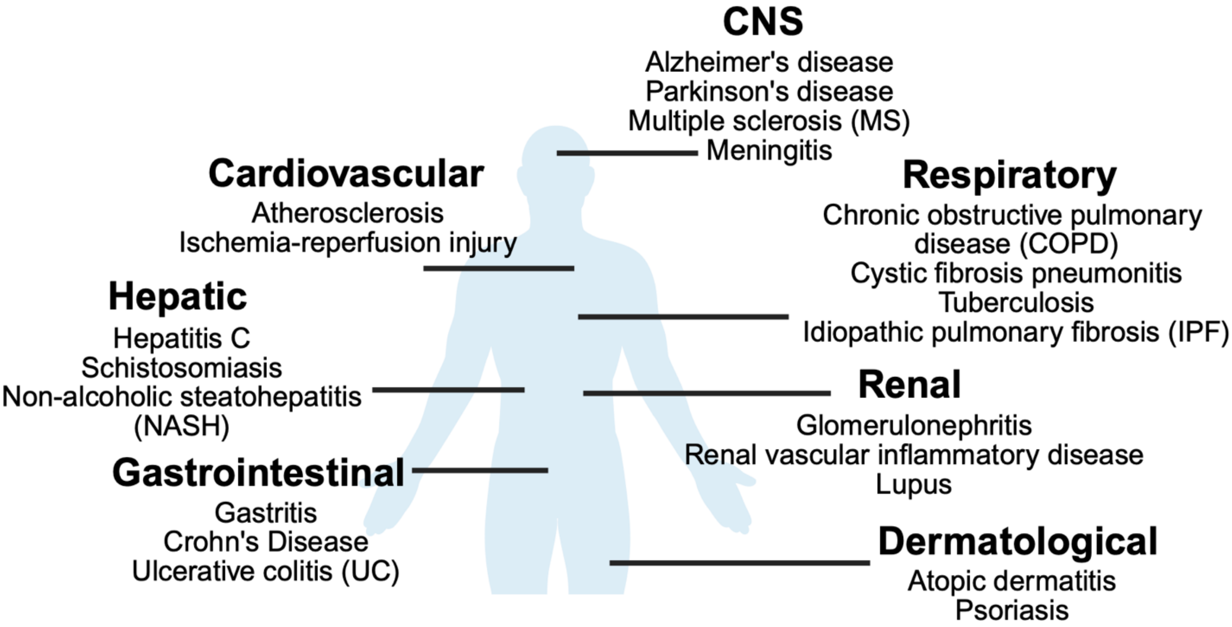

Figure 1.2. Examples of inflammatory diseases in relation to affected organs [31] [1] ***(created using BioRender)***

The triggers of chronic inflammation are complex with diverse contributors, but can broadly be categorised as sterile or non-sterile [2]. Non-sterile triggers involve prolonged exposure to pathogens which are not eliminated. For example, *H. pylori* infection can evade immune clearance and cause persistent gastric inflammation, associated with peptic ulcers and gastric carcinoma [32]. Chronic viral infections such as Hepatitis C result in hepatic inflammation, contributing to fibrosis and carcinoma development [33]. These infections drive inflammation through PAMP recognition, whereas sterile triggers are non-pathogenic and primarily involve DAMPs. Various lifestyle risk factors are associated with low-grade systemic chronic inflammation (SCI). Obesity results from the expansion of adipose tissue which can induce hypoxia cell damage and promote M1 macrophage signalling [34]. Physical inactivity and diets rich in ultra-processed foods (UPF) contribute to obesity, associated with elevated systemic IL-6 levels [35] [36]. Collectively, these factors promote inflammation and are strongly linked with the increased risk of developing cardiovascular disease, diabetes and cancer. Emerging evidence also implicates sustained neuroinflammation with depression and anxiety [37]. Furthermore, exposure to toxins and pollutants, which may be unavoidable, contributes to chronic inflammatory diseases. Cigarette smoke contains thousands of toxic compounds which are absorbed by lung epithelial cells and induce oxidative stress and elevate systemic IL-6 levels, contributing to SCI and drive carcinogenesis [38] [39].

Existing treatments are predominantly focused on symptom control and reducing disease progression, rather than addressing the underlying cause. Conventional approaches include non-steroidal anti-inflammatory drugs (NSAIDs) and corticosteroids, with therapies such as monoclonal antibodies (mAbs) providing a more targeted approach [40] [41]. For example, anti-TNFα mAbs specifically inhibit the pro-inflammatory cytokine TNF-α, with Golimumab an example approved for Rheumatoid arthritis [42]. mAbs have demonstrated clinical efficacy in autoimmune inflammatory diseases and in infectious disease such as COVID-19, but discontinued treatment can result in disease relapse. They are also limited by high manufacturing costs and are associated with adverse hypersensitivity reactions. Such risks include immunogenicity, where anti-drug antibodies reduce therapeutic efficacy or trigger hypersensitivity reactions [43] [44] [45]. Furthermore, while NSAIDs and corticosteroids can provide effective short-term symptom relief, they are limited by significant side effects. NSAIDs are associated with gastrointestinal bleeding, peptic ulcers and nephrotoxicity [46], while prolonged corticosteroid treatment can result in numerous systemic toxicities [47]. These limitations highlight the need for novel therapeutic strategies that not only alleviate symptoms but also target the underlying drivers of inflammation.

1.1.3 Crosstalk with Oxidative Stress

Oxidative stress arises when the production of reactive species exceeds the capacity of the body's antioxidant defence, disrupting redox signalling and cellular function. Reactive oxygen species (ROS) are common classes of reactive species, which also include reactive nitrogen species (RNS) (**Table 1.1**) [48].

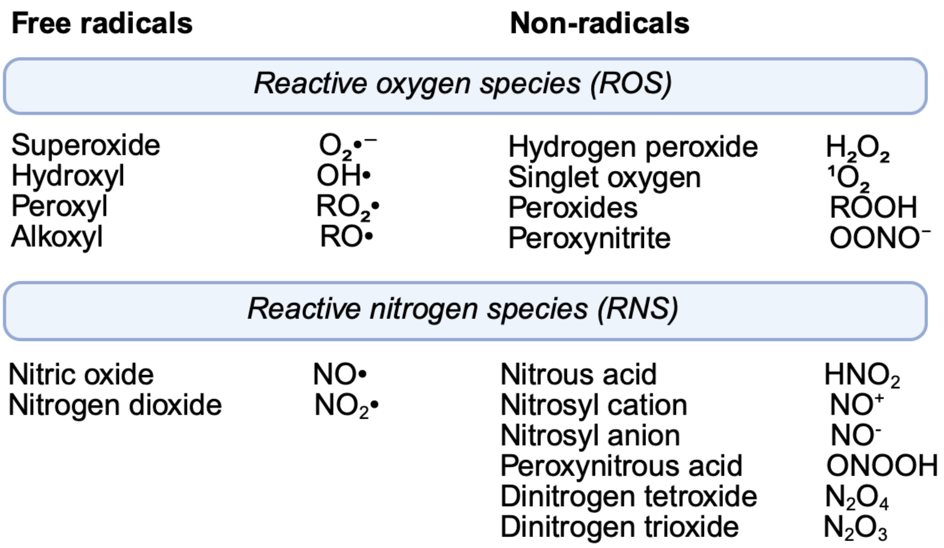

Free radicals		Non-radicals	
Reactive oxygen species (ROS)			
Superoxide	$O_2{\bullet}^-$	Hydrogen peroxide	H_2O_2
Hydroxyl	$OH\bullet$	Singlet oxygen	$^1O_2$
Peroxyl	$RO_2\bullet$	Peroxides	ROOH
Alkoxyl	$RO\bullet$	Peroxynitrite	$OONO^-$
Reactive nitrogen species (RNS)			
Nitric oxide	$NO\bullet$	Nitrous acid	HNO_2
Nitrogen dioxide	$NO_2\bullet$	Nitrosyl cation	NO^+
		Nitrosyl anion	NO^-
		Peroxynitrous acid	ONOOH
		Dinitrogen tetroxide	N_2O_4
		Dinitrogen trioxide	N_2O_3

Table 1.1. Classification of common ROS and RNS reactive species [49] (created using BioRender).

These oxygen-containing molecules function as oxidising agents due to their electron configuration, with free radicals particularly reactive due to their unpaired valence electrons. ROS are endogenously produced, primarily in the mitochondria, as by-products of normal cellular metabolism and are vital for physiological signalling pathways. During inflammation, phagocytic immune cells such as macrophages, neutrophils and dendritic cells generate ROS within the intracellular phagosome to destroy the inciting target. However, ROS can escape extracellularly and readily react with cellular proteins, lipids and DNA, resulting in protein oxidation, lipid peroxidation and DNA modifications. This sustained damage to healthy tissue can contribute to disease [49] [48].

To prevent oxidative stress, ROS are neutralised by both enzymatic and non-enzymatic antioxidant responses. Non-enzymatic antioxidants often function as radical scavengers or electron doners which directly neutralise ROS. The most physiologically abundant is glutathione (GSH), with bilirubin, vitamin C and vitamin E also major contributors [50] [49]. In contrast, the enzymatic antioxidant response, primarily regulated by the transcription factor nuclear factor erythroid-2 related factor 2 (NRF2), converts ROS into less harmful products [49]. Antioxidant enzymes, such as superoxide dismutase (SOD) and catalase, play a central role in detoxifying ROS. SOD catalyses the dismutation of superoxide radicals ($O_2{\bullet}^-$) into hydrogen peroxide (H_2O_2) and oxygen (O_2). Catalase subsequently decomposes H_2O_2 into water and oxygen [49] [51]. Xenobiotic metabolism is closely linked to the antioxidant response, consisting of Phase I (oxidation/reduction), Phase II (conjugation) and Phase III (transport and elimination) enzymes. Phase II enzymes particularly promote antioxidant activity, such as NAD(P)H:quinone oxidoreductase 1 (NQO1), heme-oxygenase-1 (HO-1) and glutathione S-transferase (GST) [49]. Expression of these genes collectively reduce oxidative stress and restore homeostasis.

Inflammation and oxidative stress are tightly interconnected, where each amplifies the other (**Figure 1.3**). Excessive ROS generation inflicts cellular damage through oxidative stress, releasing DAMPs which drives pro-inflammatory signalling. In turn, chronic inflammation drives further ROS production, through phagocytic activity, perpetuating oxidative stress and sustaining the cycle.

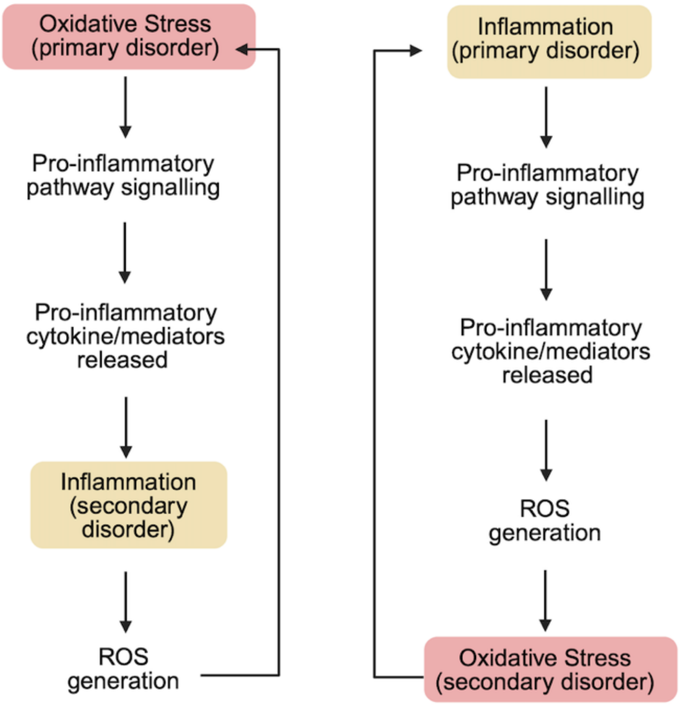

Figure 1.3. Schematic of the interconnected relationship between inflammation and oxidative stress (created using BioRender).

As discussed previously, DAMP and PAMP signalling by PRRs in neutrophils, dendritic cells and monocytes activates the NF-κB pathway. The IKK complex phosphorylates IκBα (NF-κB repressor), which marks it for degradation. This allows NF-κB to translocate to the nucleus to induce pro-inflammatory cytokine, cell adhesion molecules and NADPH oxidase (NOX) enzyme genes, amongst others [8]. NOX enzymes catalyse superoxide generation which drives ROS production and oxidative stress [49]. In a mouse model of neuroinflammation, NOX2 upregulation directly increased ROS levels, contributing to cell damage and increased IL-1β levels [52] [53]. Similarly, in a mouse model of glaucoma, NOX2-catalysed ROS generation was also found in activated glial cells with elevated IL-1β, TNF-α and IL-6 [54]. NOX-catalysed ROS can also activate the NOD-like receptor protein 3 (NLRP3) inflammasome, which is a PRR involved in pro-inflammatory signalling, which has been shown *in vitro* and *in vivo* [55] [53] [56]. Pro-inflammatory cytokines can also promote ROS generation by activating NOX enzymes, forming a cycle of inflammation and oxidative stress [48]. In cardiovascular disease, TNFα promotes NOX-dependent ROS production in human vascular smooth muscle cells [57], while in endothelial cells IL-6 was found to have the same effect [58]. Interestingly, NOX activity may also contribute to age-related systemic chronic inflammation (SCI) before it potentially becomes pathological. For example, in humans, NOX2 expression is elevated in healthy older aged brain tissue, which also correlates with increased lipid peroxidation and IL-1β, compared to younger aged brain tissue [53]. This suggests chronic inflammation can progress quietly without showing symptoms and is a prerequisite for neuroinflammatory diseases.

1.2 The KEAP1/NRF2/ARE Pathway

1.2.1 The NRF2 Antioxidant and Anti-inflammatory Response

Nuclear factor erythroid 2-related factor 2 (NRF2), encoded by the *NFE2L2* gene, is a transcription factor central to cellular defence. The isolation of NRF2 over 30 years ago, combined with the generation of NRF2 knockout (KO) mice, led to investigation into downstream target genes [59] [60]. Since then, NRF2 has been found to regulate hundreds of antioxidant response element (ARE) genes, particularly those involved in redox homeostasis and xenobiotic detoxification, gaining recognition as a 'master regulator' of the antioxidant response[61] [62]. These genes contain an electrophile response element (EpRE) within the promotor region, which consists of the core sequence (5'-TGA-NNNN-GC-3'). This core is flanked by other gene-specific nucleotides essential for transcriptional activity [63]. NRF2 regulates a range of Phase II detoxification enzymes and antioxidant proteins and enzymes which have been identified through chromatin immunoprecipitation (ChIP) and reported *in vitro* and/or *in vivo* [61] (**Table 1.2**).

Phase II detoxification enzymes			Antioxidant proteins and enzymes				
NQO1	UTGs	GSTs	ROS scavenging enzymes	GSH synthesis & recycling	Heme and iron metabolism	NADPH generation	Thioredoxin system
	UGT1A6 UGT2B5 UGT1A1	GSTA1 GSTA2 GSTA3 GSTA4 GSTM1 GSTM2 GSTM3 GSTM4 GSTP1 GSTP2 MGST1 MGST3	CAT SOD1, SOD2 GPX1, GPX2, GPX3, GPX4	GCLC GCLM GSR SLC7A11	HMOX1 FTH1 FTL BLVRB	G6PD PGD ME1 TALDO1 TKT GBE1	TXNRD1 TXN SRXN1 PRDX1 PRDX6

Table 1.2 Examples of NRF2 regulated ARE genes [61] (created using BioRender).

NQO1 was the first phase II detoxification enzyme found to be transcriptionally regulated by NRF2 [64]. It catalyses the two-electron reduction of electrophilic quinones to hydroquinone, preventing redox cycling and reducing oxidative stress and inflammation [65] [66]. Heme-oxygenase-1 (HO-1) is another canonical NRF2-regulated gene [67]. HO-1 catalyses the degradation of pro-inflammatory heme into anti-inflammatory carbon monoxide (CO) and biliverdin (which is rapidly converted into the antioxidant bilirubin) [68]. Other examples of NRF2-regulated genes (see **Table 1.2**) include catalase (CAT), superoxide dismutases (SODs) and glutathione peroxidases (GPXs), which are the enzymatic first line of defence against ROS, sequentially converting them into oxygen and water [69]. NRF2 regulates antioxidant genes directly, but also indirectly regulates inflammation. HO-1-derived metabolites including biliverdin and CO inhibit IKKβ activity, thereby preventing NF-κB-dependent pro-inflammatory gene expression. HO-1 and thioredoxin (TXN) are found to inhibit the expression of pro-inflammatory cytokines, through reduced NLRP3 signalling *in vivo* [70] [71]. Also, in monocyte/bone marrow derived macrophages, NRF2 is found to upregulate anti-inflammatory TNF α-induced protein 3 (A20) which suppresses activation of NF-κB [72]. A20 expression is also induced downstream of NRF2 activation, which contributed to reduced neuroinflammation in a mouse model [73].

1.2.2 NRF2 in Disease Pathology

Although NRF2 knock out (KO) mice develop normally and remain fertile under normal conditions, they exhibit increased susceptibility and more severe pathology in models of kidney [74] [75], cardiovascular [76], metabolic [77] and liver [78] diseases compared with WT mice. Conversely, Keap1 knock-down (KD) murine disease models are found to improve disease pathology through NRF2 activation [79] [80], highlighting the relevance of NRF2 in disease and the protective role of the NRF2/ARE pathway.

In Alzheimer's disease (AD), NRF2 is sequestered in the cytoplasm of neurones and reduces NQO1 expression which contributes to disease pathology [81] [82]. Numerous NRF2 KO studies with AD mouse models found loss of NRF2 function to correlate with elevated amyloid-β deposition, tau phosphorylation, cognitive deficits and elevated pro-inflammatory cytokines; all of which are hallmarks of disease [83] [84] [85]. Activation of NRF2 in AD human astrocytes attenuated amyloid-β pathology and a Phase II clinical trial improved cognitive outcomes in patients treated with Benfotiamine, a synthetic vitamin B1 derivative reported to activate the NRF2/ARE pathway [86] [87]. Beyond Alzheimer's, NRF2 activation has demonstrated protective roles in various disease models *in vivo* (**Table 1.3**). For example, in mouse models of diabetic nephropathy where NQO1 is downregulated, NQO1 induction resulted in reduced inflammation and fibrosis [88]. Likewise, NQO1 overexpression, alongside Keap1 degradation, was found to be protective against obesity mouse models with a high-fat diet. The mice displayed improved insulin sensitivity and glucose homeostasis [89]. Low HO-1 expression is also implicated in various diseases; for example, suppression in mice post intracerebral haemorrhage increased neuronal injury and M1 macrophage polarisation [90], while HO-1 KO exacerbates plaque formation in an atherosclerosis mouse model [91]. In humans, a polymorphism in the HO-1 promotor consisting of ≥32 tandem repeats on both alleles is associated with reduced HO-1 transcription, accelerated atherosclerosis progression and increased cardiovascular disease risk [92]. Conversely, NRF2/HO-1 activation is found to improve hallmarks of disease in atherosclerosis [93], liver disease [94], inflammatory bowel disease [95] and other age-related inflammatory diseases [96]. Interestingly, HO-1 KO liver injury mice models are found to display M1 macrophage polarisation, increased immune cell infiltration, and enhanced hepatocyte injury [97]. In a murine model of cholestatic liver injury (CLI) , NRF2/HO-1 activation exacerbated disease through upregulation of bilirubin which was hepatoxic, with NRF2 KO attenuating pathology [98].

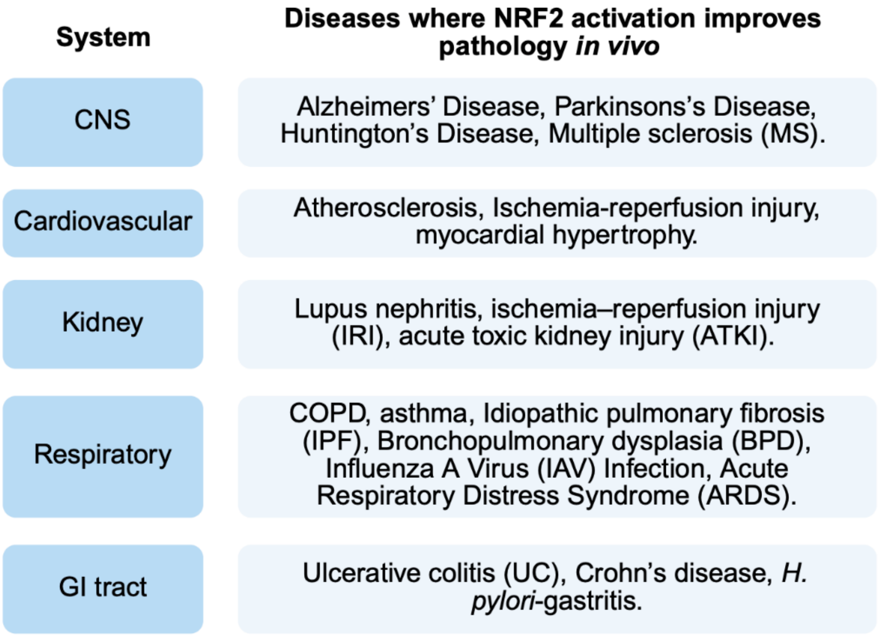

System	**Diseases where NRF2 activation improves pathology *in vivo***
CNS	Alzheimers' Disease, Parkinsons's Disease, Huntington's Disease, Multiple sclerosis (MS).
Cardiovascular	Atherosclerosis, Ischemia-reperfusion injury, myocardial hypertrophy.
Kidney	Lupus nephritis, ischemia–reperfusion injury (IRI), acute toxic kidney injury (ATKI).
Respiratory	COPD, asthma, Idiopathic pulmonary fibrosis (IPF), Bronchopulmonary dysplasia (BPD), Influenza A Virus (IAV) Infection, Acute Respiratory Distress Syndrome (ARDS).
GI tract	Ulcerative colitis (UC), Crohn's disease, *H. pylori*-gastritis.

Table 1.3. Examples of diseases where NRF2 activation is beneficial, involving the CNS [99], CVS [100], Kidney [101], respiratory system [102] and GI tract [103] [104].

The effects of NRF2 activation in cancer is complex and has been extensively reviewed elsewhere [105] [106]. While NRF2 exerts protective effects in healthy tissue by preventing carcinogenesis, its sustained activation in established tumours can promote tumour growth and metastasis, further demonstrating NRF2 activation is selectively beneficial depending on disease pathology.

1.2.3 NRF2 Structure and Domains

The Cap 'n' Collar basic leucine zipper (CNC-bZIP) family includes four closely related mammalian transcription factors: NF-E2 (*NFE2*), NRF1 (*NFE2L1*), NRF2 (*NFE2L2*) and NRF3 (*NFE2L3*). Among these, NRF1, NRF2 and NRF3 regulate gene expression through binding with small Maf proteins (sMaf) as heterodimers to the ARE enhancer regions in target genes [107]. NRF2 comprises seven distinct NRF2-ECH homology (Neh) domains, Neh1 to Neh7 (**Figure 1.4**). These domains mediate transcriptional activity and protein interactions, which supports NRF2-regulated ARE gene expression [108]. While domain structure is highly conserved, domains Neh1, Neh2 and Neh7 contain structurally flexible elements which allow selective binding with diverse targets [109].

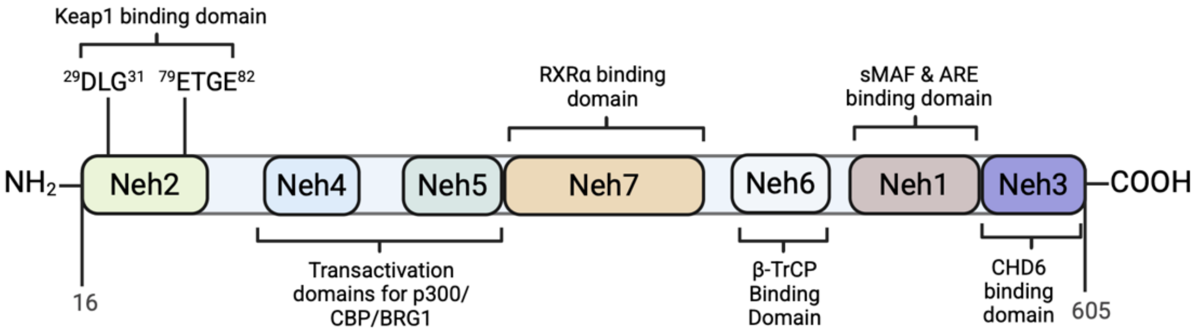

Figure 1.4. The domain structure of NRF2 with primary functions [110] [108] (created using BioRender).

The Neh1 domain contains the CNC region, which includes the bZIP motif. The leucine zipper mediates heterodimerisation with sMaf proteins, while the basic region allows the heterodimer to bind to AREs on target genes (**Figure 1.4**) [108]. The N-terminal Neh2 domain functions as a redox-sensitive degron which binds KEAP1 under basal conditions. This occurs through two regions, the high affinity 'ETGE' and low affinity 'DLG' motifs [111] [112]. The C-terminal Neh3 domain is essential for transcriptional activator binding, as Neh3 mutation abolished transcriptional activity [113]. It also contains an amino acid motif 'VFLVPK' which is highly conserved within the CNC family [113]. Phosphorylation of a residue in this region (Y567) reduced sMaf binding, suggesting it may stabilise the Neh1 domain or serve as a regulatory site [114]. Similarly, the Neh4 and Neh5 domains are required for transcriptional activity, binding transcriptional coactivators including CBP (CREB binding protein) and p300. Both domains are reported to synergistically bind CBP and p300, which is vital for NRF2 transcriptional activity [115] [116] [117]. Neh5 contains a CBP binding motif conserved across CNC family proteins, whereas Neh4 contains a motif found also in other transcription factors [116]. Both domains also interact with BRG1, a chromatin remodelling protein, to promote NRF2 transcription [118]. The Neh6 domain contains a KEAP1-independent degron which regulates NRF2 stability under basal and oxidative stress conditions. Neh6 contains two motifs which bind β-transducin repeat-containing protein (βTrCP), which mediates Keap1-independent degradation of NRF2 [119] [120]. The Neh7 domain interacts with retinoid X receptor alpha (RXRα) which inhibits NRF2 transcriptional activity through the disruption of transcriptional coactivator recruitment [121].

1.2.4 Keap1 Regulation of the NRF2/ARE pathway

Under basal conditions, NRF2 is constitutively expressed but remains transcriptionally inactive due to its rapid turnover, with a half-life of approximately 20 min [122] [123]. This strict regulation is mediated by its negative regulator, Kelch-like ECH-associated protein 1 (KEAP1), which acts as a substrate adaptor for the CUL3/RBX1 E3 ubiquitin ligase complex. KEAP1 homodimers bind NRF2 and facilitate its polyubiquitination, targeting it for degradation by the 26S proteasome (**Figure 1.5**) [124] [125].

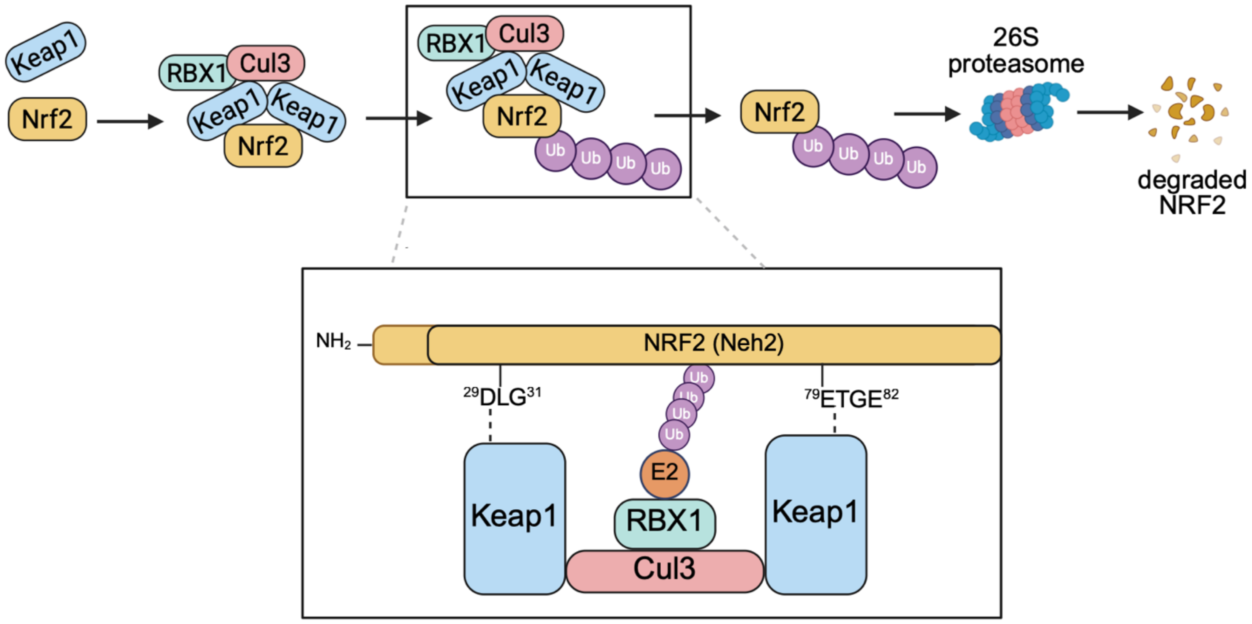

Figure 1.5. The pathway of Keap1-mediated NRF2 degradation (created using BioRender).

Keap1 (encoded by the *KEAP1* gene) is a member of the Broad complex-Tramtrack-Bric-a-brac (BTB) Kelch protein family, classified within the Kelch-like gene family members (KLHL) as KLHL19 [126] [127]. Similarly to other KLHL family proteins, the BTB, IVR and Kelch domain are critical for NRF2 regulation. Although no full Keap1 crystal structure exists to date, a 24-

Å reconstruction of mouse Keap1 homodimers using electron microscopy revealed a 'cherry bob' shape. The IVR is wrapped around the central core of the two large globular Kelch spheres, with the BTB homodimer forming the connecting stalk [128]. The BTB domain is essential for Keap1 homodimer formation and CUL3 binding, vital processes for NRF2 binding and assembly of the Keap1/CUL3/RBX1 E3 ligase complex (**Figure 1.5**). The domain contains a conserved residue Ser104 which was found to be critical for dimer formation, as a point mutation (S104A) prevented Keap1 dimerisation and NRF2 binding [129].

The first crystal structure of the human Keap1 BTB domain (PDB:4CXI) was resolved by Cleasby *et al.* in 2014 [130]. Each Keap1 monomer adopts a fold consisting of a three-stranded β-sheet, flanked by six α-helices (α1 to α5). Dimerisation occurs through the α1 helices of each monomer (**Figure 1.6**). More recently, Adamson *et al.* (2023) resolved the crystal structure of the BTB domain in complex with the '3-box' motif (PDB:5NLB) [131]. This motif consists of Leu115, Arg116, Glu117 which is found between the BTB and IVR domains. Each Keap1 dimer was found to bind one CUL3 to form a heterotetramer (2:2), with Leu115 inserting into a deep pocket of CUL3 to anchor the complex. The BTB α5 helix forms hydrogen bonds with CUL3 tyrosine residues, while BTB Arg116 and Glu117 stabilised the complex.

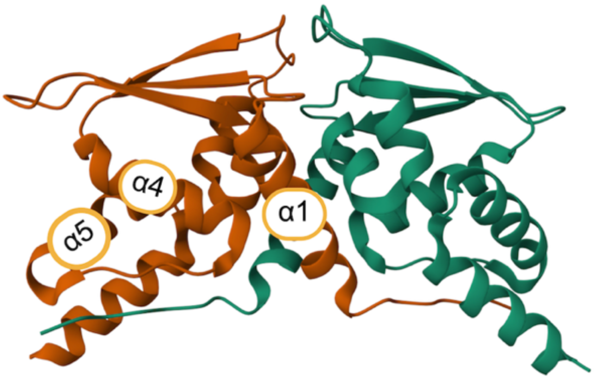

***Figure 1.6. The crystal structure of the BTB domain homodimer (PDB:4CXI)* [130].**

The Kelch domain is the site where Keap1 binds to the 'ETGE' and 'DLG' Neh2 motifs of NRF2. The first crystal structure of the human Keap1 Kelch domain was resolved by Li *et al.* (2004) (PDB:1U6D), revealing a six-bladed β-propeller fold, where each blade consists of four anti-parallel β-strands arranged around a central solvent accessible centre (**Figure 1.7**) [132]. The fifth blade extends back to the first, forming a continuous propeller structure. Although the full-length crystal structure of NRF2 bound to Keap1 has yet to be resolved, NRF2 derived peptides provide evidence of binding. In 2006, Lo *et al*. resolved the same Kelch domain crystal structure but in complex with a 16-mer NRF2 derived peptide containing the sequence

‘^{69}AFFAQLQLDEETGEFL^{84}’ (PDB:2FLU) [133]. The peptide adopted a β-hairpin fold, with two short antiparallel β-strands linked by a tight turn in the ‘ETGE’ region, which arranged in a shallow pocket. The peptide primarily interacted through F83 to E79 peptide residues, forming interactions with ten Kelch domain residues. The peptide also bound with high affinity (K_d of 20 nM) through isothermal titration calorimetry, collectively supporting the high affinity binding of the ‘ETGE’ motif of NRF2 with Keap1. Also in 2006, Padmanabhan *et al.* resolved the mouse Kelch domain bound to an ‘^{79}ETGE^{82}’ containing peptide [134]. Similarly, the peptide adopted a β-hairpin fold and bound in the same pocket. This pocket is on the bottom side of the β-propeller in an electropositive region with the rim formed by Arg380, Arg415, Arg483, and His436 residues. The cavity also contains basic residues, proving a favourable binding site for the acidic ‘ETGE’ motif of NRF2. Point mutations in the Kelch domain (G364C and G430C) were found to sterically hinder Ser363-E82 and Ser431-E79 interactions respectively, disturbing the interface for NRF2 binding [134]. This highlights the essential role of the Kelch domain for NRF2 binding, where minor mutations can impair activity.

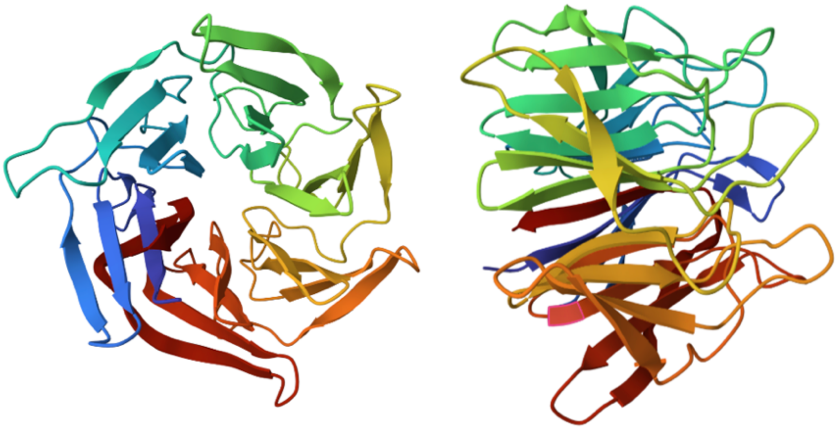

Figure 1.7. The crystal structure of the Kelch domain (PDB:1U6D) [132].

While NRF2 ‘ETGE’ binding provides high affinity binding functioning as a ‘hinge’, the ‘DLG’ motif functions as a ‘latch’ to stabilise the NRF2/Keap1 complex. Comparison of the co-crystal structures of ‘ETGE’ (PDB:2FLU)[132] and ‘DLG’ (PDB:2DYH)[135] peptides bound to the Kelch domain reveals they both adopt a similar β-hairpin conformation. However, the ‘DLG’ peptide was found to bind on the surface with 8 electrostatic interactions, whereas the ‘ETGE’ peptide extended into the binding pocket with 13 interactions. ITC measurements showed that the ‘ETGE’ peptide had ~200-fold higher affinity compared to the ‘DLG’ peptide. The ‘DLG’ motif only has one acidic residue which forms the latch, in contrast to the multiple acidic residues in ‘ETGE’ which account for the difference in binding affinity[135]. The crystal structure of a ‘DLG’ peptide with extended residues (PDB:3WN7) shows these surrounding residues provide vital stabilising interactions, which was confirmed through differential scanning fluorimetry (DSF).

Mutations of these surrounding residues can selectively abolish binding with Keap1, through a GST pulldown assay [136].

1.2.5 Keap1- independent Regulation of NRF2

While Keap1 is the primary negative regulator of NRF2, β-transducin repeat-containing protein (βTrCP) represents a major secondary pathway. The Neh6 domain of human NRF2 contains two motifs ‘^{382}DSAPGS^{387}’ and ‘^{343}DSGIS^{347}’ which are recognised by β-TrCP, the F-box/WD40 substrate receptor of the β-TrCP/CUL1 E3 ligase complex which ubiquitinates and degrades NRF2[137]. Deletion of either motif reduced β-TrCP binding to NRF2 in co-immunoprecipitation assays[138]. Glycogen synthase kinase-3β (GSK-3β) phosphorylates the serines within the ‘^{343}DSGIS^{347}’ motif which provides a higher affinity binding site for βTrCP. Peptide affinity pull-down assays found βTrCP to bind ‘^{343}DSGIS^{347}’ with higher affinity when its phosphorylated, with no similar effect on ‘^{382}DSAPGS^{3387}’ [138]. GSK3β can be inactivated by the Phosphatidylinositol 3-kinase (PI3K)/Akt pathway, allowing NRF2 to escape degradation [139]. Inhibition of GSK-3 in Keap1 deficient mouse embryo fibroblasts (MEFs) increased NRF2 levels [120], whereas GSK-3β activation in Keap1 deficient (MEFs) and human lung A549 cells significantly reduced NRF2 levels and ARE expression [138] [139].

Other NRF2 degradation pathways have also been reported. X-box binding protein 1 (XBP1) is a transcriptional regulator of the endoplasmic reticulum (ER) stress response. One of its downstream targets, HRD1, is an E3 ubiquitin ligase which binds to NRF2 through the ‘^{125}QSLVPDI^{131}’ motif in the Neh4 domain, which mediates its degradation. In human cirrhotic liver cells, ER stress drives XBP1/HDR1 signalling that suppresses NRF2 [140] [141]. In mouse models with induced liver cirrhosis, deletion of the HDR1 gene prevented NRF2 degradation and promoted ARE-mediated gene expression [141]. Another pathway involves WDR23, which is a WD40-repeat substrate receptor for the WDR3-CUL4-DDB1 E3 ligase complex. It was found to bind to the ‘^{16}DIDLID^{21}’ motif in the Neh2 domain of NRF2 and mediate degradation independent of Keap1 *in vitro* [142].

1.2.6 NRF2 Activation by Keap1 Sensor Cysteines

NRF2 can be activated by multiple stressors, including pro-inflammatory stimuli such as lipopolysaccharide (LPS) and pro-inflammatory mediators, alongside oxidative stress from ROS accumulation and electrophilic compounds [143] . According to the “hinge and latch” model, Keap1 cysteine modifications weaken the interaction between Keap1 and the low-affinity DLG ‘latch’ motif of NRF2, while binding to the high affinity ETGE ‘hinge’ motif remains, which prevents NRF2 ubiquitination and degradation [144]. Whereas, the Keap1-CUL3 dissociation model proposes that cysteine modifications disrupts the interaction between Keap1 and CUL3, allowing NRF2 to escape degradation (**Figure 1.8**) [145]. NRF2 activation by p52 (NF-κB subunit) and Keap1-NRF2 PPI inhibitors have been found to involve the "hinge and latch" model, but not by electrophilic inducers, as found through NMR spectroscopy titration experiments [146]. This suggests the mechanism of activation depends on the inducer. In both models NRF2 predominantly remains bound and transcriptionally inactive, but newly synthesised NRF2 can accumulate, translocate into the nucleus, bind ARE genes as heterodimers with sMaf proteins and activate ARE gene expression [147] [64]. These cysteine residues on Keap1 function as sensors of oxidative stress, which are also targets for NRF2 electrophilic inducers. Human Keap1 comprises 27 cysteine residues, of which a subset have been identified to function as sensors, each with distinct localisation and reactivity. Early mass spectrometry and cysteine point mutation studies identified reactive residues Cys151, Cys273, Cys288 and Cys613 which contribute to oxidative/electrophilic stress sensing [148] [149] [150]. Subsequently, Cys151, Cys226 and Cys273, Cys288 were found to be susceptible to covalent modifications by NRF2 activating electrophilic compounds [151] [151] [152].

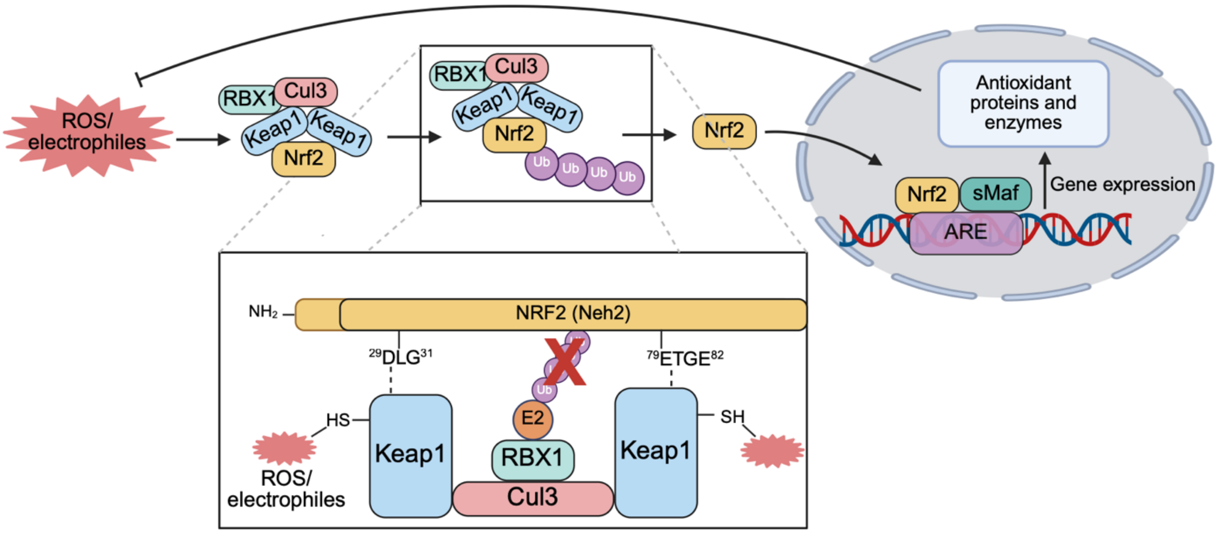

Figure 1.8. Activation of the Keap1/NRF2/ARE pathway and its regulation by ROS/electrophiles (created using BioRender).

The Cys151 residue is found in the BTB domain of Keap1 (**Figure 1.9**). The co-crystal structure of this domain with an electrophilic NRF2 activator (CDDO) (PDB:4CXT [130]) shows Cys-151 was covalently modified. Cys151 is located at a solvent exposed region, surrounded by basic residues (His129, Lys131, Arg135, Lys150, His154). This could reduce the pKa of Cys151, making the thiol more susceptible to Michael addition reactions with electrophiles [130]

[153]. Overlaying the crystal structure with KLHL11 (a homologous KLHL protein) in complex with CUL3 (PDB:4APF[154]) positioned Cys151 adjacent to a hydrophobic groove in the 3-box motif of KLHL11, which is vital for CUL3 binding. A more recent study found CDDO functioned as a partial antagonist which reduced the binding affinity of CUL3 to human Keap1, by a TR-FRET assay [131]. This suggests modifications to the Cys151 could result in a conformational change which disrupts Keap1/CUL3 binding, allowing NRF2 to escape degradation. The role of Cys151 has also been investigated with Keap1 C151S mice, which found that Cys151 is not involved in basal NRF2 degradation but is required to sense electrophilic stress[155].

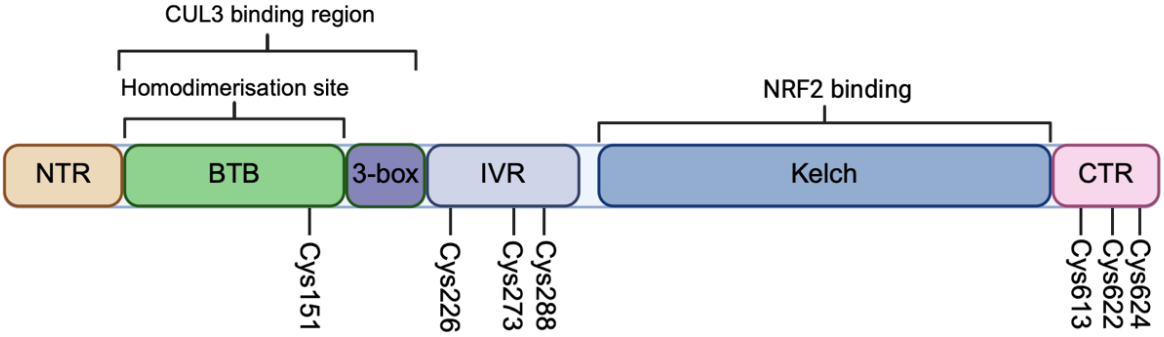

Figure 1.9. The Keap1 domain structure with sensor cystine location* [156] *(created using BioRender).

Other sensor cysteines are found in the IVR (Cys226, Cys273, Cys288) and C-terminal CTR domain (Cys613, Cys622 and Cys624) (**Figure 1.9**). Using Keap1 point mutation knock-in mice, the residues Cys151, Cys273 and Cys288 were found sense stress individually or cooperatively depending on the stressor [156]. Also, through a mouse model of physiological oxidative stress (selenocysteine tRNA KO), Cys226 and Cys613 were essential to detect oxidative stress. Treatment of an NRF2 activator (CDDO-Im) was only responsive to Cys151 and not Cys226 and Cys613, demonstrating selectivity [157]. Also, mice expressing both WT Keap1 and Cys226/Cys613 mutants (producing heterozygous Keap1 dimers), still responded to oxidative stress. This suggests cysteine modifications within a single subunit of the Keap1 homodimer is sufficient to sense oxidative stress, highlighting sensor sensitivity. Furthermore, through whole-genome sequencing (WGS), seven gene variants were found to potentially affect Cys226, Cys613, Cys622 and Cys624, with no variants for Cys151, Cys273, Cys288. This suggests evolutionary pressure has allowed for oxidative stress sensors to tolerate variation and form a fail-safe system which allows redundancy, whereas electrophilic sensors are strictly conserved due to their non-redundancy function [157].

NRF2 activation can also occur independently to Keap1 cysteine modifications. For example, increased levels of p62 (SQSTM1), an autophagy adaptor protein, has been found to bind

Keap1 and promote its autophagy, allowing NRF2 to escape Keap1-mediated degradation [158]. Proteasomal inhibitors, such as MG132, prevent ubiquitinated NRF2 from being degraded by the 26S proteasome [159]. The electrophilic activator DMF is also found to exert NRF2 activation independent to Keap1 by inactivating GSK-3β, through PI3K/AKT signalling, which allows NRF2 to escape degradation [160].

1.2.7 NRF2 Activators/Keap1 Inhibitors

Pharmacological activation of NRF2 provides a promising therapeutic strategy to reduce inflammation and oxidative stress implicated in disease pathology. Most NRF2 activators, also termed inducers, function by inhibiting Keap1-mediated degradation, effectively acting as Keap1 inhibitors. These activators can be broadly classified into two categories: electrophilic activators (synthetic and select natural products) and protein-protein interaction (PPI) inhibitors [161] [162].

1.2.7.1 Electrophilic Activators

Electrophilic activators are the oldest class of NRF2 inducers that covalently modify Keap1 cystine residues which prevent NRF2 ubiquitination and degradation. They are typically Keap1 Cys151 selective, but are also found to modify Cys273 and Cys288 [163]. The NRF2 activator CXA-10 (10-NO_2-OA), a nitrated fatty acid, targets Cys273 and Cys288 [164]. Numerous mouse models of disease have found CXA-10 to promote anti-inflammatory mediators and decrease NF-κB expression [165] [166]. A completed Phase I clinical trial was well tolerated, with an ongoing Phase II trial investigating efficacy in pulmonary arterial hypertension (NCT04125745) [167]. Cys151-selective NRF2 activators include bardoxolone-methyl (CDDO-Me), omaveloxolone (RTA-408), dimethyl fumarate (DMF), oltipraz and sulforaphane as classic examples [161] [163]. To date, four NRF2 activators have received FDA approval, all of which are small molecules which contain an electrophilic Michael acceptor (**Figure 1.10**). Dimethyl fumarate (DMF) (Tecfidera) was approved in 2013 for relapsing-remitting multiple sclerosis (RRMS) [168].

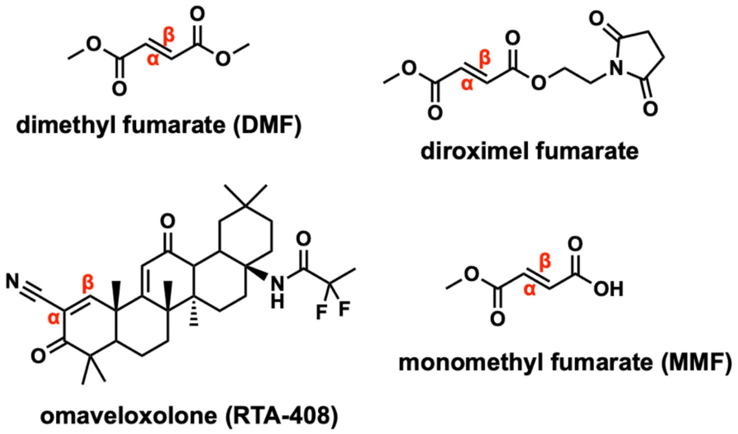

Figure 1.10. Examples of NRF2 electrophilic activators, with the α,β-unsaturated carbons in red.

Its active metabolite, monomethyl fumarate (MMF) (Bafiertam) followed in 2020, which was preceded by its pro-drug, diroximel fumarate (Vumerity) having gained approval in 2019 [169] [170]. Both were approved for Relapse-Remitting Multiple Sclerosis (RRMS). Most recently, omaveloxolone (Skyclarys), was approved in 2023 as the first available treatment for Friedreich's ataxia, a rare neuromuscular disease. All approved NRF2 activators contain an α,β-unsaturated moiety, which allow for Michael addition with Keap1 cysteines [171]. Dimethyl fumarate (DMF) contains two α,β-unsaturated dicarboxylic ester groups, while its active metabolite monomethyl fumarate (MMF) retains one ester and one acid. The pro-drug diroximel fumarate likewise contains an α,β-unsaturated moiety but incorporates cleavable linkers for improved gastrointestinal tolerability [172]. Omaveloxolone, a cyanoenone triterpenoid derived from oleanolic acid, contains an α,β-unsaturated ketone conjugated to a nitrile, forming a cyanoenone. The crystal structure of a similar cyanoenone-containing NRF2 activator, bardoxolone, shows the electrophilic β-carbon undergoes Michal addition with Keap1 Cys151[130]. The α,β-unsaturated system makes these compounds strongly electrophilic, especially the cyanoenone group of omaveloxlone, allowing them to readily react with cystines and potentially explains their success in the clinic.

Naturally derived NRF2 activators have attracted increasing attention in recent years, particularly those sourced from the diet. The most well-known example is sulforaphane, an isothiocyanate found in cruciferous vegetables. It can penetrate the blood-brain barrier and is protective in various neuroinflammatory disease animal models [161]. In mouse models of diabetes it upregulated NQO1, GCLC and GCLM expression which reduced ROS-mediated lipid peroxidation [173]. Similar effects were found in ulcerative colitis mice models with reduced ROS levels, NLRP3 activation and IL-1β expression found [174]. A molecular docking study of 332 food-derived electrophilic compounds identified three α,β-unsaturated-containing compounds, 4-hydroxyderricin (4HD), isoliquiritigenin (ISO), and butein, which were found to significantly upregulate NRF2-mediated ARE gene expression, which reduced ROS levels *in vitro*. Covalent docking studies found they formed covalent bonds with Cys151 through their α,β-unsaturated carbonyl groups [175]. Beyond therapeutic intervention, sulforaphane has also shown prophylactic potential against chronic inflammatory diseases. The cytoprotective effects have been extensively demonstrated *in vivo* and *in vitro*, protecting the kidney, liver, brain and heart from exogenous toxins through NRF2/ARE activation [176]. This is supported by a Phase II clinical trial with ex-smokers, finding sulforaphane reduced bronchial epithelial cell proliferation, a marker associated with lung cancer [177].

While electrophilic NRF2 activators have demonstrated clinical success, their use is not without limitations. Electrophilic NRF2 activators lack selectivity for Keap1 cysteine residues and could modify cysteine residues on other proteins. In clinical trials for DMF, gastrointestinal disturbances and flushing were commonly reported, with lymphopenia causing the greatest concern. Consequently, patients prescribed DMF (Tecfidera) are advised to regularly monitor their blood count as a preventative [178]. DMF may contribute to lymphopenia by modifying T cell cysteine residues[179]. Similarly, a post-commercialisation safety study of omaveloxolone reported that 24% of patients experienced side effects, with 9% discontinuing treatment within the first year [180]. The lack of selectivity may contribute to these side effects, which presents a challenge for electrophilic activators as a class. Therefore, a more targeted approach through protein-protein interactions (PPI) may be more suitable.

1.2.7.2 Protein-Protein Interaction (PPI) Inhibitors

In addition to electrophilic activators, NRF2 is also activated through small molecules or peptides that directly disrupt the Keap1-NRF2 protein-protein interaction (PPI). While electrophilic activators covalently modify reactive cysteines, PPI inhibitors typically bind non-covalently with improved selectivity to the Kelch domain of Keap1. A common peptidomimetic strategy involves incorporating the high affinity ‘ETGE’ motif from NRF2 to bind Keap1. Initial work has produced a series of linear ‘ETGE’ containing peptides of various lengths and composition. The smallest reported peptide with measurable Keap1 affinity is a 7mer (DEETGEF), with potency increased by ~7-fold from substituting Glu with Ala (DAETGEF) (**Figure 1.11**)[181]. Peptide sequence elongation does not confer activity, as the 9mer and 8mer peptides displayed comparatively reduced activity [182]. It suggests optimal bindings requires precise residue positioning rather than maximal sequence length.

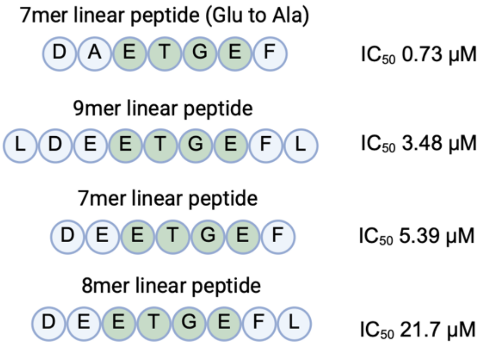

Figure 1.11. Sequence of linear PPI Keap1 inhibitors (made using BioRender).

Peptide cyclisation has been shown to enhance Keap1 binding affinity by pre-organising the backbone into the β-hairpin conformation required for optimal binding. The affinity of a 16mer linear peptide (K_d 23 nM) was improved by introducing a cyclisation between two Cys residues (cyc76-83), which increased affinity by ~2-fold (**Figure 1.12**). A second cyclic analogue incorporated an additional residue to form the cyclisation between Cys and Phe (cyc75-84), with further enhanced affinity by ~4-fold compared to the linear counterpart (**Figure 1.12**) [183].

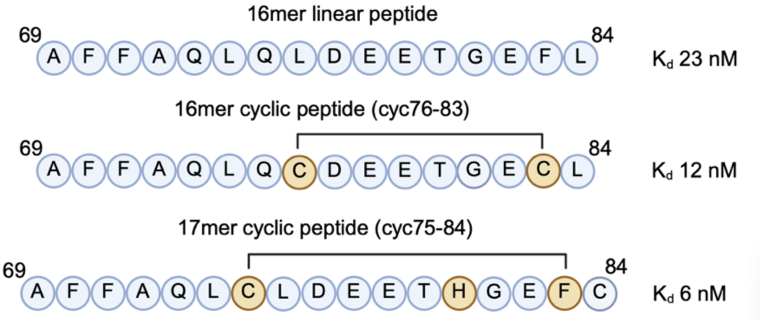

Figure 1.12. Sequence of cyclic PPI Keap1 inhibitors (created using BioRender).

Head-to-tail cyclisation has also been shown to enhance Keap1 binding. Comparison of an 11mer linear peptide with its head-to-tail cyclic analogue found it enhanced activity by ~3.4 fold (**Figure 1.13**). *In vitro*, the cyclic peptide induced greater NRF2/ARE pathway activation than the linear counterpart. In RAW264.7 macrophages, treatment with 1 µM of cyclic peptide moderately elevated HO-1, GCLM and NQO1 protein levels and attenuated LPS-induced inflammation, whereas the linear peptide had no effect [184].

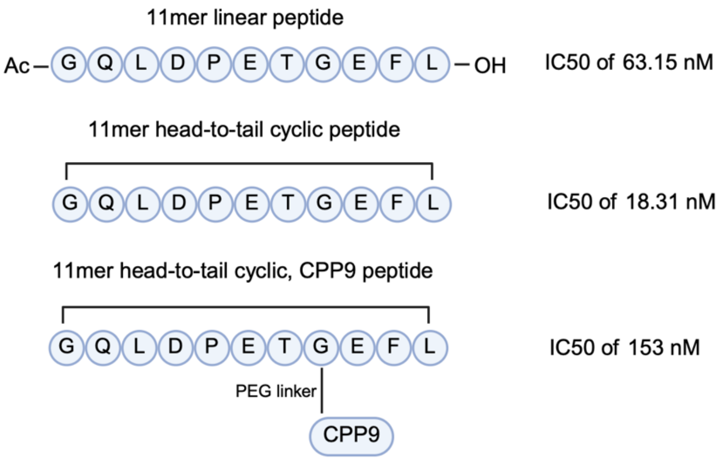

Figure 1.13. Sequence of head-to-tail cyclic Keap1/NRF2 PPI inhibitors (created using BioRender)

Subsequently, the cyclic 11mer was conjugated to a cell-penetrating peptide (CPP9) at a non-essential Gly residue, which increased cell permeability by ~98-fold (**Figure 1.13**). This modification decreased binding affinity by ~8.4-fold but enhanced ARE gene expression in HepG2 cells by ~10-fold, measured by a luciferase reporter assay [185]. Although binding activity was reduced, the significant increase in cell permeability was sufficient to enhance activity. This represents a common issue with peptides, as their large mass and increased polarity hinders intracellular delivery. Other CPP strategies have been reported, including the PPI peptide TAT-14, which was previously reported by the Searcey lab at UEA. TAT-14 comprises an 'LDEETGE' motif with N-terminal TAT conjugation. In THP-1 monocytes, TAT-14 (75 μM) increased NRF2 protein expression and increased HO-1 gene expression by 24-fold. Removing both the TAT and 'LDEETGE' sequence abolished activity, suggesting Keap1 binding occurs through the 'LDEETGE' and the TAT sequence provides sufficient cell penetration[186]. TAT-14 is discussed in more detail in subsequent sections, which forms the basis of the project here.

Several Keap1-NRF2 PPI inhibitors have been investigated with disease models *in vivo.* Findings indicate that NRF2/ARE pathway activation is protective in septic cardiomyopathy and ulcerative colitis (UC) mouse models. CPUY192018 is a small-molecule PPI inhibitor (**Figure 1.14**). Unlike electrophilic NRF2 activators, it directly disrupts Keap1-NRF2 binding rather than targeting Keap1 sensor cysteines. Using an FP assay, CPUY192018 was found to strongly bind Keap1 (IC_{50} of 14.4 nM) [187] and was later found to increase NRF2 levels and upregulate ARE–mediated gene expression in human kidney HK-2 cells [188]. In an ulcerative colitis (UC) mouse model, CPUY192018 significantly improved pathological symptoms, with reduced diarrhoea and rectal bleeding. Colon composition was improved, with a reduction in TNF-α, IL-6 and IL-1β concentrations in combination with reduced ROS levels [189].

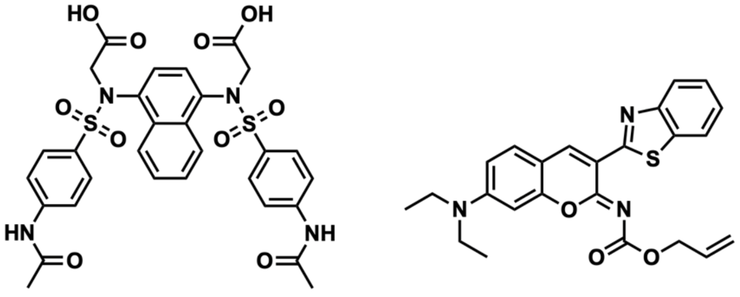

CPUY192018 **ZJ01**

Figure 1.14. Structure of small-molecule Keap1 PPI inhibitors.

ZJ01 is also a small-molecule PPI inhibitor (**Figure 1.14**), although it is reported to exhibit a far weaker binding affinity for Keap1 (K_d 48.1 μM, measured by SPR). In vivo, ZJ01 increased NRF2 nuclear translocation alongside upregulation of HO-1 and NQO1 mRNA, which are NRF2 target genes[190]. Molecular docking was also used to propose a binding mode within the ETGE pocket, suggesting potential contacts with six residues. In a mouse model of LPS-induced septic cardiomyopathy, ZJ01 administration increased nuclear NRF2 accumulation and suppressed pro-inflammatory cytokine release, including TNF-α, IL-1β and IL-6 [190]. Peptide Keap1-NRF2 PPI inhibitors such as LAS200813, a bicyclic peptide, have also been investigated *in vivo*. LAS200813 was found to bind Keap1 with sub-nanomolar affinity (IC_{50} of 0.73 nM) and upregulate NRF2-regulated ARE genes, NQO1 and SRXN1, in BEAS-2B human bronchial epithelial cells. *In vivo* administration to rats resulted in significant induction of HO1, NQO1 and SRXN1 mRNA within 6 h, which remained elevated at 24 h [191]. Collectively, these findings highlight the *in vivo* therapeutic relevance of targeting the Keap1/NRF2 pathway to reduce inflammation and improve disease pathology. Although Keap1 PPI inhibitors can activate NRF2 *in vitro* and *in vivo*, with promising activity in disease models, their therapeutic application is potentially hindered by inherent limitations. PPI inhibitors can suffer from poor cell permeability, which can be improved by CPP conjugation. Also, since PPI inhibition is reversible, sustained NRF2 activation may provide a challenge in the clinic. Therefore, new strategies should be explored with enhanced characteristics.

1.3 PROTACs: Targeted Protein Degradation as a Therapeutic Strategy

1.3.1 Mechanism of Action

Proteolysis-targeting chimeras (PROTACs) are a class of protein degraders that have advanced significantly since they were first reported in 2001 [192]. They are heterobifunctional molecules consisting of three structural elements: a ligand to bind the target protein of interest (POI), a ligand for an E3 ubiquitin ligase and a connecting linker (**Figure 1.15**). This design allows for simultaneous binding of the target protein and an E3 ubiquitin ligase (shortened to E3 ligase), forming a ternary complex (POI-PROTAC-E3 ligase). There are four types of E3 ligases, categorised by their catalytic domain, with Really Interesting New Gene (RING) the most widely recruited by PROTACs. The ternary complex brings the target protein and E3 ligase to proximity. Within the E3 ligase, the RING box protein 1 subunit (RBX1) recruits the E2 ubiquitin conjugating enzyme which ubiquitinates the target protein. PROTACs effectively hijack the ubiquitin-proteasome system (UPS) to mediate degradation [193].

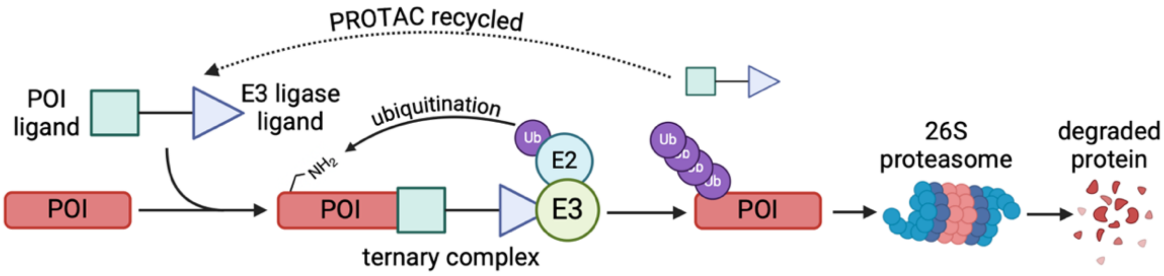

Figure 1.15. Generalised overview of PROTAC MOI (created using BioRender).

The UPS, alongside autophagy, is a major pathway for the maintenance of systemic proteostasis. This is achieved through selectively tagging damaged or superfluous proteins with ubiquitin, which are subsequently degraded. Ubiquitination involves a sequential, three enzyme cascade involving the ubiquitin activating enzyme (E1), the ubiquitin conjugating enzyme (E2) and the ubiquitin ligase (E3) (**Figure 1.16**) [194]. Ubiquitin, a 76 amino acid protein, is first adenylated at its C-terminal glycine and undergoes thioesterification with a cysteine residue on the E1 enzyme, forming a lysine isopeptide bond [195]. Activated ubiquitin is transferred via trans-esterification to an E2 enzyme cysteine [196]. Finally, E3 ligase catalyses the transfer of ubiquitin from the E2 enzyme to lysine residues of the target protein [197]. PROTACs exploit this final reaction by assembling the PROTAC-E3 ligase complex which brings the E3 ligase into close proximity with the target protein, promoting E2 ubiquitination of the target protein [193]. Subsequent rounds of ubiquitination occur through each ubiquitin Lys48 forming a polyubiquitinated chain (four monomers long) which is recognised by the 26S proteasome. Upon recognition, the 26S proteasome unfolds and degrades the protein within its 20S core particle [198] [199]. Deubiquitinating enzymes (DUBs) catalyse the removal of ubiquitin before degradation, allowing for it to be recycled within the system [200].

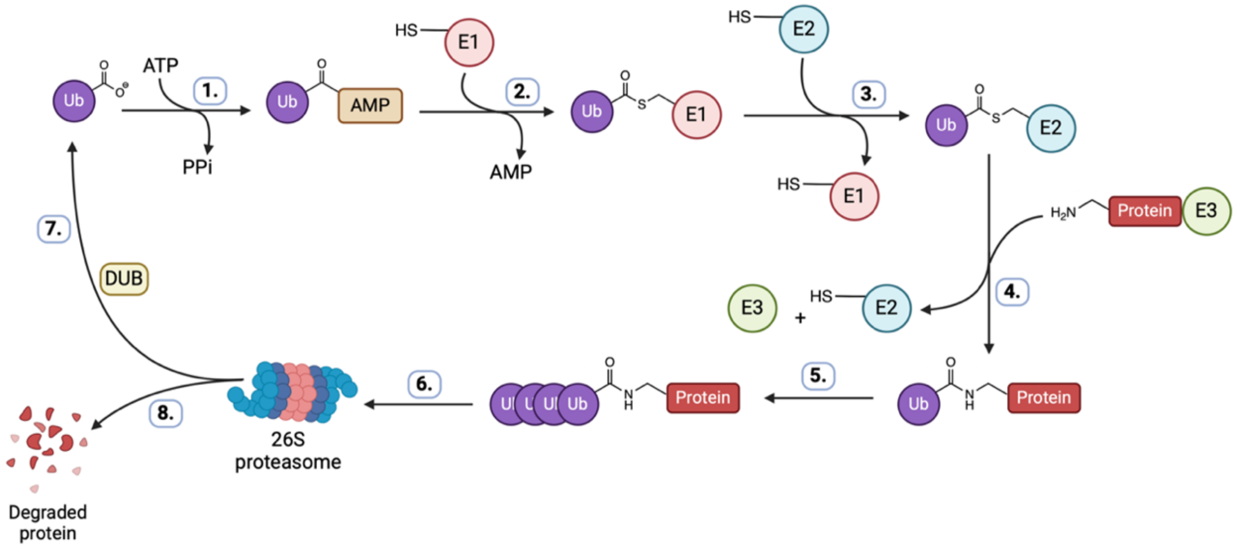

Figure 1.16. Overview of UPS mediated protein degradation (created using BioRender).

1.3.2 Recent Developments with PROTACs

The first reported PROTAC was designed with ovalicin, a small-molecule methionine aminopeptidase-2 (MetAP-2) inhibitor, with a IκBα-derived peptide fragment which recruits β-TRCP to form the E3 ubiquitin ligase complex. MetAP-2 was only found to be ubiquitinated by the PROTAC which resulted in its degradation *in vitro*, providing the first proof of concept [192]. Since then, PROTACs have been shown to degrade a wide range of targets using various E3 ligase ligands. The most widely employed are those which recruit von Hippel-Lindau (VHL) or cereblon (CRBN) proteins, which account for the majority of PROTACs in academia and industry.

The VHL protein is the substrate receptor for the Cullin2(CUL2)/RING E3 ligase complex (CRL2/VHL). CUL2 forms the scaffold for the RING finger protein subunit RBX1 to recruit the E2 enzyme. VHL contains a pocket found to bind Hyp564 of hydroxylated HIF-1 [201]. VHL-recruiting small-molecules such as VH032, and VH298 mimic this binding (**Figure 1.17**).

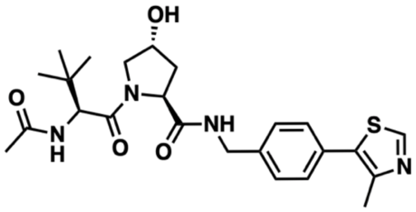

VH032

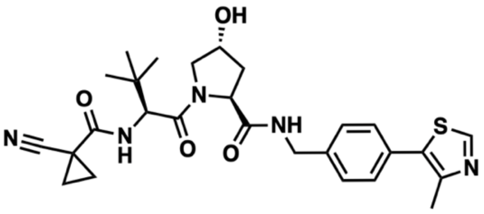

VH298

Figure 1.17. Structure of VHL-recruiting ligands

Crystal structures show they both occupy the same pocket of VHL, forming hydrogen bonds with Ser111, His115, His110 and Tyr98, with Phe91, Ile109 and Tyr112 providing hydrophobic interactions [202] [203]. In 2017, Gadd *et al.* resolved the first PROTAC ternary complex co-crystal structure of a VH032-based PROTAC (MZ1) with VHL and its target, a BET family protein, bromodomain-containing 4 (BRD4) (PDB:5T35) [204]. As expected, MZ1 bound VHL in the Hyp564-recognising pocket. Formation of the ternary complex identified *de novo* interactions between BRD4 and VHL. Electrostatic bonds between BRD4 Asp381 and Glu383 with VHL Arg107 and Arg108 'zipped' the proteins together, with an addition BRD4 Glu438 hydrogen bond to VHL Arg69 (see **Figure 1.18**).

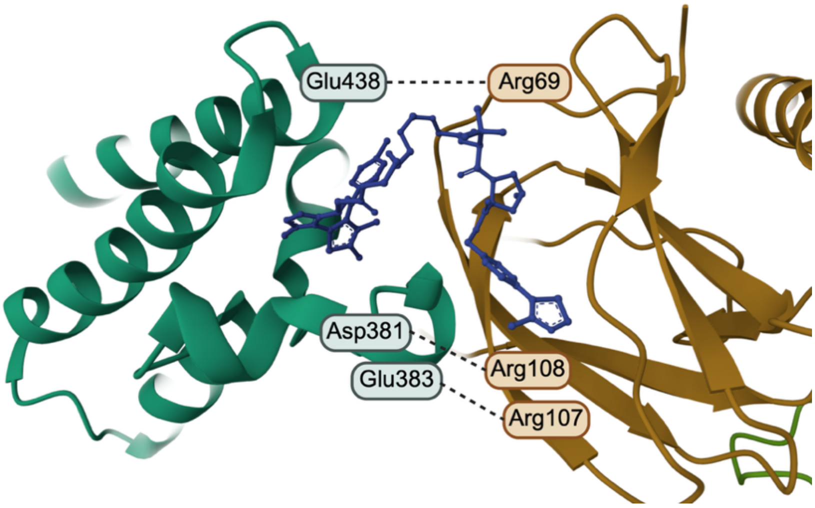

Figure 1.18. Crystal structure of MZ1 (blue) in complex with VHL (brown) and BRD4 (green) with VHL/BRD4 interactions. (PDB 5T35) (created using BioRender) [204].

These interactions are vital for ternary complex formation, as MZ1/VHL (K_d 67 nM) compared to BRD4/MZ1/VHL (K_d 4.4 nM) shows VHL binds 15-fold more tightly when BRD4 is already bound, illustrating a positive cooperative binding effect [204]. MZ1 was found to degrade BRD4 in various brain tumour cell lines, inhibiting growth of U251 cells (IC_{50} of 0.47 µM) [205]. MZ1 was developed further by introducing a cyclised linker, forming a macrocyclic PROTAC (macroPROTAC-1). The crystal structure (PDB:5T35) shows this induced more favourable interactions, increasing binding affinity as a ternary complex compared to MZ1. This resulted in BRD4 degradation in HeLa cells (DC_{50} 25-125 nM, depending on BRD4 isoforms) [206]. ARV-771 is a VH032-derivative PROTAC which also targets other BRD proteins. In castration-resistant prostate cancer cell lines, ARV-771 degraded BRD proteins with DC_{50} <5 nM and suppressed a cancer oncogene with an IC_{50} <1 nM. Although tumour regression was found *in vivo*, ARV-771 was not taken forward [207].

Other VHL-recruiting PROTACs have entered clinical trials for various cancer types, including DT2216 and KT-333 (**Table 1.4**). DT-2216 is a VHL-recruiting PROTAC which contains

ABT263, a small-molecule inhibitor of BCL-XL. ABT263 was previously found to inhibit BCL-XL, inducing tumour regression. It completed Phase I clinical trials but thrombocytopenia was a major side effect [208]. DT-2216 was found to be more potent than ABT263 in various cancer cell lines and inhibited xenograft tumour progression in mouse models without causing significant thrombocytopenia [209] [210]. It since completed Phase I clinical trials, again with less significant thrombocytopenia found (NCT04886622) [211]. It is now being investigated in combination therapies (NCT06620302, NCT06964009). KT-333 is a VHL-recruiting PROTAC which targets signal transducer and activator of transcription 3 (STAT3). Aberrant activation of STAT3 is associated with various cancers and can be targeted as an oncological therapeutic approach [212]. It entered Phase I clinical trials with preliminary data suggesting it is well tolerated and degrades STAT3 effectively (NCT05225584) [213]. ARV-471 (Vepdegestrant) is arguably the most successful PROTAC to date, recruiting CRBN and targeting oestrogen receptors (ER) in ER$^+$/HER2$^-$ breast cancer (**Table 1.4**). It was well tolerated and showed clinical benefits in Phase I/II clinical trials (NCT05654623) and is currently in phase III trials (NCT05909397) (NCT05654623) [214].

PROTAC	E3 ligase recruiter	Current clinical stage	Target	Disease in clinical trials
DT2216	VHL	Phase I/II (NCT06620302) (NCT06964009) (NCT04886622)	BCL-XL	Relapse/ refractory cancers
KTT-33	VHL	Phase I (NCT05225584)	STAT3	STAT3-driven solid tumours and lymphoma
ARV-471	VHL	Phase III recruiting	Estrogen receptor (ER)	ER-driven breast cancer
ARV-110	CRBN	Phase I/II complete	Androgen receptor (AR)	mCRPC
BGB-16673	Unspecified	Phase I/II (NCT05006716)	BTK (WT and mutants)	B-cell malignancies

Table 1.4. Examples of PROTACs in clinical development.

Cereblon (CRBN) is another protein which functions as a substrate receptor for the CUL4/RING/E3 ligase complex (CRL4/CRBN), in contrast to VHL which uses CUL2. Assembly of the complex recruits an E2 ligase which catalyses target ubiquitination. CRBN contains a pocket which binds immunomodulatory drugs (IMiDs) such as thalidomide, lenalidomide and other derivatives. This binding site can be exploited for PROTAC design, using these IMiDs as CRBN ligands. The co-crystal structure of a thalidomide-recruiting PROTAC revealed *de novo* interactions between the target and CRBN and thalidomide bound to CRBN through the expected IMiD binding pocket [215]. There are various CRBN-recruiting PROTACs in clinical trials, including ARV-110 and BGB-16673 (**Table 1.4**). ARV-110 degrades the androgen receptor (AR) in various prostate cancer mouse models with a (DC_{50} of 1 nM) [216]. In a Phase I/II clinical trial for mCRPC, it was well tolerated and clinically beneficial (NCT03888612) [217]. BGB-16673 (unspecified E3 ligase recruiting) targets wild-type and mutant BTK proteins found in B-cell malignancies. It is currently being evaluated in an ongoing phase I/II clinical trial (NCT05006716) and has shown good tolerability and clinically beneficial BTK degradation [218].

1.3.3 Advantages of PROTACs

PROTACs provide event-driven degradation over classical occupancy-based inhibition. Unlike inhibitors such as Keap1-NRF2 PPI inhibitors which require continuous target engagement, PROTACs act catalytically where each molecule can induce degradation and be recycled. This allows for sustained protein degradation at lower concentrations [219]. Traditional inhibitors are limited to proteins with well-defined binding pockets, reducing target selection. By requiring only surface binding interactions to form a ternary complex, PROTACs can inhibit ‘undruggable’ targets through degradation. Challenging targets for small-molecule inhibition such as BRD4 and STAT3 have been successfully degraded using PROTACs *in vivo* [220] [221]. Moreover, by degrading proteins, PROTACs can overcome target resistance found in cancer. ARV-110, an androgen receptor PROTAC, retains activity against mutant androgen receptors in prostate cancer [222]. Also, ARV-471 is reported to inhibit the growth of both wild-type and mutant breast cancer cells [223]. PROTACs enhance selectivity by driving assembly of the ternary complex between the target protein and an E3 ligase. This induced proximity creates novel *de novo* interactions that provide positive cooperativity and greater selectivity beyond solely target binding. The crystal structure of the PROTAC MZ1 with its target protein and E3 ligase revealed specific interactions upon ternary complex formation which conferred specificity over other structurally similar proteins (PDB:5T35) [204]. The modular design of PROTACs allows for optimisation for target selectivity with minor linker modifications significantly enhancing target binding, evident through SAR studies [224] [225]. E3 ligase ligand selection can also affect activity, depending on the expression of VHL or CRBN and the specific E3 ligase/POI interactions within the ternary complex [226]. Despite these benefits, PROTACs are plagued by poor bioavailability due to their high molecular weight, polarity and poor membrane permeability [227]. Strategies such as macrocyclization [206], rigid linkers [228], and nanoparticle delivery [229] have been found to mitigate these issues.

1.3.4 NRF2 Activating PROTACs

Although the application of PROTACs for NRF2 activation has been limited, several studies have successfully reported NRF2/ARE pathway activation through Keap1 degradation. Wang *et al.* (2022) developed KKP1, a peptide-based PROTAC containing two adjacent 'ETGE' motifs separated by a glycine linker, with a C-terminal CPP hPP10 (**Figure 1.19)** [230]**.**

Figure 1.19 The peptide sequence of KKP1.

This dual approach exploits the E3 ligase complex function of Keap1 to facilitate its own degradation. Molecular docking found KKP1 to form strong interactions with Kelch domain of Keap1, which was found in HSC-T6 cells as KKP1 induced Keap1 degradation with the highest penetration efficiency at 7.5 μM. Also, degradation was abolished by the proteasomal inhibitor MG132, suggesting UPS-mediated degradation occurs. KKP1 was found to upregulate HO-1 and GCLC protein expression, along with reducing pro-inflammatory TNF-α and IL-1β protein expression in HSC-T6 (rat hepatic cells). However, ARE gene expression was selective with no significant changes in NQO1 expression. Additionally, fibrotic markers were downregulated which indicates therapeutic potential in liver fibrosis [230].

In 2023, Park *et al.* reported SD2267, a typical small-molecule PROTAC comprised of a potent nanomolar Keap1 inhibitor/NRF2 activator [231] with the CRBN-recruiting thalidomide joined through an 8 carbon linker (**Figure 1.20**) [232]. The crystal structure of the Keap1 Kelch domain with the Keap1 inhibitor identified the binding site, which allowed for linker position to be directed (PDB:5FNU) [231]. The methoxy moiety was not found to have key interactions, therefore the linker was positioned here. In HepG2 (human liver) and AML12 (mouse liver) cell lines, SD2267 was rapidly taken up and degraded Keap1 (DC_{50} of 8.1 nM; 16.8 nM respectively). Degradation was confirmed to be mediated by the UPS, as treatment with MG132 (proteasome inhibitor) abolished Keap1 degradation.

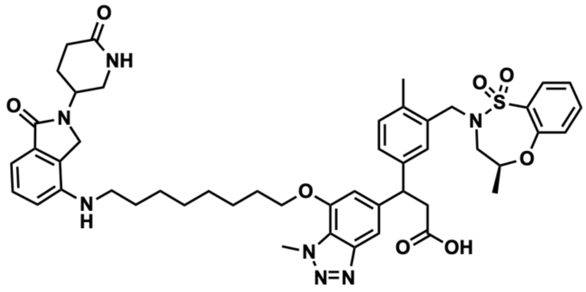

SD2267

Figure 1.20. Structure of SD2267

Also, inhibition of autophagy by chloroquine had no effect, indicating autophagy pathways were not involved. Keap1 degradation also required CRBN recruitment, as CRBN knockdown cells were not responsive. SD2267 resulted in NRF2 nuclear accumulation, measured by immunofluorescence, whilst upregulating numerous NRF2/ARE genes and rescuing AML12 cells from acetaminophen (APAP)-induced oxidative stress. In a liver injury mouse model (APAP induced), similar effects were found through NRF2/ARE pathway activation which attenuated hepatoxic effects. While both SD2267 and the Keap1 inhibitor (on its own) had nanomolar potency *in vitro*, SD2267 was found to have a superior pharmacokinetic profile *in vivo*. In orally dosed mice, SD2256 was found to increase C_{max} by ~1.4-fold and AUC_{last} by ~9-fold (normalised to dose). SD2267 also had a significantly longer half-life ($t_{1/2}$ 12 hr vs. 1.6 hr), finding the PROTAC approach provided superior ADME properties [232] [231].

Also in 2023, Chen *et al.* conducted a SAR study on a series of NRF2 activating PROTACs with varying linker lengths [233]. They all contained the CRBN-recruiting thalidomide with a small-molecule Keap1 inhibitor, which was previously reported (IC_{50} 270 nM) [231]. PROTAC8 (with a seven-carbon linker) was found to be the most potent (IC_{50} 66 nM) through a Keap1 HTRF biochemical assay. PROTACs with linkers with >7 carbons were found to enhance degradation. Therefore, PROTAC14 was designed with a seven-carbon linker, connecting to thalidomide though an amide linker (**Figure 1.21**). This replaced the previous oxy-acetamide linker in PROTAC8, which was found to be hydrolysis-sensitive [234]. PROTAC14 degraded Keap1 with a nanomolar concentration, similar to the previously discussed PROTAC SD2267 [232]. Both PROTACs contain thalidomide as the CRBN recruiter with the same Keap1 inhibitor to bind Keap1, with SD2267 having a shorter linker (by one carbon) (**Figure 1.20**). Mechanistic studies in HEK293T cells found PROTAC14 binds to both Keap1 and CRBN, as treatment with the Keap1 inhibitor or thalidomide abolished degradation. Combined with UPS-mediated degradation confirmed (as MG132 treatment abolished activity), it suggests formation of the tertiary complex promoted UPS degradation. NRF2/ARE pathway activation was compared for PROTAC14 and the Keap1 inhibitor (solely) *in vitro*, finding similar activity. In HEK293T (human embryonic kidney) and HCA7 (human colorectal cancer) cell lines, both increased ARE-regulated NRF2 gene expression, and in oxidative stress induced-BEAS-2B cells both improved cell viability. Label-free quantitative proteomics found PROTAC14 selectively degraded Keap1 and resulted in the expression of NRF2/ARE associated proteins including GCLC and GCLM. However, other non-antioxidant related proteins were also upregulated including Zinc finger protein 91 (ZFP91), and p62. ZFP91, an E3 ligase, is found to upregulate HIF-1α and promote colon cancer growth both *in vitro* and *in vivo* [235]; while overexpression of p62 is linked with breast cancer progression [236]. Therefore, these off-target effects would need to be addressed.

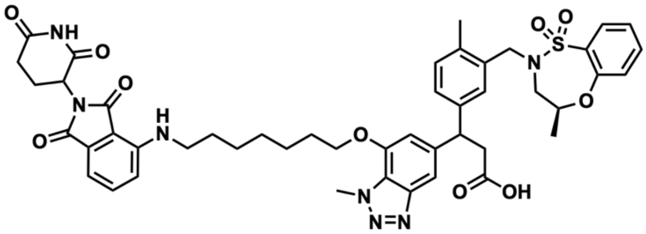

PROTAC14

Figure 1.21. Structure of PROTAC14

As outlined above, several NRF2 activating PROTACs have demonstrated the ability to degrade Keap1, upregulate ARE genes and attenuate inflammation with activity found at nanomolar and low micromolar concentrations. Together, these studies provide evidence that Keap1 degradation presents a compelling strategy for NRF2 activation. Given the novelty of the approach, the lack of reported NRF2 activating PROTACs in the literature and early evidence of therapeutic relevance, it provides an area for further development. It is hypothesised that conjugation of a peptide CPP inhibitor of the Keap1/NRF2 PPI (TAT-14) to the VHL-recruiting ligand VH032 could generate a PROTAC capable of binding and degrading Keap1. Through ternary complex formation (VHL-PROTAC-Keap1), VHL could recruit the CUL2-RBX1 E3 ligase complex to ubiquitinate Keap1, marking it for degradation. The catalytic degradation is expected to stabilise NRF2 more effectively than occupancy-driven inhibition by TAT-14 alone, therefore enhancing the induction of ARE-regulated genes such as HO-1 and NQO1. The design and synthesis of a hybrid peptide-small molecule PROTAC represents a novel approach to activating NRF2 with potential therapeutic benefits in inflammatory disease.

1.4 Aims and Objectives

1.4.1 Overall Aim

To synthesise and evaluate the biological activity of TAT-14 and PROTAC derivatives designed to degrade Keap1, to assess their efficacy in activating the NRF2/ARE pathway *in vitro*.

1.4.2 Objectives

1. To synthesise TAT-14 following the procedure reported by Steel *et al.* [186].

2. To validate the biological activity of TAT-14 in THP-1 cells by assessing NRF2 protein expression (by Western blot), induction of ARE-regulated HO-1 gene expression (by RT-qPCR) and cell viability (by MTS).

3. To synthesise the VHL-recruiting ligand VH032 following the procedure reported by Yan *et al.* [237].

4. To synthesise a Keap1-degrading PROTAC by conjugating TAT-14 to VH032 via a suitable linker.

5. To determine the biological activity of the PROTAC in THP-1 cells by assessing HO-1 and NQO1 gene induction (by RT-qPCR) and effects on cell viability (MTS).

Chapter 2 – TAT-14

2.1 TAT-14 Discovery

Previous work conducted in our lab by Steel *et al.*[186] involved investigating a series of peptides designed to disrupt the NRF2/Keap1 PPI interaction, activate the NRF2/ARE pathway and potentially reduce inflammation. Three lead peptides, designated TAT-10, TAT-14 and TAT-16, were synthesised with each comprising an NRF2-derived sequence conjugated at the N-terminus to a trans-activator of transcription (TAT) cell-penetrating peptide (CPP) (**Figure 2.1**).

TAT-10: YGRKKRRQRRR^{76}LDEETGEFLP^{85}

TAT-14: YGRKKRRQRRR^{74}LQLDEETGEFLPIQ^{87}

TAT-16: YGRKKRRQRRR^{69}AFFAQLQLDEETGEFL^{84}

Figure 2.1. The sequence of TAT-10, TAT-14 and TAT-16 with the TAT sequence (blue) and Neh2 NRF2 derived sequence (red). Superscripts indicate the corresponding amino acid position in human NRF2 [186].

As outlined previously, peptide PPI inhibitors can target the Kelch domain of Keap1 at the same binding site occupied by the 'ETGE' motif within NRF2. Incorporation of the 'ETGE' motif, with flanking residues, allows for high-affinity binding to Keap1 and upregulation of NRF2/ARE gene expression [238]. The NRF2-derived peptide sequences of TAT-10, TAT-14 and TAT-16 are highlighted with the corresponding amino acid number of NRF2 (**Figure 2.1**). The addition of the TAT sequence, derived from the human immunodeficiency virus type 1 (HIV-1), is a common CPP strategy to increase cell permeability [239]. The TAT peptide contains clusters of positively charged lysine and arginine residues, which provide favourable electrostatic interactions with the negatively charged cell membrane. This allows the peptide, with its cargo, to enter the cell efficiently. Combined with its low toxicity, TAT has been used in peptide design in various *in vitro and in vivo* studies [240] [241].

TAT-14: YGRKKRRQRRR^{74}LQLDEETGEFLPIQ^{87}

TAT-14Sc: YGRKKRRQRRREFGTDIQLIEPQLE

14mer: ^{74}LQLDEETGEFLPIQ^{87}

Figure 2.2. The sequence of TAT-14, TAT-14Sc and 14mer peptides with the TAT sequence (blue) NRF2 derived sequence (red) and scrambled sequence (black) [186].

TAT-10, TAT-14 and TAT-16 were synthesised and investigated *in vitro*. In human monocytic THP-1 cells, 75 μM TAT-14 induced an 18-fold upregulation of HO-1 mRNA expression (by

RT-qPCR), whereas TAT-10 and TAT-16 (both 75 μM) had minimal effect. Also, an FP competition assay found TAT-14 to have superior Keap1 binding affinity (K_i of 3.6 nM) compared to the other peptides (TAT-10 K_i of 6.9 nM; TAT-16 K_i of 38.9 nM, unpublished PhD data, Richard Steel). Due to the high affinity with Keap1 and activation of the NRF2/ARE pathway, TAT-14 was investigated for effects on NRF2 protein expression. Two derivatives were designed as controls (**Figure 2.2**), the peptides TAT-14Sc contains a scrambled 'LDEETGEFL' sequence and the 14mer that lacks the TAT sequence. THP-1 cells were treated with 75 μM of each peptide to measure HO-1 mRNA expression by RT-qPCR. TAT-14 upregulated HO-1 mRNA expression by 24-fold, whereas TAT-14Sc and 14-mer had no significant effect. Since the 14-mer peptide had no effect on HO-1 expression, it suggests the TAT sequence is essential for efficient cellular uptake and NRF2/ARE activation. Furthermore, THP-1 cells treated with TAT-14 were found to increase NRF2 protein levels (by Western blot) without affecting NRF2 mRNA expression (by RT-qPCR) (unpublished PhD data, Richard Steel). This suggests NRF2 accumulation occurs through disrupting the Keap1/NRF2 interaction, rather than transcriptional upregulation of NRF2. Western blot analysis found TAT-14Sc peptide had no effect on NRF2 levels, which further suggests the NRF2 derived sequence is essential for activity. In LPS-induced THP-1 cells, a model of inflammation, TAT-14 was found to resolve inflammation, reducing TNF-α mRNA expression by 61% compared to basal cells. Furthermore, Cowan, who also conducted PhD research at UEA in the same lab, reported that treatment with 75 μM TAT-14 significantly upregulated HO-1 mRNA expression (30-fold), as well as NQO1 (5-fold) and Ferritin (2-fold) mRNA in THP-1 cells measured by RT-qPCR. In addition, in LPS-stimulated THP-1 cells, TAT-14 reduced TNF-α protein expression by 50% (ELISA), while TNF-α mRNA expression was decreased by 50% and IL-1β mRNA expression by 40% (RT-qPCR) [242]. This further provides evidence that TAT-14 both upregulates ARE-regulated genes and decreases pro-inflammatory gene expression. Taken together, it supports the use of NRF2 activation as a strategy to reduce inflammation.

2.2 TAT-14 Synthesis

To validate the reported results by Steel et al., TAT-14 was synthesised based on the optimised Fmoc-based, solid-phase peptide synthesis (SPPS) procedure reported, using an automated peptide-synthesiser (MultiSynTech Syro I) for improved efficiency. Since TAT-14 contains a C-terminal Gln amino acid, a preloaded Wang resin with a 9-fluorenylmethoxycarbonyl (Fmoc) protected Gln was selected (**Figure 2.3**). Wang resin is a polystyrene-based support commonly used for peptide synthesis, which is either unloaded or preloaded with an amino acid. The resin joins glutamine through an ester linker, which is stable during synthesis but can be cleaved to produce a C-terminal free acid. The side chain of glutamine is also protected to prevent side reactions (**Figure 2.3**). The triphenylmethyl (Trt) protecting group is stable under basic amide coupling conditions but acid liable, which allows for removal upon completion of the synthesis.

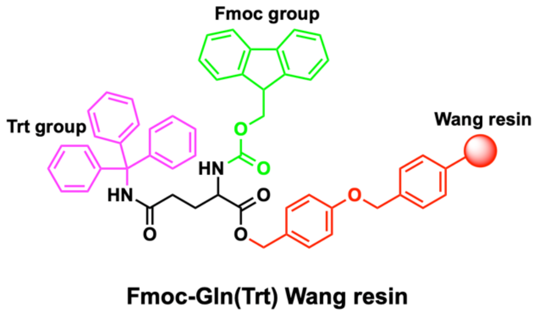

Figure 2.3. The pre-loaded resin used to synthesise TAT-14 with the resin (red), Fmoc protected amine group (green), Trt protected side chain (pink) and glutamine (black).

The synthesis involves a series of Fmoc deprotection and amide coupling reactions (**Scheme 2.1**). This allows for the systematic elongation of the peptide chain, building onto the C-terminal with each incoming amino acid forming the N-terminal, in a C- to N-terminus direction.

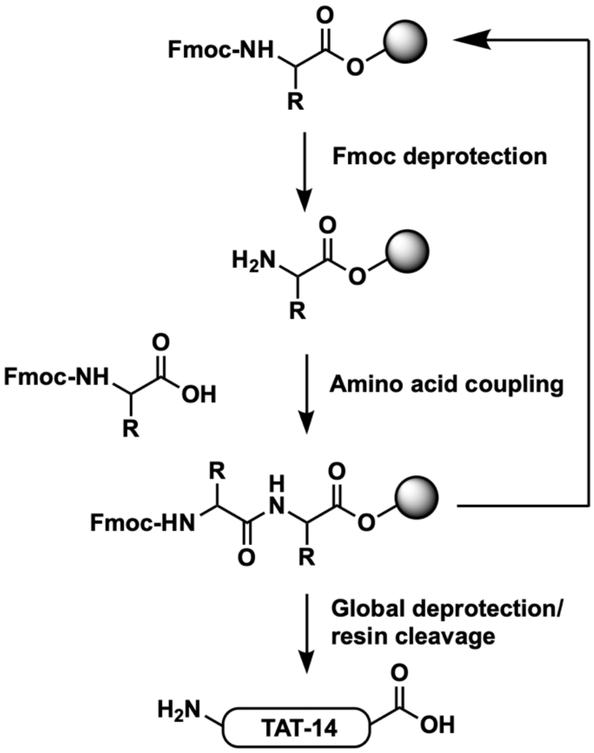

Scheme 2.1. An overview of the Fmoc-based procedure for HATU amino acid couplings, with final deprotection and cleavage to form TAT-14.

Once the resin was swollen in DMF, to expand its surface area and improve efficiency, it was loaded onto the synthesiser with the reagents and protected amino acids. The initial reaction involves removing the Fmoc group from pre-loaded resin glutamine, which was completed by treating with the base piperidine. Piperidine deprotonates the fluorene ring system, followed by elimination of the Fmoc group (**Scheme 2.2**). After washing away the byproducts, this produces a free amine to react with the incoming amino acid (isoleucine).

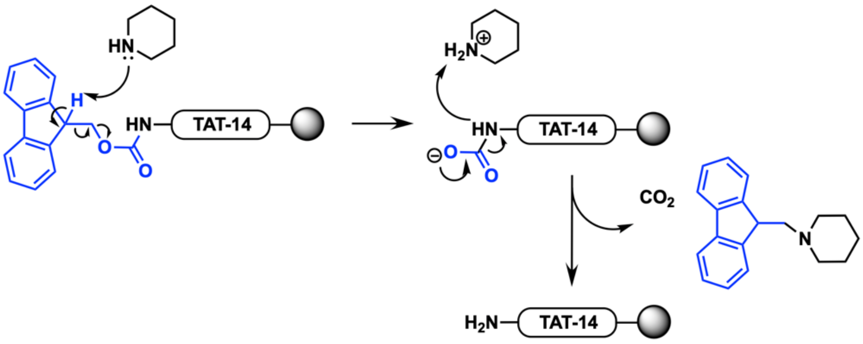

Scheme 2.2 Fmoc deprotection of amino acids with piperidine (in blue).

The next amino acid (isoleucine) has a free carboxylic acid which is coupled with the deprotected amine group of the N-terminal amino acid. Couplings were performed with HBTU, HOBt and DIPEA. The base DIPEA, deprotonates the incoming amino acid (**Scheme 2.3**). This allows the carboxylate to attack HBTU to form an ester intermediate. The addition of HOBt reacts rapidly with the intermediate to form the active ester, helping to reduce racemisation. The resin bound amine attacks the active ester to form a peptide bond. This was repeated for each amino acid coupling to form the TAT-14 peptide chain. Synthesis took 2.5 days and was periodically monitored.

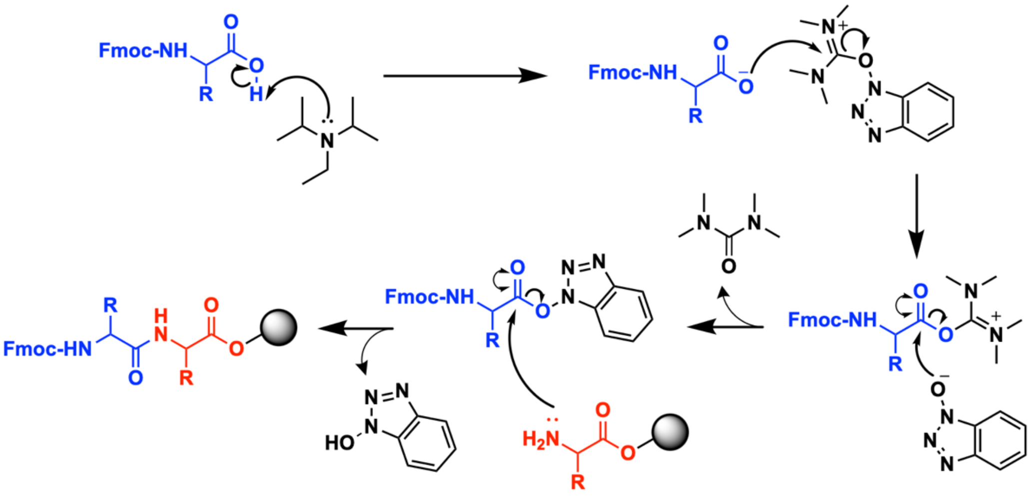

Scheme 2.3. Amino acid coupling between the resin bound amino acid (red) and the incoming amino acid (blue) with DIPEA and HBTU/HOBT.

Following completion of the TAT-14 sequence and the final Fmoc deprotection of the N-terminal amino acid (tyrosine), the peptide was cleaved from the resin. Cleavage of the peptide from the resin and removal of the side chain protecting groups was achieved with the strongly acidic cleavage cocktail of trifluoracetic acid (TFA), water and triisopropylsaline (TIPS) (95:5:5). The acid cleaves the resin-peptide ester linkage while simultaneously removing the acid-liable protecting groups (such as Boc, Pbf and Trt). Water and TIPS act as scavengers to neutralise reactive species and minimise side reactions. Upon completion, TFA was removed under a flow of N_2 and the peptide was precipitated in diethyl ether. The crude peptide was purified by reverse-phase flash chromatography, and the resulting fractions were collected based on 214 nm UV activity. A major peak formed which was suspected to be TAT-14, but the peak was wide, therefore multiple fractions within the peak were collected for HPLC analysis. One fraction was suspected to contain TAT-14, as the HPLC trace revealed one major peak (tR = 9.4) (**Figure 2.4**). MALDI-TOF was performed to confirm the mass, the expected mass was 3172.7 (M + H) and a major peak formed at 3172.10. To further confirm, electrospray ionisation mass spectrometry (ESI-MS) was performed. Peaks formed at 1058.6 and 1587.6 m/z, corresponding to TAT-14 adduct formation (M+2H+Na) and (M+H+Na). The isolated peptide was lyophilised to afford 17 mg of a white power, with a 9% percentage yield. Combined, the data suggested TAT-14 was successfully synthesised and purified to allow for *in vitro* assessment.

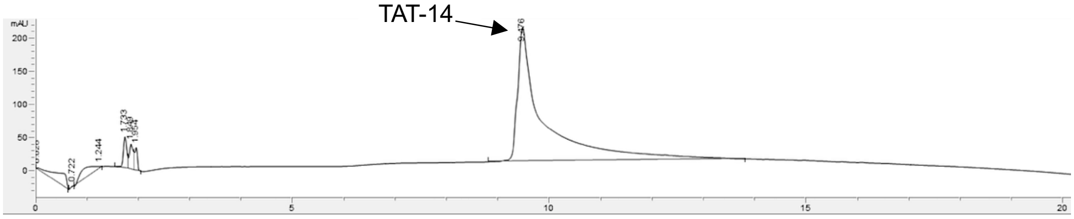

Figure 2.4. Purified HPLC trace of TAT-14

2.3 TAT 14 *in vitro* Assays

2.3.1 Western Blot

In vitro assays were conducted with the human monocytic cell line (THP-1), which is used as a model of monocytes during inflammation [243]. Since monocytes are a vital cellular component of inflammation, their modulation by TAT-14 provides evidence of inflammation control. Western blot was performed to assess NRF2 protein expression in THP-1 cells treated with TAT-14, dimethyl fumarate (DMF) or DMSO (vehicle control). Since all treatments were dissolved in DMSO, it was included as a control. As discussed previously, dimethyl fumarate

(DMF) is a potent NRF2 activator which disrupts the Keap1/NRF2 interaction. It has been previously shown to increase NRF2 protein levels in THP-1 cells (whilst having no effect on NRF2 mRNA expression) [244] [186]. Therefore, it was used as a positive control. THP-1 cells were treated with 75 µM TAT-14, 30 µM DMF or DMSO and incubated for 3 h. These were the same conditions used by Steel *et al.,* which allows for direct comparison. Protein extracts were prepared, protein concentration was quantified using a Nanodrop spectrophotometer and equivalent amounts of protein were loaded onto a gel and separated by SDS-PAGE. Proteins were transferred onto a PVDF membrane, blocked to minimise non-specific antibody binding and probed for NRF2 and the loading control β-tubulin. The membrane was incubated with primary antibodies for human NRF2 or β-tubulin and proteins visualised by chemiluminescence.

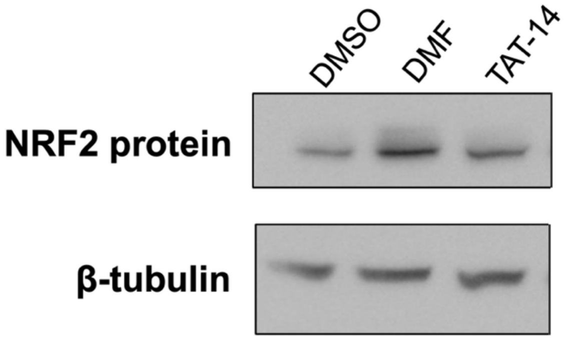

Figure 2.5. The effects of the NRF2 activators, DMF and TAT-14, on NRF2 expression in THP-1 cells. ***$1x10^6$ THP-1 cells in complete media were treated with TAT-14 (75 µM), DMF (30 µM) and DMSO for 3 h prior to protein extraction. Equal amounts of protein samples were separated by SDS-PAGE, transferred to PVDF membrane and probed with NRF2 primary antibodies with β-tubulin as a loading control, followed by secondary HRP antibodies. Bands were visualised by chemiluminescence. n=1.***

Analysis of the blot (**Figure 2.5**) showed β-tubulin loading bands were of comparable intensity across all three lanes, with only minor streaking, indicating consistent protein loading and transfer. Densitometric analysis found that DMF induced a greater increase in NRF2 protein expression (1.85-fold) compared with TAT-14 (1.2-fold), relative to the DMSO control. This was expected as DMF is a potent, clinically approved NRF2 activator widely reported to upregulate NRF2 protein concentration *in vitro* in various cell lines [245] [244]. Similarly, Steel *et al.* previously reported TAT-14 increased NRF2 protein expression in the same cell line at an equivalent concentration [186]. Although an increase in NRF2 protein expression was found here, the overall band intensity across the blot appeared muted. Nanodrop protein quantification found minor nucleic acid contamination, indicated by a low 260/280 absorbance ratio, which may have resulted in an underestimation of the true protein concentration. Nevertheless, the consistency between β-tubulin band intensity suggests that protein loading, while low, was consistent.

2.3.2 RT-qPCR

To evaluate the transcriptional activation of the NRF2 target gene HO-1, mRNA expression was assessed by RT-qPCR. THP-1 cells were stimulated for 6 h with 75 or 100 μM TAT-14, 30 μM DMF or DMSO (vehicle control). Following treatment, total RNA was extracted following a phase separation protocol and concentrations assessed by Nanodrop. Reverse transcription was performed by combining sample RNA with reverse transcription mastermix, which was run on a PTC-100 thermal cycler. Synthesised cDNA was then amplified by RT-qPCR using SYBR Green mastermix with primers for HO-1 and GAPDH. GAPDH is a housekeeping gene which should have stable expression between treatment conditions, providing a baseline to compare target gene expression. Reactions were run on a QIAGEN Rotor-GeneQ 5 Plex system using a two-step cycling protocol. DNA amplification was monitored in real time by SYBR Green fluorescence. Relative expression was normalised to GAPDH and expressed as a fold change relative to the DMSO vehicle control.

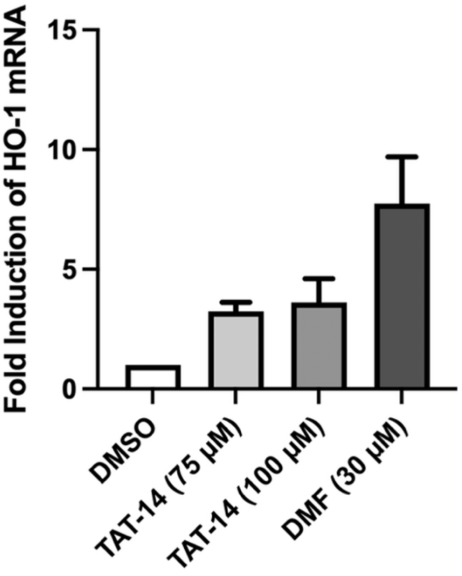

***Figure 2.6* Induction of HO-1 mRNA in THP-1 cells (*10x10^6*) seeded in a 12-well plate in complete media following 6 h treatment with TAT-14, DMF or DMSO (the vehicle control). Upon stimulation, total RNA was extracted and reverse transcribed into cDNA. HO-1 expression was measured by RT-qPCR with SYBR Green detection, normalised to GAPDH and relative expression calculated using the ΔΔCt method. Mean ± SEM, n=3.**

DMF 30 μM, the positive control, produced the strongest response with a 7-fold induction of HO-1 mRNA (**Figure 2.6**). This was expected as DMF has been widely reported to upregulate HO-1 mRNA expression *in vivo* and *in vitro* through NRF2 activation [246] [247] [248]. TAT-14 induced HO-1 mRNA expression with a ~3-fold increase at 75 μM with only a marginal further increase found at 100 μM. While Steel *et al.* did not evaluate activity above 75 μM, 100 μM was expected to increase HO-1 mRNA induction due to increased Keap1 inhibition. These findings suggest both DMF and TAT-14 disrupted the Keap1/NRF2 interaction which allowed for NRF2 to upregulate the ARE gene HO-1. However, the induction of HO-1 mRNA by TAT-14 was markedly reduced compared to previous reports. Steel *et al.* reported that TAT-14 increased HO-1 mRNA expression by 24-fold [186], while Cowan similarly reported a 20-fold induction of HO-1 mRNA at the same concentration [242]. Furthermore, TAT-14 at 75 μM and 100 μM treatments both produced similar induction of HO-1 mRNA expression. While Steel *et al.* did not assess TAT-14 over 75 μM, it was expected that 100 μM would further increase HO-1 mRNA expression. The reduced induction magnitude was attributed to cell responsiveness and RNA extraction. THP-1 cells with a later passage number, around passage 20, were used and perhaps were less responsive to treatment. Also, Nanodrop analysis found minor DNA and solvent contamination indicated by a >2 260/280 ratio and <2 260/230 ratio. This may have resulted in an underestimation of true RNA concentrations, which would explain the reduced HO-1 mRNA expression found for both TAT-14 and DMF treatment. Since DMF is a potent NRF2 activator which was expected to increase HO-1 mRNA induction significantly, it suggests the treatments were not the cause, but more likely cellular responsiveness or reduced RNA extraction. These results still show a positive response which suggests TAT-14 disrupts the Keap1-NRF2 complex and allows NRF2 to translocate into the nucleus to upregulate ARE genes. Therefore, it supports the use of TAT-14 in PROTAC design.

2.3.3 MTS Cell Viability Assay

To assess the cytotoxicity of TAT-14, an MTS cell viability assay was performed. DMF was used for comparison as an NRF2 activator. THP-1 cells were seeded at 1 x 10^6 cells/mL with 100 μL per well. Cells were treated with 1 μL DMSO (vehicle control), TAT-14 (75 μM) or DMF (30 μM). The cells were incubated for 24 h before addition of 10 μL MTS solution. Cells were further incubated for 3 h and absorbance at 495 nm was detected with a microplate reader. MTS analysis found that neither treatment with TAT-14 nor DMF resulted in significant reduction in cell viability compared to DMSO, which was expected (**Figure 2.7**). This is consistent with the findings by Steel *et al.,* who reported TAT-14 was not cytotoxic at concentrations up to 150 μM over 72 h in THP-1 cells. While DMF has been shown to be cytotoxic in various cell lines [249], the low concentration and shorter induction time was not sufficient to elicit a significant reduction in viability. This data validates the results by Steel *et al.* and supports the use of TAT-14 in PROTAC development.

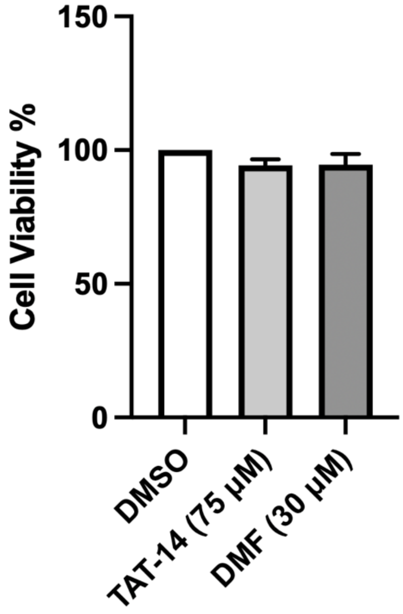

Figure 2.7. MTS cell viability assay was conducted with 1x10^5 THP-1 cells in a 96-well plate in complete media treated with TAT-14 and DMF in triplicates for 6 h. Upon stimulation, cells were treated with MTS solution for 3 h and incubated. Upon incubation, absorbance was measured at 492 nm using a microplate reader and cell viability was calculated by subtracting background absorbance and treatment conditions were normalised against the DMSO control. One-way ANOVA was performed followed by a post-hoc Dunnett's test to compare each treatment to the DMSO control. *Mean ± SEM, n=3.*

2.4 PROTAC1 Design

To enhance the activity of TAT-14, a PROTAC strategy was adopted. PROTAC1 was designed by conjugating TAT-14 to the VHL-recruiting ligand VH032 through a minimal PEG linker (**Figure 2.8**). PEG linkers are widely utilised in PROTAC design due to their conformational flexibility, polarity and reduced steric bulk which can support ternary complex formation [250]. Although the linker in PROTAC1 is short, it provides a suitable starting point to evaluate activity. Also, VH032 is a common VHL-recruiting ligand which has been reported in numerous PROTACs in the literature with nanomolar binding affinity [251] [202]. Since VH032 is well characterised, it was selected for PROTAC1 design. As discussed previously, several NRF2 activating PROTACs have previously been reported which demonstrate that targeted degradation of Keap1 is a suitable approach to activate the NRF2/ARE pathway, both *in vitro* and *in vivo* [232] [252]. Notably, KKP1 is a peptide-based PROTAC which incorporates 'ETGE' motifs to bind Keap1 with a CPP to enhance cellular uptake. KKP1 was found to degrade Keap1 and upregulate HO-1 and GCLC expression, supporting the relevance of a peptide-based Keap1 degradation strategy [230].

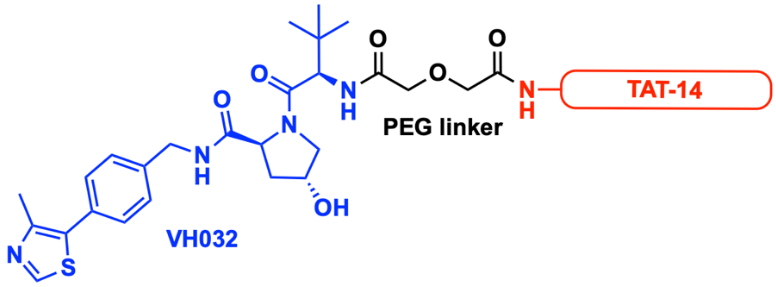

Figure 2.8. Structure of PROTAC1 with the VH032 ligand (blue), PEG linker (black) and TAT-14 (red) highlighted.

It was hypothesised that incorporating TAT-14 into PROTAC1 would allow it to function as the 'warhead' to bind Keap1 at the Kelch domain. VH032 would simultaneously recruit the VHL E3 ligase, which could promote formation of the ternary complex, leading to Keap1 ubiquitination and proteasomal degradation. By degrading Keap1, NRF2 levels would stabilise in the cytoplasm, allowing it to accumulate and translocate to the nucleus to promote transcription of ARE genes such as HO-1 and NQO1. Compared to TAT-14 alone, this strategy was expected to enhance activity and reduce the concentration required to activate the NRF2/ARE pathway. Since TAT-14 functions as a competitive inhibitor of the Keap1/NRF2 PPI interaction, it requires continuous occupancy of the Kelch domain and activity is reversible upon dissociation. Whereas PROTAC1 could degrade Keap1 in a catalytic manner, which would reduce the concentration required to induce NRF2/ARE-regulated gene expression.

2.5 VH032 Synthesis

To synthesise the PROTAC, VH032 was initially synthesised with a free amine group to enable subsequent coupling to the PEG linker. This strategy is frequently used to join acid linkers through amide bond formation [253]. The synthetic route was adapted from the protocol reported by Yan *et al.* [237], where the VH032 amine was synthesised on a 50g scale in a seven-step series (**Scheme 2.4**). The protocol achieved an overall yield of 65% with 97% purity without the need for chromatographic purification. Given the low cost and availability of the starting material combined with the high cost of commercially available VH032, it was initially synthesised on a gram scale to allow for PROTAC synthesis. Also, Yan *et al.* synthesised a BRD4 targeting PROTAC with synthesised VH032 amine. An identical PROTAC with commercially available VH032 was also produced, in which they found both PROTACs exhibited identical biological activity *in vitro*. This confirms the functional equivalence of the synthesised VH032 and supports the protocol reported.

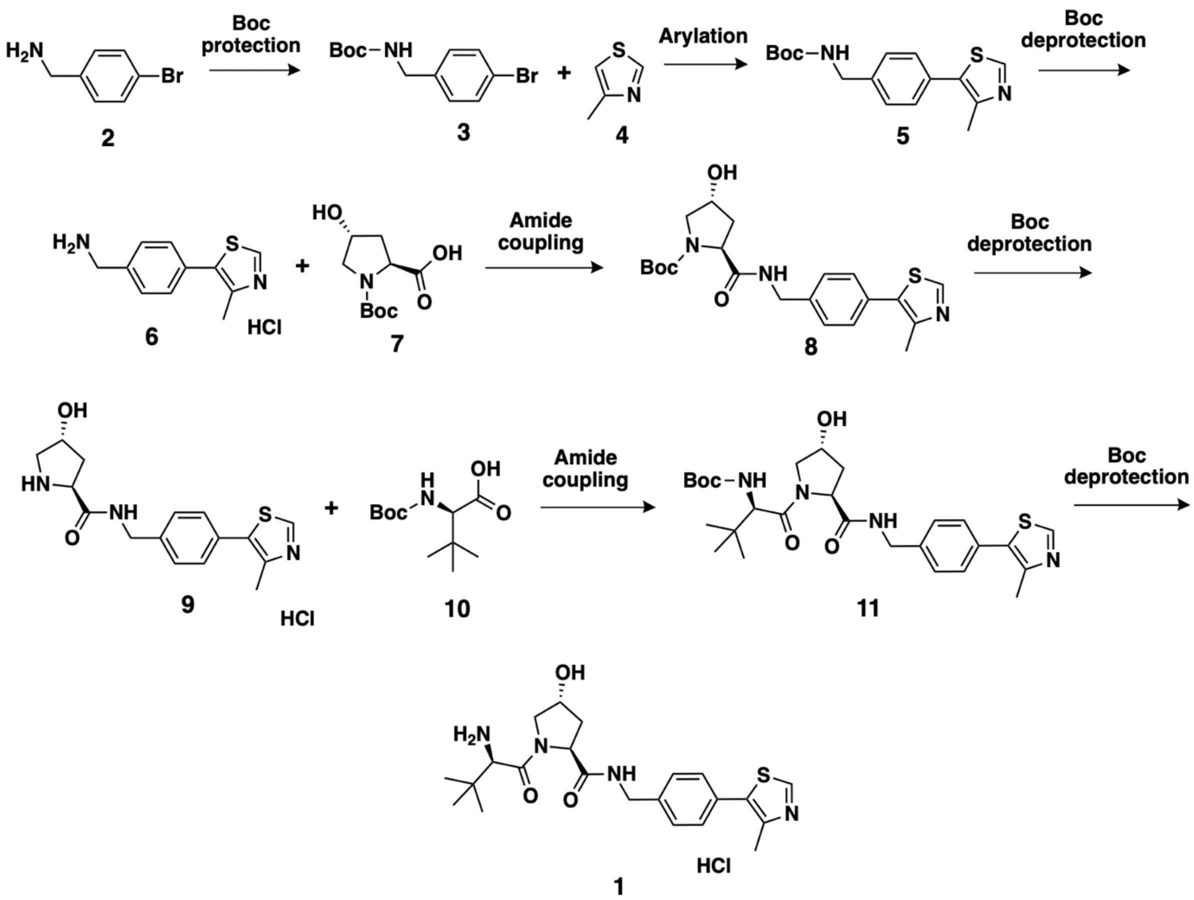

Scheme 2.4 Overall synthetic protocol for VH032 (1) synthesis.

Protection of 4-bromobenzylamine with a *tert*-Butoxycarbonyl (Boc) group

The first step involved *tert*-butoxycarbonyl (Boc) protection of the primary amine in 4-bromobenzylamine **2** (**Scheme 2.5**). This protected the amine from unwanted side-reactions in the subsequent step. The amine **2** was reacted with a slight excess of di-tertbutyl dicarbonate (Boc_2O) in the presence of sodium hydrogen carbonate in a biphasic aqueous/EtOAc system. In the reaction mechanism, the lone pair of the amine of **2** attacks the electrophilic carbonyl carbon of Boc_2O, forming a carbamate linkage.

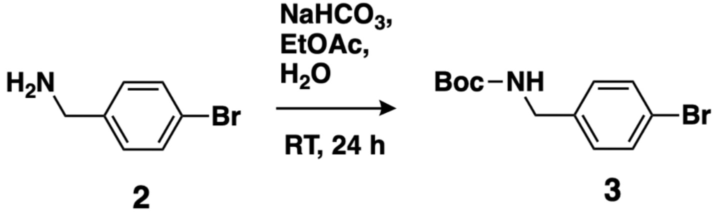

Scheme 2.5 Boc protection of 4-bromobenzylamine (2).

Sodium hydrogen carbonate acts as a mild base, deprotonating the amine upon carbamate formation. The *tert*-butyl carbonate leaving group decomposes to CO_2 and *tert*-butoxide (which is protonated to *tert*-butanol). Since CO_2 gas was released, the reaction was not performed in a closed system. The *tert*-butanol partitions into the aqueous phase during extraction and can be evaporated under reduced pressure. Upon mixing, a white precipitate formed immediately which fully dissolved after stirring overnight. TLC stained with ninhydrin confirmed the amine was protected, as **2** produced an orange colour whereas **3** was colourless. ^{1}H NMR analysis of **3** matched the literature data, showing all four characteristic signals. Residual EtOAc and water were present (singlets at 1.2 and 3.2 ppm respectively) which were also found in the reported spectrum. An additional singlet at 1.5 ppm was attributed to the CH_3 protons of residual tert-butanol. The crude percentage yield found was 94 %, which was similar to the reported yield from the literature (crude yield 117 %, corrected to 97 % of pure product). Therefore, crude **3** was taken forward.

Palladium-catalysed arylation of compound 3 with 4-methyltriazole

The next step involved a palladium catalysed selective C-H arylation of 4-methylthiazole **4** with crude **3** (**Scheme 2.6**). The reaction mechanism initially proceeds by oxidative addition of the aryl bromide to the palladium catalyst, forming an aryl-palladium complex (**Scheme 2.7**). This is followed by C-H activation at the C5 position of **4**, following a concerted metalation deprotonation (CMD) pathway. The C5 position is the most nucleophilic carbon, due to high electron density, which promotes regiospecific palladation [254].

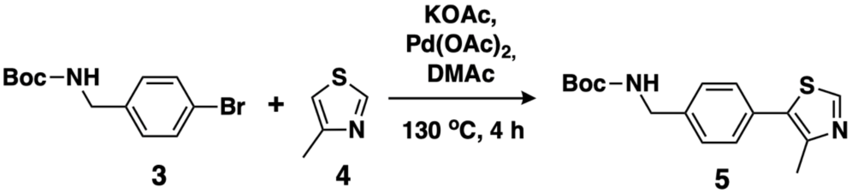

Scheme 2.6 Palladium-catalysed arylation of 4-methyl thiazole (4) with N-Boc-4-bromobenzylamine (3)

This forms a 6-membered intermediate, which is followed by reductive elimination which produces **5** and regenerates the palladium catalyst. Initial attempts were unsuccessful; therefore, measures were taken to reduce exposure to water and oxygen which were suspected to hinder the reaction. Compound **3** was dried by lyophilisation to remove residual water. The mixture of **3**, **4**, KOAc in DMAc was degassed with nitrogen after palladium catalyst addition. Whilst the reaction mixture was heated, it was kept under a nitrogen environment. By ensuring reduced exposure to oxygen and water, the reaction was successfully complete.

The reaction was challenging to monitor with TLC as the spot streaked, which made interpretation difficult. Upon extraction TLC was used to compare **3** and **5,** which produced distinct spots albeit with similar Rf values. Compound **3** had a slightly larger Rf value (0.67) than compound 5 (0.60), which was expected as compound **5** is slightly more polar. Crude **5** was taken forward for Boc deprotection.

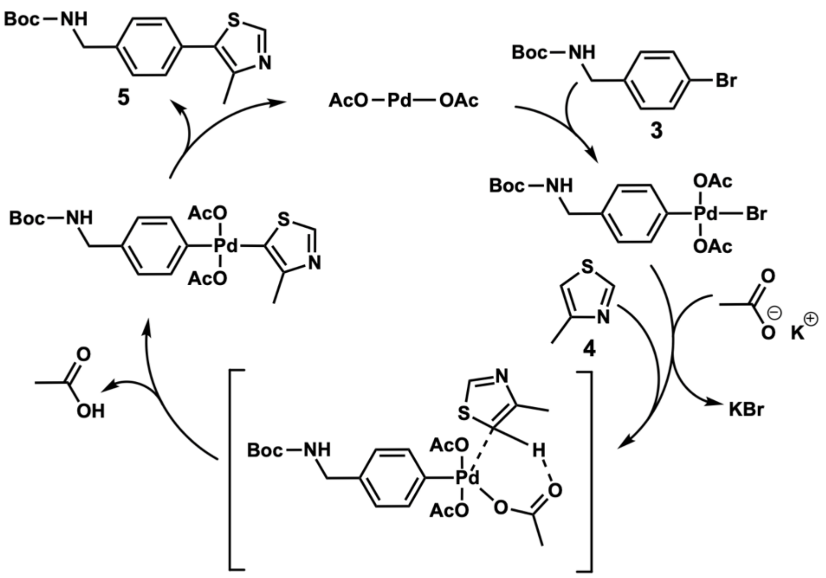

Scheme 2.7. Proposed catalytic cycle for the palladium-catalysed directed C-H arylation to yield (5)

Deprotection of compound 5 to generate the benzylamine 6

The next step involved the removal of the Boc protecting group from crude **5** under mild acidic conditions to yield the amine **6** as a HCl salt (**Scheme 2.8**). In the presence of HCl, the Boc carbonyl oxygen is protonated which promotes cleavage of the *tert*-butyl group, which leaves as a cation (**Scheme 2.9**). The resulting carbamic acid intermediate undergoes decarboxylation to release CO_2 gas, liberating the amine to yield **6**. Since CO_2 is produced, the reaction was not run in a closed system.

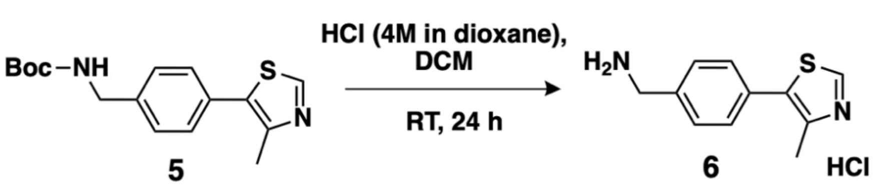

Scheme 2.8. Boc deprotection of 5 to yield the corresponding amine HCl (6)

The tert-butyl cation is trapped by chloride to produce *tert*-butyl chloride which is removed during work-up. Upon addition of HCl (4M in dioxane) to a solution of **5** in CH_2Cl_2, a yellow precipitate formed immediately. Since excess acid was used, it protonated the amine **6** to from a HCl salt insoluble in CH_2Cl_2. The reaction mixture was stirred overnight to ensure complete deprotection. The precipitate was washed, filtered and dried under reduced pressure to remove the *tert*-butyl chloride byproduct. The reaction was repeated multiple times which were successful. TLC showed complete consumption of **5** and the appearance of a new strongly polar spot for **6** which had minimal mobility on silica (with EtOAc/Hexane) which was expected. Ninhydrin staining gave an orange colour for **6**, confirming amine presence, whereas **5** had no colour change. ^{1}H NMR analysis confirmed the structure of **6**, with the absence of the tert-butyl singlet (1.4 ppm) and retention of all aromatic protons corresponding to the benzene and thiazole rings. A broad singlet (8.46 ppm) integrating to 3H was consistent with the protonated NH_3^+ of **6**. The spectrum matched the literature data, confirming successful Boc deprotection and **6** HCl salt formation. The two-step crude yield was 103 %, which matched the reported crude yield (103 %, corrected to 96% pure product). The apparent excess mass is attributed to residual solvent and minor impurities, therefore Crude **6** was taken forward for the next step.

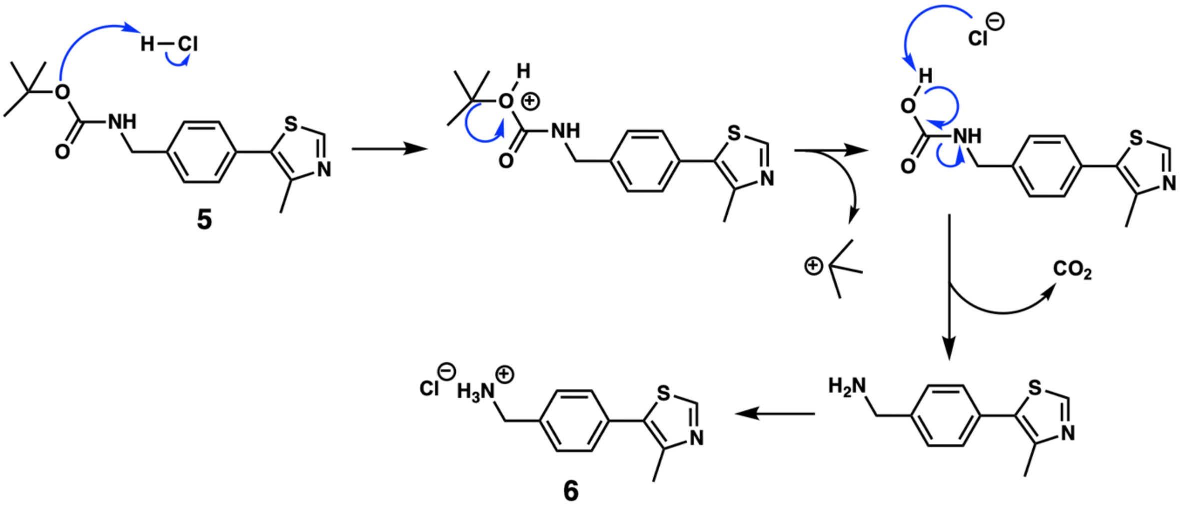

Scheme 2.9. Proposed mechanism of Boc deprotection of (5) to yield (6).

Coupling of Compound 6 with *N*-Boc-L-proline.

The next step involved an amide coupling reaction between the free amine of **6** with N-Boc-L-hydroxyproline **7** to form the amide **8** (**Scheme 2.10**). The reaction proceeds through initial deprotonation of carboxylic acid **7**, which attacks the HATU uronium central carbon to generate an uronium intermediate **7a** and liberates the HOAt anion (**Scheme 2.11**).

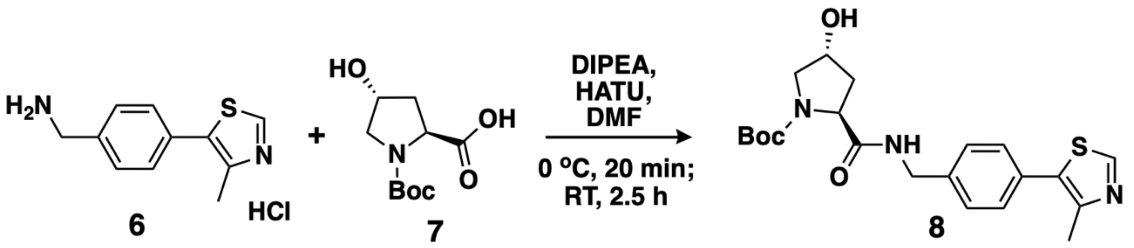

Scheme 2.10. Amide coupling of amine HCl (6) with Boc-protected hydroxyproline (7).

HOAt undergoes nucleophilic attack on the carbonyl of the uronium intermediate, generating the by-product tetramethylurea and forming the active ester **7b**. The HCl salt **6** is neutralised by DIPEA and then undergoes nucleophilic attack on the carbonyl carbon of the active ester **7**, which liberates HOAt as an anion and forms the amide bond of **8**. Initial attempts following the conditions of Yang *et al.,* (DMF/CH_2Cl_2 solvent mixture, TEA as base) were unsuccessful. Therefore, the conditions were modified based on a HATU/DIPEA protocol [255] with **6** and **7** (1 equiv. each), with HATU (1.1 equiv.) and DIPEA (3 equiv.). The acid **7** was first activated by stirring with HATU and DIPEA in DMF at 0°C for 10 min to promote active ester formation. Subsequently, the amine **6** was added and the reaction stirred for 2.5 h at RT under a nitrogen environment. The excess DIPEA used was expected to both neutralise the HCl salt of **6** and deprotonate the acid **7**. HATU is a common coupling reagent used in amide coupling reactions which reduces racemisation. Cooling the solution to 0°C was expected to further reduce potential racemisation.

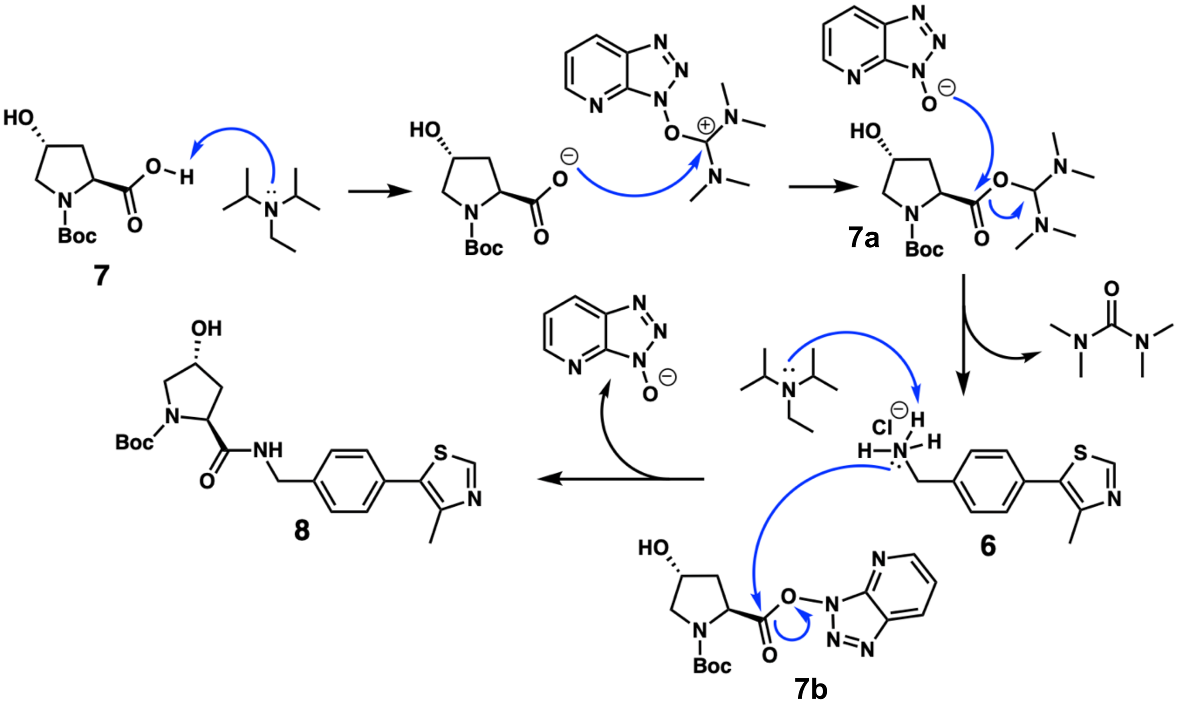

Scheme 2.11. Mechanism of HATU-mediated amide coupling between the acid (7) and amine (6).

Following the reaction, the mixture was washed with brine and $NaHCO_3$ to remove DMF and the by-products HOAt and tetramethylurea, then extracted into EtOAc. TLC analysis confirmed product formation, with the absence of colour after ninhydrin staining indicating complete consumption of the amine. Crude **8** was dried with sodium sulphate, concentrated under vacuum and used directly for subsequent Boc deprotection.

Deprotection of Compound 8

The next step involved a Boc deprotection reaction under acidic conditions to liberate the free amine from **8** to produce **9** (**Scheme 2.12**). The Boc protecting group was removed from the hydroxyproline amine of **8** to allow subsequent amide coupling. The same acidic conditions were used, with HCL (4M in dioxane) used as the acid in a solution of dioxane and EtOAc. Upon addition of the acid, a precipitate formed immediate which was off-yellow and sticky. The reaction was allowed to stir overnight to promote complete deprotection. The precipitate was washed with EtOAc and dissolved in MeOH to allow for transfer. ^1H NMR analysis was consistent with the literature reported spectrum. Peaks were found to correspond to the benzene CH (7.59 and 7.53 ppm) and the thiazole methyl CH_3 (2.61 ppm) and thiazole CH (9.83 ppm). No *tert*-butyl Boc peak was present, suggesting successful deprotection. Also, the hydroxyproline signals were present from **7** (4.63, 3.45, 2.51 and 2.11 ppm) which suggest the amide coupling was successful. The crude percentage yield found (111 %) was similar to the reported crude yield (114 %, which was corrected to 94 % of pure product). The excess mass was attributed to residual solvent and minor impurities. Since the product was characterised by ^1H NMR and one major spot was found by TLC, crude **9** was taken forward.

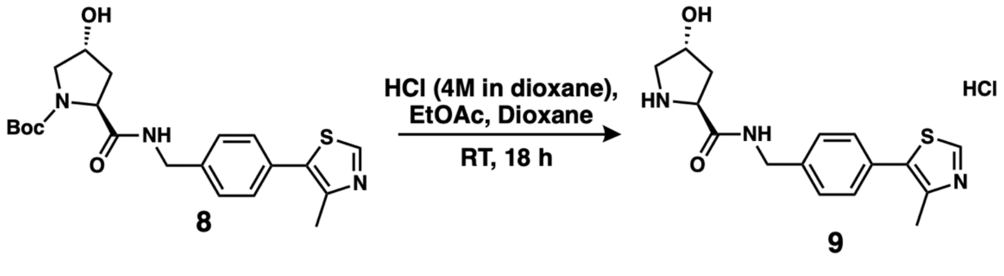

Scheme 2.12 Boc deprotection of 8 under mild acidic conditions

Reaction of Compound 9 with *N*-Boc-*tert*-leucine

The next step involved coupling the secondary amine, which was previously Boc protected, of **9** with the carboxylic acid of *N*-Boc-*tert*-leucine **10** to afford the amide **11 (Scheme 2.13)**. In a cooled solution of CH_2Cl_2, **10**, DIPEA and HATU were mixed for 10 min to initially form the active ester. The amine **9** was added and the reaction mixture was stirred overnight. The work up involved washing with aqueous citric acid, saturated sodium hydrogen carbonate, water and brine to remove excess base and by-products. The organic phase was concentrated to produce a yellow oil which was used directly for the final step.

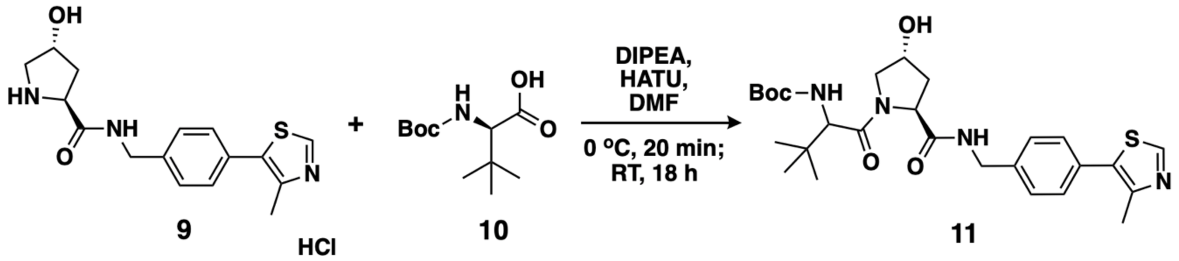

Scheme 2.13 Amide coupling of the amine 9 with the acid N-Boc-tert-leucine 10.

Deprotection of Compound 11 to generate the target VHL ligand (VH032)

The final step involved Boc deprotection of the primary amine of **11** under acidic conditions to produce the VH032 amine HCl salt (**1**) (**Scheme 2.14**). HCl (4M in dioxane) was added to a stirred solution of **11** in CH_2Cl_2. Upon addition, a yellow sticky solid precipitated out immediately. The reaction mixture was stirred overnight to ensure complete deprotection.

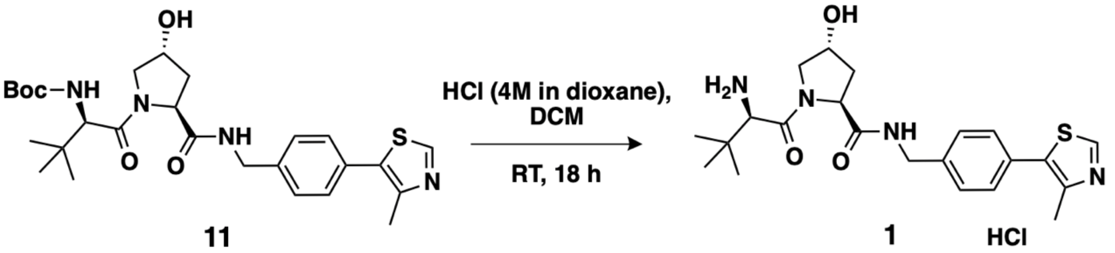

Scheme 2.14 Boc deprotection of the amine under mild acidic conditions (11) to yield (1).

The solid was washed with CH_2Cl_2 and filtered, then dissolved in MeOH to allow for transfer. TLC found formation of a new major spot which was suspected to be **1.** The initial attempt was successful, however purification by normal-phase flash chromatography resulted in significant product loss which was suspected to stick to the silica. Therefore, for the second attempt, crude **1** was taken forward for PROTAC synthesis without further purification. ^{1}H NMR confirmed the structure as the spectra matched the reported literature. Retention of the thiazole moiety was evident by a singlet for the thiazole CH (8.78 ppm) and the methyl singlet (2.37 ppm).

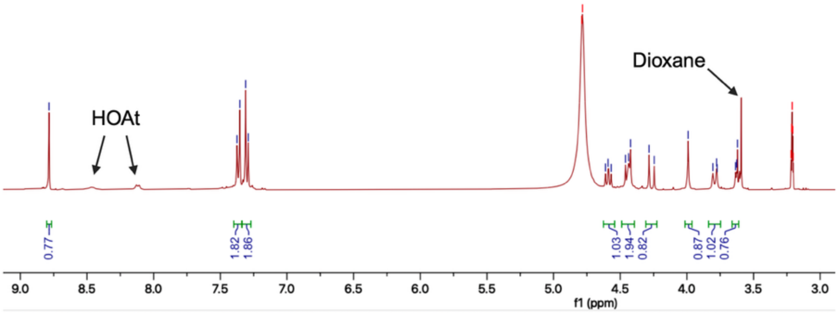

Figure 2.9. Section of ^{1}H NMR of VH032 amine (1)

The benzene group formed two doublets (7.36 and 7.30 ppm) for the aromatic CH. Hydroxyproline was also confirmed between 4.63 – 3.61 ppm, while the *tert*-leucine was identified by the *tert*-butyl singlet (1.03 ppm). The absence of the *tert*-butyl singlet associated with the Boc group (~1.4 ppm) confirmed the Boc deprotection was successful. A singlet (3.6 ppm) was suspected to be residual dioxane which was also found in the literature spectrum (**Figure 2.9**). The two small peaks are beginning to form between 8.0 – 8.5 ppm which were suspected to be from HOAt, the by-product from the previous amide coupling. The two-step crude yield was 101 %, which was higher than the reported crude yield from the literature (87 %, which was corrected to 74 % of pure product). The apparent excess mass was attributed to residual dioxane and minor impurities such as HOAt, as observed by ^{1}H NMR analysis. The crude VH032 **1** was taken forward for PROTAC synthesis.

2.6 PROTAC1 Development

The synthetic scheme for PROTAC1 was developed with two amide coupling reactions (**Scheme 2.15**). Diglycolic acid **12** would first be coupled to the N-terminal amine of TAT-14 to produce the TAT-14/PEG conjugate **13**. This would allow the amine of VH032 **1** to be coupled to the carboxylic acid of **13** to yield PROTAC1.

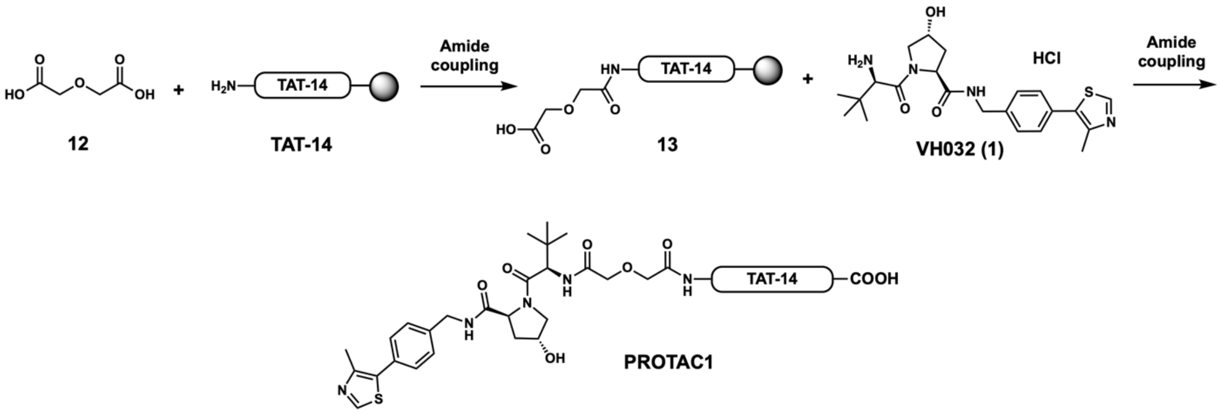

Scheme 2.15. PROTAC1 synthesis overview

Initially, TAT-14 was synthesised following the standard procedure on the Syro I automated peptide synthesiser. The peptide was synthesised on the Fmoc-Gln(Trt)-Wang resin (100 mg, loading capacity 0.61 mmol/g). Upon synthesis, the resin and side chain protecting groups were not cleaved. This would protect the peptide from side-reactions in the subsequent amide couplings. A small sample was cleaved to confirm the synthesis was successful. HPLC was performed and a major peak which was suspected to be TAT-14 (tR = 9.6 min) based on previous HPLC analysis of TAT-14. MALDI-TOF also confirmed the mass of TAT-14, the expected mass (+ve) was 3171.7 and the found mass was 3170.3.

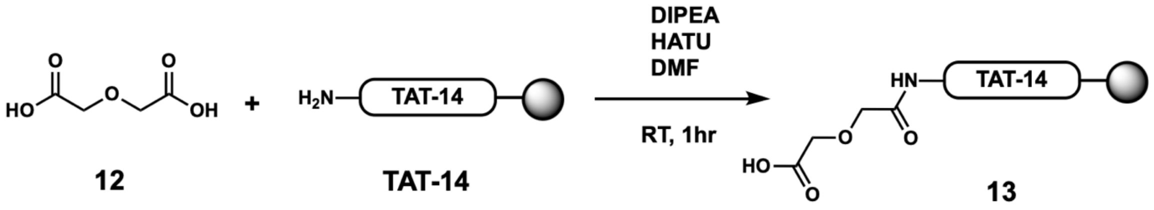

Scheme 2.16. Amide coupling between the TAT-14 amine and carboxylic acid (12).

The resin-bound TAT-14 amine was then coupled with the carboxylic acid **12** under standard HATU coupling conditions with a mild base (**Scheme 2.16**) [253]. Initially, **12** was stirred in DMF with subsequent addition of DIPEA and HATU which were in excess to drive the reaction forward. This was expected to initially deprotonate the acid and allow for HATU activation. The solution was added to the TAT-14 resin and shaken for 45 min. The reaction was monitored by the Kaiser (ninhydrin) test, which is a colourimetric assay to detect primary amines. Since the TAT-14 amine was coupling with the acid, a negative test would suggest reaction completion. A small resin sample was tested periodically, but a dark brown/orange colour persisted, which suggested the presence of amines. As a control, the Fmoc-Gln(trt) Wang resin on its own was tested and retuned the same colour. Since the amine on the resin is protected it should have remained colourless. Therefore, the test was inconclusive. A small resin sample was then cleaved to allow for characterisation. HPLC analysis found one new major peak (rT = 11.1 min) formed, which differed to the test TAT-14 trace (**Figure 2.10**). The sample of **13** was purified by semi-preparative HPLC and the isolated product was analysed by MALDI-TOF. The expected mass (3287.8) was not found in any fraction.

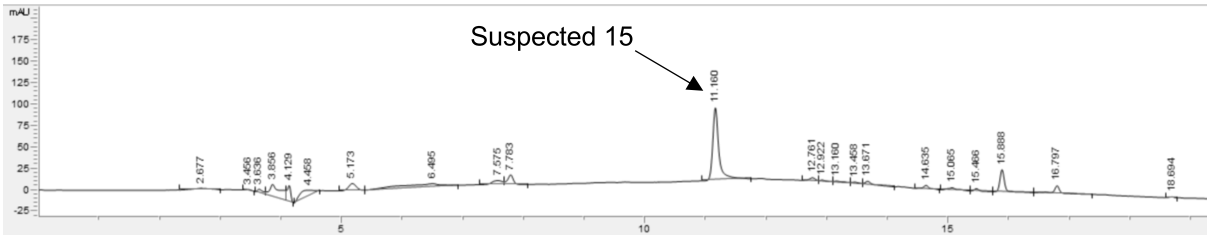

Figure 2.10. HPLC of crude TAT14/PEG conjugate (13)

Since the expected mass was not found but the major peak of the HPLC trace suggested a new product had formed, a new approach was taken. To not waste synthesised VH032 **1**, the subsequent amide coupling was attempted with benzylamine and the suspected TAT-14/PEG conjugate **13**. If successful and the expected mass was found, it would provide evidence that the previous reaction did work.

Initially, the TAT-14/PEG conjugate acid was combined with DIPEA then HATU to generate the active ester (**Scheme 2.17**). The reaction mixture was shaken for 45 min, then drained and repeated. The reagents and **14** were in excess (10 equiv.) to drive the reaction and double coupling was expected to promote complete synthesis. The TAT-14/PEG/benzylamine **15** was cleaved from the resin and deprotected. HPLC analysis of crude **15** found multiple peaks, which suggested the peptide had degraded. Also, MALDI-TOF analysis also did not find the expected mass (3376.8), multiple smaller peptide masses were found which suggests it was degraded. Purification by reverse-phase chromatography identified numerous fractions. MALDI-TOF analysis of these fractions found the mass of numerous smaller peptides, alongside TAT-14. This suggested neither reaction was successful, therefore a different approach was taken.

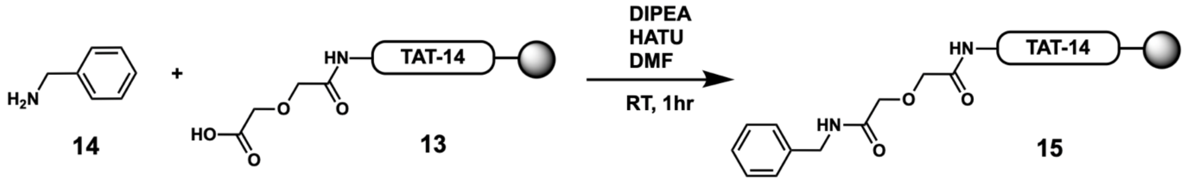

Scheme 2.17. Second amide coupling between benzylamine (14) and the TAT-14/PEG conjugate (13) to yield TAT-14/PEG/benzylamine (15).

2.7 PROTAC2 Development

Since PROTAC1 synthesis was unsuccessful, a new approach was taken by modifying the linker used. PROTAC2 was designed with a glutaric anhydride derived linker which would introduce a 5-carbon linker with a linking amide bond (**Figure 2.11**). Glutaric anhydride has been reported as a strategy for PROTAC linkage, due to the formation of a carboxylic acid which allows for VHL ligand addition[256] . The synthetic scheme was designed consisting of ring-opening acylation of glutaric anhydride **14** followed by amide coupling with VH032 **1** to yield PROTAC2 (**Scheme 2.18**).

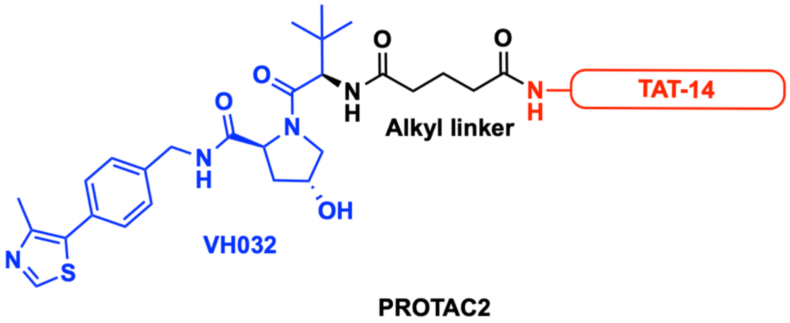

Figure 2.11. PROTAC2 design with VH032 (blue), alkyl linker (black) and TAT-14 (red).

Initially, TAT-14 was synthesised again using the same procedure previously described. A small sample of resin was cleaved and deprotected to allow for characterisation. HPLC analysis found one major peak (rT = 9.5) which was previously found for TAT-14. MALDI-TOF analysis also confirmed synthesis, the mass (+ve) found was 3170.0 and the expected mass was 3171.7. Therefore, the peptide-bound resin was taken forward.

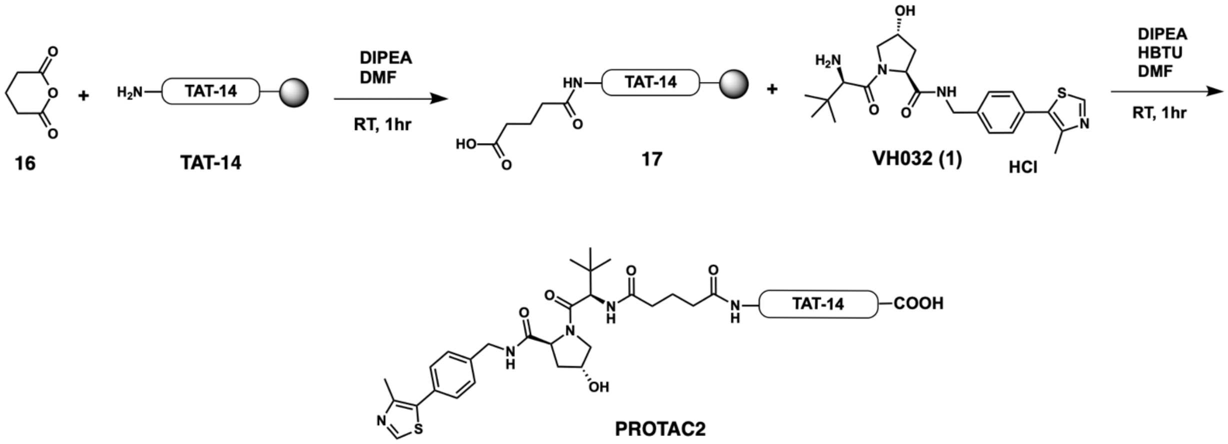

Scheme 2.18. Overview of PROTAC2 synthesis

The first step involved formation of an amide bond by acylation between the TAT-14 amine and glutaric anhydride **16 (Scheme 2.19)**. This would yield the TAT-14/alkyl linker **17** with a carboxylic acid to allow VH032 addition. Cyclic anhydrides are highly reactive due to presence of two adjacent electrophilic carbonyl groups and do not require coupling reagents. The reaction mechanism proceeds initially by nucleophilic attack of the TAT-14 amine with either carbonyl carbon of **16** to form a tetrahedral intermediate. A carboxylate group leaves as the ring is cleaved, which generates the amide bond and a carboxylic acid group.

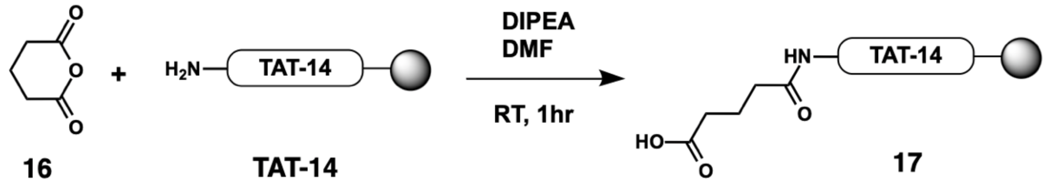

Scheme 2.19. Ring-opening of glutaric anhydride (16) to acylate the amine of TAT-14 to yield the TAT-14/glutaric acid conjugate (17)

TAT-14 was shaken with **16** and DIPEA in DMF for 1 hr. Both DIPEA and 14 were in excess (5 equiv.) and the reaction was repeated once to promote complete synthesis (**Scheme 2.19**). A small sample of resin was cleaved and deprotected to allow for characterisation. HPLC analysis found one minor peak (tR = 15.2 min) which was suspected to be **17**. After semi-prep HPLC purification, MALDI-TOF analysis of the fractions suggested compound **17** was synthesised as expected mass was 3285.7 and the found mass was 3284.1. Therefore, the rein-bound **17** was taken forward.

The second reaction involved an amide coupling between the linker carboxylic acid of **17** with the free amine of VH032 **1 (Scheme 2.20)**. Initially, **17** was shaken with DIPEA in DMF to deprotonate the acid, which was followed by HATU to generate the active ester.

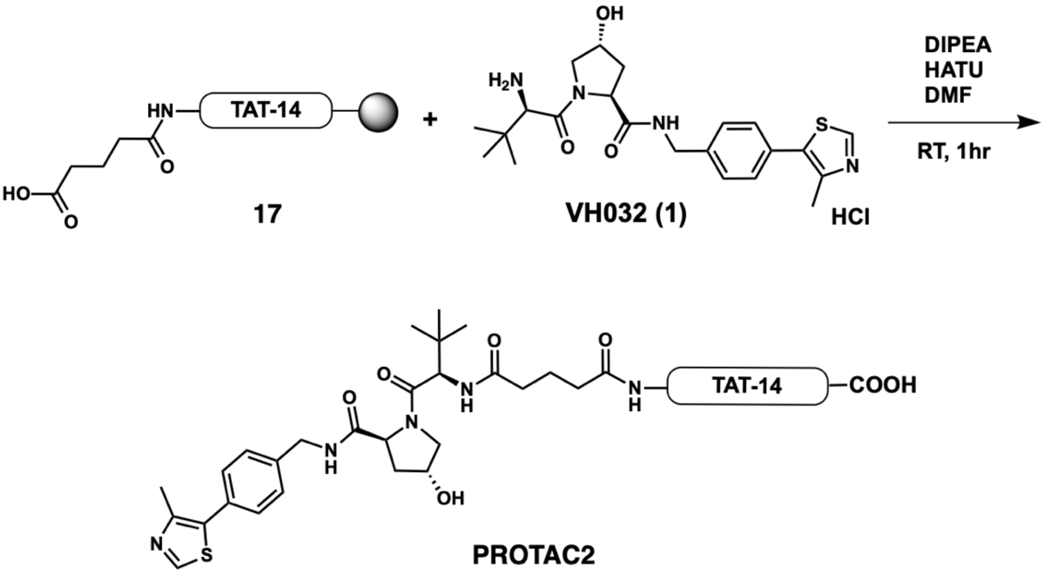

Scheme 2.20. Amide coupling between the acid (17) and amine VH032 to yield PROTAC2

VH032 **1** was added and the reaction mixture was shaken for 45 min. Both DIPEA and HATU were in excess (5 equiv.) with VH032 only in small excess (1.5 equiv.) to conserve compound. The coupling was repeated once and a small sample was cleaved and deprotected then characterised. HPLC analysis found multiple peaks between 13 to 20 min, with no major peak formed, circled in **Figure 2.12**. Therefore, it was purified by semi-prep HPLC which was challenging due to the number of compounds present, which was ultimately unsuccessful. Reverse-phase chromatography was also performed for complete purification, but PROTAC2 was not isolated in any fraction, suggesting the synthesis was not successful.

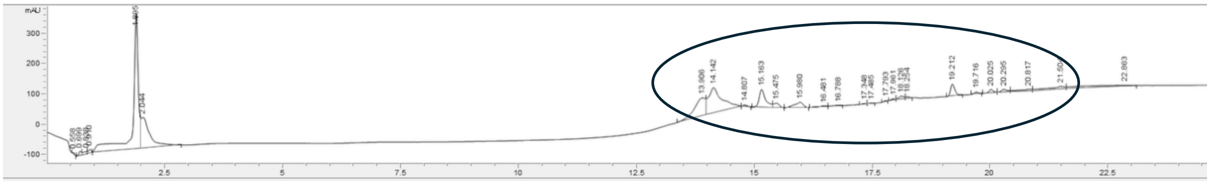

Figure 2.12. Crude PROTAC2 HPLC trace.

PROTAC2 Optimised Synthesis

The procedure was attempted again with modification. TAT-14 was synthesised on the Liberty Blue peptide synthesiser using the same resin, which was scaled up to 0.164 mg. The Liberty synthesiser can improve reaction efficiency due to microwave assistance which can increase yield compared to the Syro I peptide synthesiser. A small sample was cleaved, deprotected and characterised. HPLC analysis found a major peak (rT = 9.4) which was suspected to be TAT-14 (**Figure 2.13**). The trace was clean with minimal impurities which suggested the synthesis was efficient. MALDI TOF analysis also confirmed synthesis, the expected mass 3171.7 and the found mass 3172.7.

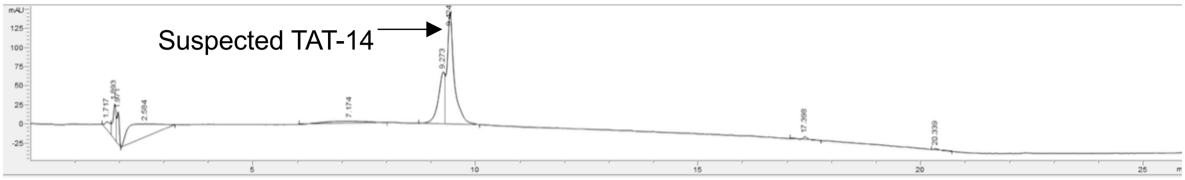

Figure 2.13. HPLC trace of crude TAT-14 test

The same reaction conditions were used previously to synthesise **17,** since it was previously successful (**Scheme 2.21**). A small sample was cleaved and characterised. HPLC analysis found one major peak which was suspected to be 15 (Rt = 9.6), although it was similar to TAT-14 (rT = 9.4) (**Figure 2.14**). Since **17** is more polar than TAT-14, due to linker addition a slightly shorter retention time was expected. MALDI-TOF confirmed synthesis of **17**, as the mass found was 3285.9 and the expected mass was 3285.7, therefore it was taken forward.

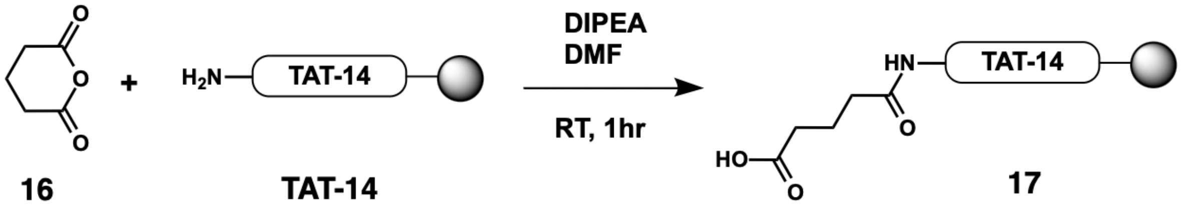

Scheme 2.21. Ring-opening of glutaric anhydride to acylate the amine of TAT-14 to yield the TAT-14/glutaric acid conjugate (repeated conditions)

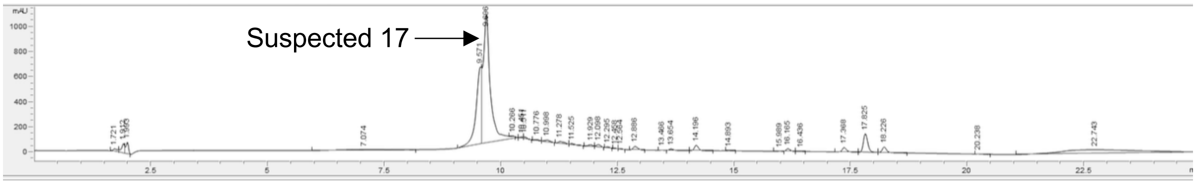

Figure 2.14. HPLC trace of test TAT14/glutaric acid linker conjugate (15)

The subsequent amide coupling reaction was modified by replacing the coupling reagent from HATU to HBTU to synthesise PROTAC2 (**Scheme 2.22**). The TAT-14/glutaric acid conjugate **17** was reacted with DIPEA, to deprotonate the acid, followed by HBTU to generate the active ester. VH032 **1** was added and the reaction mixture was shaken for 45 min, which was repeated once. The peptide was cleaved, fully deprotected and lyophilised to form a white powder, with a crude mass 0.593 g. The crude peptide was analysed by HPLC, finding two major peaks (tR of 9.7 and 10.3) (**Figure 2.15**).

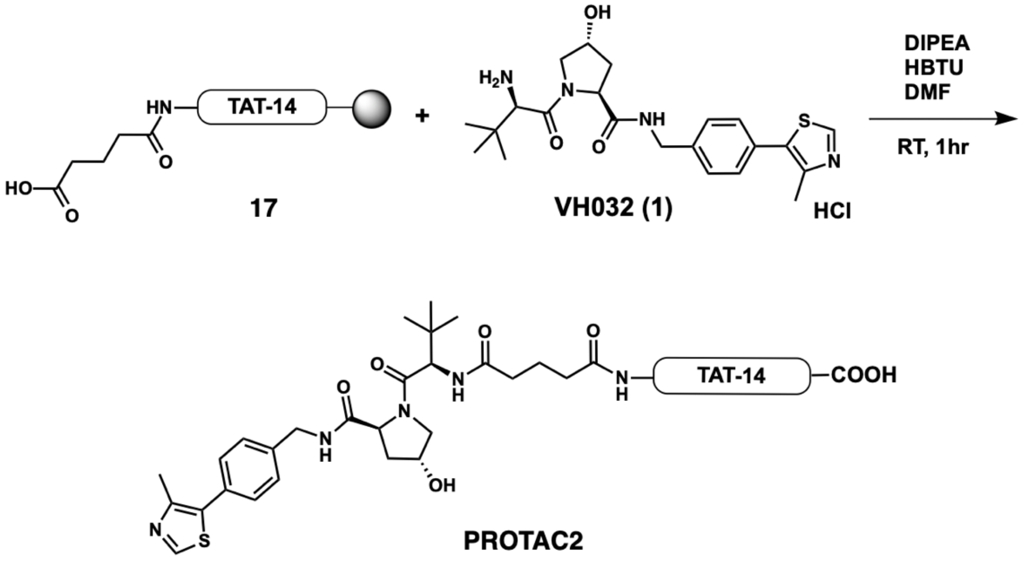

Scheme 2.22. Optimised HBTU amide coupling between the acid (15) and amine VH032 (1).

Therefore, it was purified by reverse-phase chromatography which found PROTAC2 formed in the later peak (tR = 10.3) (**Figure 2.16**). Although purified, the broadening of the peak suggested some impurities remained. The mass was confirmed by MALDI-TOF, expected mass 3697.9 and the found mass was 3698.0. The isolated fractions were concentrated and PROTAC2 was lyophilised to afford 68 mg (18.6% yield) of a white solid.

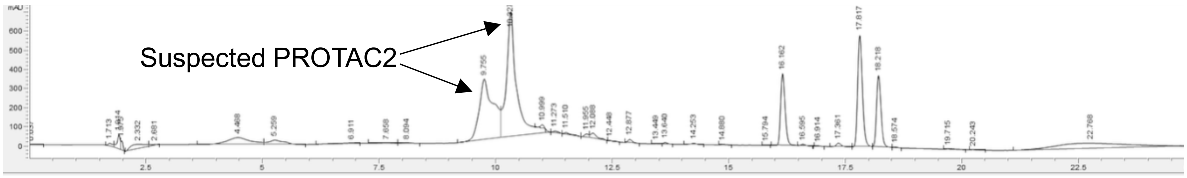

Figure 2.15. HPLC trace of crude PROTAC 2

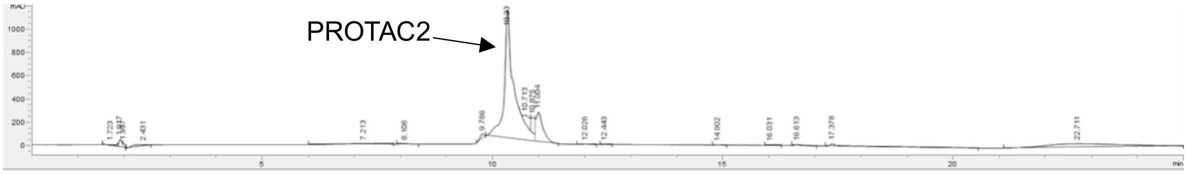

Figure 2.16. HPLC trace of purified PROTAC2

2.9 PROTAC2 *In Vitro* Assays

2.9.1 RT-qPCR

To assess the transcriptional activation of NRF2-regulated ARE genes, HO-1 and NQO1 mRNA expression was quantified by RT-qPCR following 6 h treatment with PROTAC2 (75 or 100 μM), 75 μM TAT-14 or DMSO as the vehicle control. Following treatment, RNA was extracted, cDNA synthesised, and RT-qPCR was performed as previously described. Treatment with 75 μM PROTAC2 significantly increased HO-1 mRNA expression by 80-fold relative to DMSO, while a significant 180-fold induction was found at 100 μM (**Figure 2.17A)**. In contrast, 75 μM TAT-14 elicited only a modest 3.5-fold increase. At the same concentration, PROTAC2 enhanced HO-1 mRNA induction by 23-fold compared with TAT-14 alone. Furthermore, when compared with the 7-fold induction of HO-1 mRNA by 30 μM DMF found initially, PROTAC2 elicited a far greater induction. While both treatments were at different concentrations, the difference of HO-1 induction is notable. PROTAC2 also significantly induced NQO1 mRNA, though of a lower magnitude than HO-1 (**Figure 2.17B)**. Inductions of 2-fold and 2.8-fold were found at 75 μM and 100 μM respectively for PROTAC2, compared with 1.2-fold for TAT-14 treatment. When compared at the same dose, PROTAC2 treatment resulted in an additional 0.8-fold increase over TAT-14. The difference in inducibility of HO-1 and NQO1 mRNA was expected, as HO-1 is known to be more transcriptionally responsive due to its sensitivity to diverse stress signals [257]. In THP1 cells, NRF2 activation has previously shown HO-1 is markedly more inducible than NQO1 [258] [242].

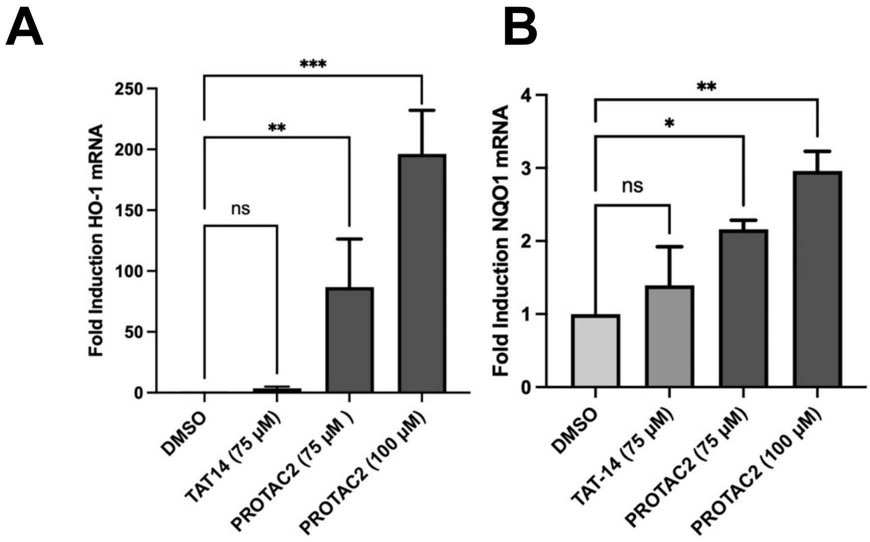

Figure 2.17. (A) Induction of (A) HO-1 mRNA or (B) NQO1 mRNA in THP-1 cells ($10x10^6$) seeded in a 12-well plate in complete media following 6 h treatment with TAT-14, PROTAC2 or DMSO (the vehicle control). Upon stimulation, total RNA was extracted and reverse transcribed into cDNA. HO-1 expression was measured by RT-qPCR with SYBR Green detection, normalised to GAPDH and relative expression calculated using the ΔΔCt method. **One-way ANOVA was performed followed by a post-hoc Dunnett's test to compare each treatment to the DMSO control.** ***Mean ± SEM, n=3, ***$p < 0.001$, **$p < 0.01$, *$p < 0.1$.***

RT-qPCR analysis supports the hypothesis that PROTAC2 activates the NRF2/ARE pathway through event-driven degradation of Keap1. By inducing VHL-mediated ubiquitination and degradation of Keap1, PROTAC2 would be expected to stabilise NRF2 and upregulate ARE gene expression more effectively than the occupancy-driven disruption of the Keap1-NRF2 interaction by TAT-14. Comparison with the activity of previously reported Keap1 degrading PROTACs further supports the proposed mechanism of degradation. SD2267 induced significant increase in HO-1 and NQO1 mRNA in AML-12 cells [232], while KPP1 and PROTAC14 upregulated HO-1 and NQO1 protein levels in various cell lines [230] [233]. This suggests PROTAC2 degraded Keap1, which allowed NRF2 to induce HO-1 and NQO1. To confirm NRF2 activation, RT-qPCR could be used to assess induction of other NRF2-regulated ARE genes such as ferritin, GCLM and GCLC. Moreover, assessment of inflammatory cytokine expression such as IL-1β and TNF-α would provide relevance with treating inflammatory disease.

2.9.2 MTS Assay

The toxicity of PROTAC2 was then evaluated by an MTS cell viability assay. THP-1 cells were prepared following the procedure previously described and treated with 75 μM or 100 μM PROTAC2, alongside DMSO as the (vehicle control). The cells were incubated for 24 h before addition of 10 μL MTS solution, with subsequent incubation for 3 h before absorbance at 495 nm was detected with a microplate reader. Cell viability was normalised against DMSO treated cells (**Figure 2.18**). PROTAC2 significantly decreased cell viability by 20% at 75 μM and 25% at 100 μM, compared to the DMSO control, which is notable. The treatments could have induced a stress response which would explain the reduction in cell viability and the activation of NRF2, which would require further investigation to confirm PROTAC2 mediated NRF2 activation. However, the significant induction of both HO-1 and NQO1 mRNA found upon PROTAC2 treatment (Figure 2.17) suggests NRF2 was robustly activated by PROTAC2, rather than solely by oxidative signalling.

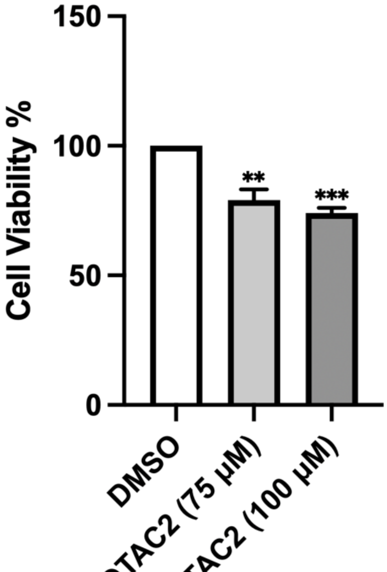

Figure 2.18 MTS cell viability assay was conducted with 1x10^5 THP-1 cells in a 96-well plate in complete media treated with TAT-14 and PROTAC2 in triplicates for 6 h. Upon stimulation, cells were treated with MTS solution for 3 h and incubated. Upon incubation, absorbance was measured at 492 nm using a microplate reader and cell viability was calculated by subtracting background absorbance and treatment conditions were normalised against the DMSO control. One-way ANOVA was performed followed by a post-hoc Dunnett's test to compare each treatment to the DMSO control. ***Mean ± SEM, n=3, **$p < 0.01$, ***$p < 0.001$.***

Conclusion

TAT-14 was successfully synthesised by Fmoc SPPS, purified and validated by HPLC and MALDI-TOF. TAT-14 was synthesised on both a Liberty Blue and Syro I automated peptide synthesiser using a preloaded Wang resin, whereas Steel *et al.* only reported synthesis on a Syro I with a TGA resin. This shows the synthesis is flexible and reproducible across SPPS systems. Western blot analysis found NRF2 protein expression was increased with TAT-14 and DMF treatment, which was consistent with the literature. Also, TAT-14 increased HO-1 mRNA expression by 3-fold which shows a positive induction, albeit markedly lower than what was expected from previous reports. During PROTAC development, VH032 was successfully synthesised based on the protocol by Yan *et al*. The procedure was scaled down and the washing and extractions were sufficient in removing by-products and excess reagents without chromatography purification. An initial attempt to synthesise PROTAC1 using a PEG linker was unsuccessful, as the TAT-14/PEG conjugate could not be confirmed by MALDI-TOF despite appearance of a new HPLC peak. However, replacing the PEG linker with a glutaric anhydride-derived alkyl liner resulted in the successful synthesis and purification of PROTAC2. PROTAC2 significantly increased HO-1 and NQO1 mRNA expression (by 80-fold and 2-fold, respectively) which was a dramatic increase compared to TAT-14 alone (3-fold and 1.3-fold, respectively). Although PROTAC2 demonstrated NRF2/ARE pathway activation, several limitations remain. While the observed induction of HO-1 and NQO1 mRNA suggests pathway activation, the mechanism of action was not confirmed to verify ternary complex formation, Keap1 proteasomal degradation or NRF2 protein upregulation. Therefore, PROTAC2 cannot be confirmed to function as a Keap1 degrader. Future studies should therefore aim to validate the proposed mechanism of action of PROTAC2. Fluorescence polarisation or SPR assays could be used to confirm disruption of the Keap1-NRF2 interaction, while NanoBRET would confirm ternary complex formation [259]. Western blot could be performed to show Keap1 degradation and NRF2 accumulation. Collectively this project demonstrates that cell-penetrating peptide-based NRF2 activators, which disrupt the Keap1-NRF2 interaction, can be reproposed as warheads in PROTAC design. PROTAC2 differs from previously reported NRF2 activating PROTACS as a peptide-small molecule conjugate, comprising the peptide TAT-14 and the small molecule VH032. In contrast, KKP1 [230] is entirely peptide-based, whereas SD2267 [232] and PROTAC14 [233] are small-molecules. Therefore, PROTAC2, as a hybrid peptide-small molecule conjugate, presents a promising novel strategy which combines the cell-penetrating and Keap1-binding abilities of a peptide warhead with the E3 ligase recruiting ability of a small-molecule ligand for targeted NRF2 activation, with potential therapeutic benefits in inflammatory disease.

Experimental

2.10 TAT-14 Synthesis

General

All solvents used were from commercial suppliers including Sigma Aldrich (Dorset, UK), Fluorochem (Derbyshire, UK) and Thermo Fisher (Leicestershire, UK) (unless otherwise stated) and were of analytical or HPLC grade. Analytical HPLC was performed on an Agilent 1260 Infinity system using a linear gradient from 95:5 to 5:95 (water/acetonitrile) with 0.05% TFA additive (unless otherwise stated). The HPLC method was run with a flow rate of 1 mL/min over 25 min. Samples (10 – 20 μL) were injected and detection was measured at 214 nm. Semi-preparative HPLC used a gradient of 95:5 to 5:95 (water:methanol) with 0.05% TFA additive. The method was run with a flow rate of 4 mL/min over 25 min, detecting at 214 nm. MALDI-TOF mass spectrometry was performed using a Shimadzu Axima Performance mass spectrometer (Shimadzu Biotech). The matrix CHCA was prepared in water/acetonitrile (1:1) at 10mg/mL. Matrix was spotted on the plate, then the sample (dissolved in water/acetonitrile, 1:1) and matrix on top (2 μL of each, allowed to air dry between spotting). Spectra (m/z 500 – 5000) was recorded using the Reflectron mode. Reverse-phase column chromatography was performed on an Interchim PuriFlash automated flash purification system using a Biotage KP-C18HS 12g reverse-phase column. The mobile phases were water and acetonitrile, with 0.1% TFA additive. A linear gradient from 100:0 to 0:100 (water:acetonitrile) was used over 40 CV with a flow rate of 12 mL/min. UV absorbance at 214 nm was monitored and fractions were collected, concentrated *in vacuo* and lyophilised.

2.10.1 TAT-14 synthesis

TAT-14 was synthesised using solid-phase Fmoc chemistry with a Multisyntech Syro I automated peptide synthesiser (Biotage). Synthesis was performed with 100 mg preloaded Wang resin (Fmoc-Gln(Trt) Wang resin, 0.61 mmol/g) (Rapp Polymere). Amino acids were prepared in NMP (except for Fmoc-arginine which was dissolved in DMF) (0.5 M). Chain elongation couplings were performed with HBTU/HOBt (0.5 M/0.5 M) in DMF and DIPEA (3 M) in NMP. Deprotection was performed with piperidine (20% v/v in DMF). Upon synthesis, the peptide was cleaved from the resin and deprotected by washing with DMF and MeOH (5 mL x 3) and treated with 3mL cleavage cocktail (95:5:5, TFA/H_2O/TIPS). The reaction mixture was shaken (RT, 3 h), the solution was transferred into an Eppendorf and was concentrated under a flow of N_2. The peptide was precipitated in diethyl ether, pelleted, washed in diethyl ether and concentrated under a flow of N_2 to remove residual solvent. The peptide was characterised by HPLC and MALDI-TOF and purified by reverse-phase chromatography following standard procedure. MS (+ve) expected: 3171.7, found: 3172.10.

2.10.2 VH032 Synthesis

General

The reagents, reactants and solvents used were from various suppliers (Sigma Aldrich, Fluorochem and Thermo Fisher. Distilled water was used for all reactions and work-up. All HNMR spectra was recorded using a Bruker spectrometer at a frequency of 400 MHz using the specified solvent. ^{1}H NMR data was processed using MestReNova. Chemical shifts were recorded in ppm and referenced to the solvent used. Multiplicities were abbreviated as s (singlets), d (doublets), t (triplets), q (quartets) and multiplets (m). Thin-layer chromatography was performed on 0.2 mm silica gel coated aluminium plates and visualised under UV light.

Step 1. Synthesis of tert-Butyl 4-bromobenzylcarbamate (3)

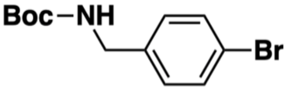

3

To a solution of 4-bromobenzylamine (1.02 g, 5.5 mmol) in 5 mL EtOAc, a solution of $NaHCO_3$ (0.31 g, 3.7 mmol) in 5 mL water was added. To the mixture, a solution of Boc_2O (1.44 g, 6.60 mmol) in 2 mL was added dropwise and a white precipitate formed. The reaction mixture was stirred at RT for 24 h and the solution turned clear. The aqueous phase was extracted with EtOAc. The EtOAc phase was combined, dried ($MgSO_4$) and washed with water (50 mL, 2x) and brine (50 mL, 2x). The EtOAc phase was concentrated *in vacuo* to afford a colourless oil which solidified upon standing (1.46 g). The crude product was used for the next step.

Rf value = 0.67 (80:20, hexane/EtOAc); ^{1}H NMR (400 MHz, DMSO-d_6) δ 7.51 (d, *J* = 8.4 Hz, 2H, CH benzene), 7.42 (t, *J* = 6.3 Hz, 1H, NH), 7.19 (d, *J* = 8.4 Hz, 2H, CH benzene), 4.08 (d, *J* = 6.2 Hz, 2H, NH_2-C$\underline{H_2}$-benzene), 1.39 (s, 9H, Boc CH_3).

Step 2. Synthesis of tert-butyl 4-(4-methylthiazol-5-yl)benzylcarbamate (5)

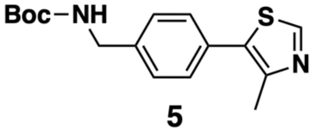

5

A mixture of crude 3 (3.25 g, 11.4 mmol), 4-methylthiazole (2.59 g, 26.1 mmol) and KOAc (2.57 g, 19.8 mmol) in DMAc (25 mL) was degassed with nitrogen for 20 min. $Pd(OAc)_2$ (0.149 g, 0.663 mmol) was added and the mixture was degassed with nitrogen for 10 min. The mixture was stirred at 130 °C for 4 h under a nitrogen atmosphere. To the

mixture 50 mL of each EtOAc and water was added and filtered through a diatomite pad. The pad was rinsed with EtOAc and the organic layer was washed with water (50 mL, x2) and brine (50 mL, x2). The EtOAc phase was concentrated *in vacuo* and azeotroped with CH_2Cl_2 (10 mL) and concentrated again. The crude material was used directly in the next step.
Rf value = 0.60 (80:20, hexane/EtOAc); ^{1}H NMR (400 MHz, DMSO-d_6) δ 8.98 (s, 1H, thiazole CH), 7.44 (d, *J* = 8.1 Hz, 2H, CH benzene), 7.33 (d, *J* = 8.2 Hz, 2H, CH benzene), 4.16 (d, *J* = 6.2 Hz, 2H, NH_2-C$\underline{H_2}$-benzene), 2.45 (s, 3H, thiazole methyl CH_3), 1.40 (s, 9H, Boc CH_3).

Step 3. Synthesis of (4-(4-Methylthiazol-5-yl)phenyl)methanamine Hydrochloride (6)

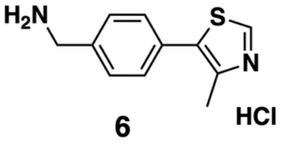

6

To the residue from the previous step, CH_2Cl_2 (25 mL) and HCl (10 mL, 4 M in dioxane) was added. A yellow solid precipitated out immediately during addition. The reaction mixture was stirred at RT for 24 h. The mixture was filtered, dissolved in methanol and dried *in vacuo* to afford a dark yellow solid (2.81 g). The crude product was directly used in the next step.
Rf value = 0.47 (90:10, CH_2Cl_2/MeOH); ^{1}H NMR (400 MHz, DMSO-d_6) δ 9.06 (s, 1H, thiazole CH), 8.46 (s, 3H, NH3+), 7.60 (d, *J* = 8.2 Hz, 2H, benzene CH), 7.55 (d, *J* = 8.0 Hz, 2H, benzene CH), 4.07 (q, *J* = 5.9 Hz, 2H, $\underline{CH_2}$-NH_3^+), 2.47 (s, 3H, thiazole methyl CH_3).

Step 4. Synthesis of (2*S*,4*R*)-*tert*-Butyl 4-Hydroxy-2-((4-(4-methylthiazol-5-yl)benzyl)carbamoyl)pyrrolidine-1-carboxylate (8)

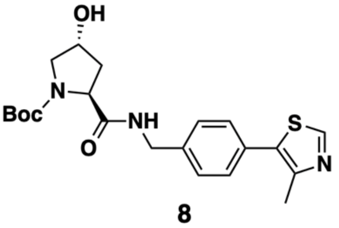

8

Compound **7** (0.566 g, 2.44 mmol), HATU (1.024 g, 2.69 mmol) and DIPEA (1.3 mL, 7.34 mmol) were added to DMF (2 mL) cooled to 0 °C and stirred for 10 min. Crude compound **6** (0.500 g, 2.45 mmol) was added and the reaction mixture was stirred for 2.5 h. The reaction mixture was washed with $NaHCO_3$ (50 mL) and extracted with EtOAc (2x 25 mL). The EtOAc phase was washed with $NaHCO_3$ (50 mL) and brine (50 mL, x2), then dried with sodium sulphate and concentrated *in vacuo* to afford a yellow solid (1.094 g) which was directly used for the next step. Rf value = 0.57 (90:10, CH_2Cl_2/MeOH).

Step 5. Synthesis of (2*S*,4*R*)-4-Hydroxy-*N*-(4-(4-methylthiazol-5-yl)benzyl)pyrrolidine-2-carboxamide Hydrochloride

Crude compound **8** (1.084 g, 2.60 mmol) was dissolved in dioxane (0.80 mL) and EtOAc (3.20 mL). HCl (4.40 mL, 4M in dioxane) was added and a yellow solid precipitated out. The mixture was stirred at RT for 24 h. The yellow solid was filtered, washed with EtOAc (50 mL, x2) and dried *in vacuo* to afford a yellow solid (1.021 g) which was directly used for the next step.

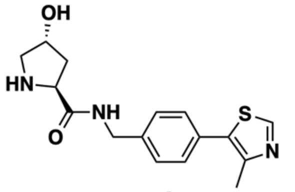

9

Rf value = 0.39 (90:10, CH_2Cl_2/MeOH); ^1H NMR (400 MHz, Methanol-d_4) δ 9.83 (s, 1H, thiazole CH), 9.02 (s, 1H, NH), 7.59 (d, *J* = 8.4 Hz, 2H, benzene CH), 7.53 (d, *J* = 8.4 Hz, 2H, benzene CH), 4.63 (t, *J* = 3.5 Hz, 1H, Hyp), 4.62 – 4.49 (m, 2H, NH-$\underline{CH_2}$-benzene), 3.45 (m, 1H, Hyp CH), 2.61 (s, 3H, thiazole CH_3), 2.51 (m, 1H, Hyp CH), 2.11 (m, 1H, Hyp CH).

Step 6. Synthesis of *tert*-Butyl ((*S*)-1-((2*S*,4*R*)-4-Hydroxy-2-((4-(4-methylthiazol-5-yl)benzyl)carbamoyl)pyrrolidin-1-yl)-3,3-dimethyl-1-oxobutan-2-yl)carbamate

Compound **10** (0.158 g, 0.680 mmol) was dissolved in CH_2Cl_2 (3 mL) and cooled to 0 °C. DIPEA (0.230 g, 1.70 mmol) and HATU (0.302 g, 0.794 mmol) was added and stirred for a further 10 min. Crude compound **9** (0.180 g, 0.567 mmol) was added and the reaction mixture was stirred at RT for 18 h under a nitrogen environment. The reaction mixture was washed with 10% citric acid (50 mL, x2), saturated $NaHCO_3$ (50 mL, x2), water (50 mL, x2) and brine (50 mL, x2). Then the organic phase was concentrated *in vacuo* to afford a yellow oil (0.272 g) which was directly used for the next step. Rf value = 0.37 (90:10, CH_2Cl_2/MeOH)

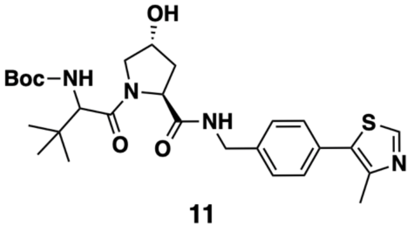

11

Step 7. Synthesis of (2*S*,4*R*)-1-((*S*)-2-Amino-3,3-dimethylbutanoyl)-4-hydroxy-*N*-(4-(4-methylthiazol-5-yl)benzyl)pyrrolidine-2-carboxamide Hydrochloride (1, VH032 HCl)

Crude compound 11 (0.249 g, 0.470 mmol) was dissolved in CH_2Cl_2 (2 mL) and HCl (0.7 mL, 4M in dioxane) was added. The mixture was stirred at RT for 18 h and a yellow solid precipitated. The solid was filtered, washed with CH_2Cl_2 (50 mL, 2x) and dissolved in MeOH. The mixture was concentrated *in vacuo* to afford a yellow solid (0.223 g).

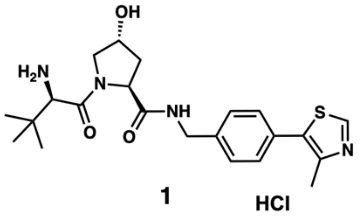

1

Rf value = 0.33 (90:10, CH_2Cl_2/MeOH); ^1H NMR (400 MHz, Methanol-d_4) δ 8.78 (s, 1H, thiazole CH), 7.36 (d, *J* = 8.3 Hz, 2H, benzene CH), 7.30 (d, *J* = 8.2 Hz, 2H, benzene CH), 4.63 – 4.54 (m, 1H, Hyp), 4.49 – 4.39 (m, 2H, NH-CH$_2$-benzene), 4.26 (d, *J* = 15.5 Hz, 1H), 3.99 (s, 1H, Hyp), 3.79 (d, *J* = 11.2 Hz, 1H, Hyp), 3.66 – 3.61 (m, 1H, Hyp), 2.37 (s, 3H, thiazole methyl CH$_3$), 2.26 – 2.17 (m, 1H, Hyp), 2.03 – 1.94 (m, 1H, Hyp), 1.03 (s, 9H, leucine tert-butyl 3x CH$_3$).

2.10.3 PROTAC Synthesis

PROTAC1 Development

TAT-14 was synthesised following the standard procedure using a Multisyntech Syro I automated peptide synthesiser. The resin used was Fmoc-Gln(Trt) Wang resin (100 mg, loading capacity 0.61 mmol/g) (Rapp Polymere). The standard coupling and deprotection procedure was followed. Upon peptide synthesis, the resin was washed with DMF (2x 5 mL), CH_2Cl_2 (3x 5 mL) and MeOH (3x 5 mL) and dried by suction. The resin-bound TAT-14 was used directly for subsequent PROTAC synthesis. A small resin sample was cleaved following the standard procedure to allow for MALDI-TOF and HPLC characterisation.
TAT-14 MS (MALDI +ve) calculated for 3171.7, found: 3170.3.

Step 1 – TAT-14 diglycolic acid linker (PEG) conjugation (13)

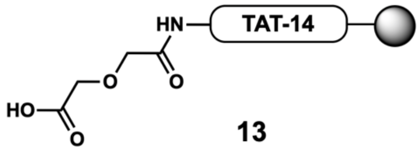

13

The TAT-14-bound resin was swelled in DMF (5 mL) for 10 min. To a solution of diglycolic acid (0.082 g, 0.61 mmol) in DMF (1 mL), DIPEA was added (0.079 g/0.106 mL, 0.61 mmol) and the mixture was stirred (RT, 10 min). HATU was subsequently added (0.232 g, 0.61 mmol) and was further stirred (10 min). The resin was drained under suction, and the coupling solution was added. The reaction mixture was shaken (RT, 45 min). The reaction was monitored by the Kaiser test. It was performed by transferring a small sample to an Eppendorf, to which three drops of reagent A (KCN/H2O/pyridine), reagent B (ninhydrin/n-butanol) and reagent C (phenol/*n*-butanol) were added. The eppendorf was heated (110 °C, 5 min) and the colour change was observed. The colour remained dark red/orange which was inconclusive. After shaking the resin was drained, washed (5x DMF 5mL) and drained again. A small sample was cleaved following the standard procedure to allow for HPLC and MALDI-TOF analysis. MS (MALDI +ve) calculated for 3171.7, found: not found.

Step 2 – TAT-14/PEG conjugation with benzylamine (15)

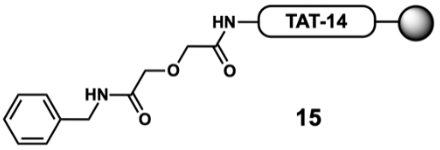

15

The TAT-14/PEG-bound resin was swelled in DMF (5 mL) for 10 min. The resin was drained and a solution of DIPEA (0.079 g/0.106 mL, 0.61 mmol) in DMF (1 mL) was added and shaken (10 min). HATU was added (0.232 g, 0.61 mmol) and shaken (10 min). Benzylamine (0.065 g/0.066 mL, 0.61 mmol) was added and the reaction mixture was shaken (45 min). The resin was drained and the reaction was repeated. After the second coupling reaction the resin was washed with DMF (3x 5 mL) and MeOH (3x 5 mL) and drained under suction. The resin was cleaved following the standard procedure. HPLC and MALDI-TOF was performed following standard procedure. MS (MALDI +ve): calculated: 3376.8, found: not found.

PROTAC2 Development

TAT-14 was synthesised following the standard procedure above. A small sample was cleaved following standard procedure and characterised by HPLC and MALDI-TOF following standard procedure. MS (MALDI +ve): calculated: 3171.7, found: 3170.0.

Step 1 – TAT-14 glutaric anhydride (alkyl linker) conjugation (17)

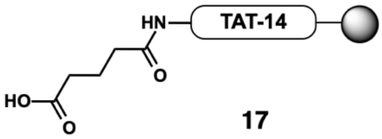

17

Resin-bound TAT-14 was swelled in DMF (5 mL) for 10 min then drained. A solution of glutaric anhydride (0.035 g, 0.305 mmol) in DMF (1 mL) was added. DIPEA (0.039 g/0.053 mL, 0.305 mmol) was subsequently added and the reaction mixture was shaken for 1 h. The resin was drained and the reaction was repeated once. Upon completion, the resin was drained, washed with DMF (3x, 5 mL) and MeOH (3x, 5 mL) then drained. A small sample of resin was cleaved following the standard procedure to allow characterisation by HPLC and MALDI-TOF following standard procedure. MS (MALDI-TOF +ve): calculated: 3285.7, found: 3284.1.

Step 2 – TAT-14/glutaric anhydride conjugation with VH032 (PROTAC2)

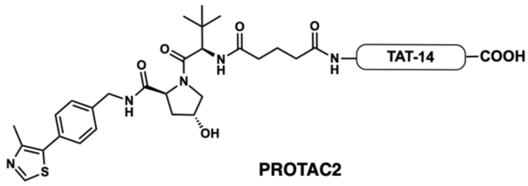

PROTAC2

The TAT-14/glutaric anhydride linker-bound resin was swelled in DMF (5 mL) for 10 min then drained. A solution of DIPEA (0.039 g, 0.305 mmol) in DMF (1 mL) was added and shaken for 10 min. HATU (0.116 g, 0.305

mmol) was subsequently added and shaken for 10 min. Crude VH032 (1) (0.043 g, 0.0915 mmol) was added and the reaction mixture was shaken for 45 min. The resin was then drained and the reaction was repeated once. The resin was drained, washed with DMF (3x 5 mL) and MeOH (3x 5 mL) and drained. The resin was then cleaved following the standard procedure. PROTAC2 was purified by semi-preparative HPLC following the general procedure. The fraction containing pure PROTAC2 was lyophilised to produce a white powder (stored at -80 °C). MS (MALDI-TOF +ve) calculated: 3697.9, found: 3695.1

PROTAC2 Optimised Synthesis

TAT-14 was synthesised on the Liberty Lite automated peptide synthesiser. The resin used was Fmoc-Gln(Trt) Wang resin (164 mg, loading capacity 0.61 mmol/g) (Rapp Polymere). Amino acids were prepared in DMF (0.2M) and chain elongation couplings were performed with DIC (0.5M) with Oxyma (0.5M). Deprotection was performed with piperidine (20% v/v DMF). Upon peptide synthesis, the resin was washed with DMF (2x 5 mL), CH_2Cl_2 (3x 5 mL) and MeOH (3x 5 mL) and dried by suction. The resin-bound TAT-14 was used directly for subsequent PROTAC synthesis. A small resin sample was cleaved following the standard procedure to allow for MALDI-TOF and HPLC characterisation following standard procedure. MS (MALDI-TOF +ve) calculated 3171.7 and the found mass 3172.7.

Step 1 – TAT-14 glutaric anhydride (alkyl linker) conjugation (17)

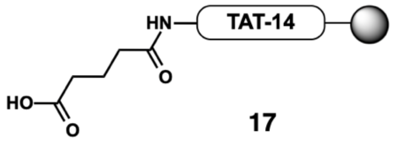

17

Resin-bound TAT-14 was swelled in DMF (5 mL) for 10 min then drained. A solution of glutaric anhydride (0.057 g, 0.444 mmol) in DMF (1 mL) was added. DIPEA (0.065 g/0.088 mL, 0.503 mmol) was subsequently added and the reaction mixture was shaken for 1 h. The resin was drained and the reaction was repeated once. Upon completion, the resin was drained, washed with DMF (3x, 5 mL) and MeOH (3x, 5 mL) then drained. A small sample of resin was cleaved following the standard procedure to allow characterisation by HPLC and MALDI-TOF. MS (MALSI +ve): calculated: 3285.7, found: 3285.9.

Step 2 – TAT-14/glutaric anhydride conjugation with VH032 (PROTAC2)

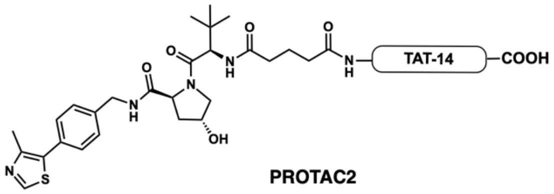

PROTAC2

The TAT-14/glutaric anhydride linker-bound resin was swelled in DMF (5 mL) for 10 min then drained. A solution of DIPEA (0.078 g, 0.604 mmol) in DMF (1 mL) was added and shaken for 10 min. HBTU (0.112 g, 0.295 mmol) was subsequently added and shaken for 10 min. Crude VH032 (1) (0.07 g, 0.15 mmol) was added and the reaction mixture was shaken for 45 min. The resin was then drained and the reaction was repeated once. The resin was drained, washed with DMF (3x 5 mL) and MeOH (3x 5 mL) and drained. The peptide was cleaved from the resin following the standard procedure and lyophilised to afford 553 mg crude product. PROTAC1 was purified by reverse-phase chromatography following the standard procedure. The isolated fractions were concentrated *in vacuo* and the resulting PROTAC2 was lyophilised to afford 68 mg (18.6 % yield). Characterisation was performed by HPLC and MALDI-TOF following standard procedure. MS (MALDI +ve): calculated: 3697.9, found: 3697.0.

2.11 Cell Biology

Cell Culture

Human THP-1 monocytic cells were obtained from the European Collection of Cell Cultures (ECACC, Salisbury, UK). THP1 cells were cultured in RPMI 1640 medium (Sigma Aldrich) supplemented with 10% foetal bovine serum (FBS), 2 mM L-glutamine, 100 IU penicillin and 100 μg/ mL streptomycin (P/S) (Gibco, Leicestershire, UK). Completed media was stored at 4 °C and cells were grown and incubated at 37 °C in a humidified atmosphere containing 5% CO_2.

Stimulation

THP-1 cells were seeded at a density of 5 x 10^5 cells/mL in 2 mL per well (12-well plate) and incubated for 18 h prior to stimulation. Stimulation was performed at a final density of 1 x 10^6 cells/mL with TAT-14 (75 μM or 100 μM), DMF (30 μM) or PROTAC2 (75 μM or 100 μM) and were incubated for 3 h (for protein extracts) or 6 h (for RNA extracts). DMSO (cell culture grade, Sigma Aldrich) was used to dissolve all compounds and an equivalent final concentration of DMSO was included as a vehicle control in all assays.

RNA Extraction and RT-qPCR

After stimulation, cells were pelleted in RNAse-free Eppendorfs and the supernatant discarded. Pellets were resuspended in 1 mL TRI Reagent (Invitrogen), incubated at RT for 15 mins, and stored at -80 °C. RNA extraction was performed by adding 100 μL 1-bromo-3-chloropropane, followed by centrifugation (12,000 x g, 20 min, 4 °C). The aqueous phase was transferred to fresh Eppendorfs and combined with 500 μL 2-propanol. After centrifugation (12,000 x g, 15 min, 4 °C), the supernatant was removed and the RNA pellet was washed with 1 mL 70% ethanol. A final centrifugation (12,000 x g, 10 min, 4 °C) was performed, ethanol was discarded, and residual solvent was evaporated. RNA was dissolved in 20 µL nuclease-free water. Concentration was measured using a Nanodrop spectrophotometer-1000 (Labtech, Uckfield, UK) and purity was assessed by 260/280 and 260/230 ratios. Samples were diluted to 200 ng/μL in nuclease-free water and stored at - 80 °C. For cDNA synthesis, each reaction was prepared with 5 μL of sample RNA (200 ng per reaction) and 5 μL mastermix. The mastermix was prepared from the High-Capacity cDNA Reverse Transcription Kit (Applied Biosystems) per **Table 2.1**.

Table 2.1 cDNA synthesis mastermix reagents and volumes

Reagents	**1X reaction volume (μL)**
Nuclease-free water	1.6
10xRT Buffer	1
Random Hexamers	1
RNase Inhibitor	0.5
Reverse Transcriptase	0.5
dNTPs	0.4

Samples were run on a PTC-100 thermal cycler (Biorad, Hertfordshire, UK) on the RT-PCR program XL. The program cycled from 25 °C for 10 min, to 37 °C for 2 h, then to 85 °C for 5 min. The samples were kept on ice before and after cycling. For RT-qPCR, cDNA was diluted to 5 ng/μL and 5 μL was added to 0.1 mL strip tubes (Qiagen Manchester). Mastermix was prepared for NQO1, HO-1 and GAPDH mRNA and 15 μL was added per tube. Per tube 4 μL nuclease-free water, 10 μL SYBR Green (Thermo Fisher) and 1 µL F + R primers were added per tube. The primers for each gene with the sequence are in **Table 2.2**.

Table 2.2. Gene primers used for RT-qPCR

Gene	Primers	Sequence
HO1 (Invitrogen)	Forward	5’-ATGGCCTCCCTGTACCACACTC-3’
	Reverse	5’-TGTTGCGCTCAATCTCCTCCT-3’
NQO1(Invitrogen)	Forward	5′-TGAAGAGCTTTAGGGTCGCAG-3′
	Reverse	5′-GGATACTGAAAGTTCGCAGGG-3′
GAPDH (Invitrogen)	Forward	5’-AACAGCCTCAAGATCATCAGCA-3
	Reverse	5’-TGCTAAGCAGTTGGTGGTGC-3’

Table 2.3. PCR two-step cycle with melt curve analysis

Cycles	Temperature (°C)	Time
Hold step	95	2 mins
Two-step cycle (repeated 40 x)	95	15 sec
	60	40 sec
Melt curve analysis	60 - 94	

For each gene a non-template control (NTC) was produced, replacing sample cDNA for nuclease-free water. Reaction tubes were loaded onto the Rotor-GeneQ Series 5 Plex PCR Cycler (Qiagen, Manchester, UK) and a two-step cycle was run (see **Table 2.3**). A melt curve analysis was performed, and mRNA expression was normalised against GAPDH expression using the ΔCt method described below.

$$\Delta Ct = Ct \text{ (gene of interest)} - Ct \text{ (housekeeping gene)}$$

$$\Delta\Delta Ct = \ \Delta Ct \text{ (treatment condition)} - \ \Delta Ct \text{ (untreated control)}$$

$$2^{-\Delta\Delta Ct} = \text{Relative gene expression}$$

Protein Extraction and Western Blot

THP-1 cells were seeded overnight in a 12-well plate, then stimulated with 75 μM TAT-14 or 30 μM DMF for 3 h. Cells were removed from the plate, centrifuged in an Eppendorf (5 min, 2500 rpm) and supernatant removed then stored on ice. Cells were washed with 500 μL PBS (cold) and 100 μL diluted 2x Novex tris-glycine SDS lysis buffer solution (Invitrogen) added (SDS buffer/PBS 1:1). The samples were boiled for 5 min, stored on ice, then transferred to the -80 °C freezer overnight.

Sample protein content was quantified with a Nanodrop spectrophotometer. The Nanodrop arm was cleaned with ethanol and 1 μL sample was loaded. Protein content was measured by UV absorbance and quantified in ng/μL. Blank measurements were taken with SDS buffer/PBS (1:1) between each measurement for calibration. The concentration of protein was determined by the Beer-Lambert Law as described below.

$$C = \frac{A}{\varepsilon L}$$

C = concentration (M)
A = UV absorbance (AU)
ε = Extinction coefficient (M^{-1} cm^{-1})
L = Light path (cm)

Buffers were made up per **Table 2.4.** The precast NuPAGE Bis-Tris PAGE gel (Invitrogen) was locked into the chamber of an XCell SureLock Mini Cell (Invitrogen). Running buffer was added to the middle and outer chamber and 500 µL NuPAGE antioxidant solution added to the middle chamber. Each sample was prepared to 18 mL with SDS buffer solution and 2 mL 10X reducing agent. 5 µL PageRuler Prestained Protein Laded alongside each sample was added to the gel and run at 150 V for 5 min then 200 V until the dye front reached the bottom. For transfer, PVDF membrane was soaked in methanol then transfer buffer and agitated for 20 min, 100 RPM on an orbital shaker. The gel was cut and the PVDF membrane placed on top and sandwiched between transfer buffer-soaked filters. Protein transfer was run for 1 h at 33 V in transfer buffer then the membrane was soaked in blocking buffer (30 min at RT, then overnight at 4 °C). The membrane was cut incubated in corresponding primary antibodies for 1.5 h, washed in TBST, blocking solution (3 x 5 min) and TBST (3 x 5 min) (see **Table 2.5**), then incubated in secondary HRP antibodies for 40 min, followed by washing as described above. All incubations were performed at RT on an orbital shaker.

Table 2.4. Western blot buffer solutions

Buffer	Reagents
Running buffer	40 mL 20X MOPS buffer (Invitrogen), 760mL Milli-Q water
10X transfer buffer	24.26 g Tris Base, 112.6 g Glycine, 1 g SDS, 1 L Milli-Q water
Transfer buffer	700 mL Milli-Q water, 200 mL methanol, 100mL 10X transfer buffer
1X TBST	900 mL Milli-Q water, 100mL 10X TBST
blocking buffer	20 g milk powder (Marvel), 400 mL 1X TBST
10X TBST	24.2 Tris Base, 80 g NaCl, 31 mL 5M HCl, 10 mL Tween 20 diluted to 1 L Milli-Q water

Table. 2.5 Western blot antibodies

	Protein	Company	Dilution (in 5 mL blocking buffer)	Details
Primary antibody	NRF2	Cell Signalling	1:750	Rabbit (anti-human)
	Beta-tubulin	Abcam	1:1000	Goat (anti-rabbit)
Secondary antibody	NRF2	Cell Signalling	1:1000	Rabbit (anti-human)
	Beta-tubulin	Abcam	1:1000	Goat (anti-rabbit)

Enhanced chemiluminescence (Novex ECL) (Invitrogen) was used for signal detection. Equal volumes of ECL reagents A and B were mixed (1:1) and applied to the membrane and chemiluminescence captured using the ImageQuant LAS 4000 imager (General Electric, Buckinghamshire, UK).

Densitometry was performed to quantify protein expression as follows. For each band (NRF2 or β-tubulin), ImageJ gave an integrated density (ID) value which is the sum of all pixels inside the rectangular region. To correct for uneven blot background, the ID of an identical sized rectangular region in a blank area was used:

$$I_{\text{corrected}} = ID_{\text{background}} - ID_{\text{band}}$$

Corrected NRF2 intensity for each lane was normalised to the corresponding β-tubulin value:

$$N = \frac{I_{\text{NRF2, corrected}}}{I_{\beta\text{-tubulin, corrected}}}$$

The DMSO control lane was set at 1 and NRF2 levels in DMF and TAT-14 samples were expressed as fold-change relative to the control:

$$\text{Fold change} = \frac{N}{N_{\text{DMSO}}}$$

MTS Cell Viability Assay

THP-1 cells were plated at a density of 1×10^6 cells/mL, with 100 μL added per well (1×10^5 cells/well) in a 96-well plate. Cells were stimulated in triplicate with DMSO (vehicle control) or TAT-14 (75 μM), DMF (30 μM) or PROTAC2 (75 μM) and incubated for 24 h.

Following incubation, 10 μL of CellTiter 96 Aqueous One Solution Cell Proliferation Assay MTS reagent (Promega) was added to each well and was further incubated for 3 h. Absorbance was measured at 492 nm using a POLARstar OPTIMA microplate reader (BMG, Aylesbury, UK). Cell viability was calculated by subtracting background absorbance (media-only wells) and normalising treatment conditions to the DMSO control.

Statistical analysis

Data was analysed using GraphPad Prism and ImageJ for Western blot densitometry. Comparisons between multiple treatment groups were performed using ordinary one-way analysis of variance (ANOVA) under the assumption of a Gaussian distribution. Post hoc multiple comparison was conducted by Dunnett's multiple comparison test (comparing each treatment to the DMSO control). Experiments were conducted $n = 3$ unless otherwise stated and presented with the mean ± SEM and statistical significance was indicated as as $P^* < 0.05$, $P^{**} < 0.01$ or $P^{***} < 0.001$.

Appendix 1 – Chemical Data

A1.1 VH032 Synthesis

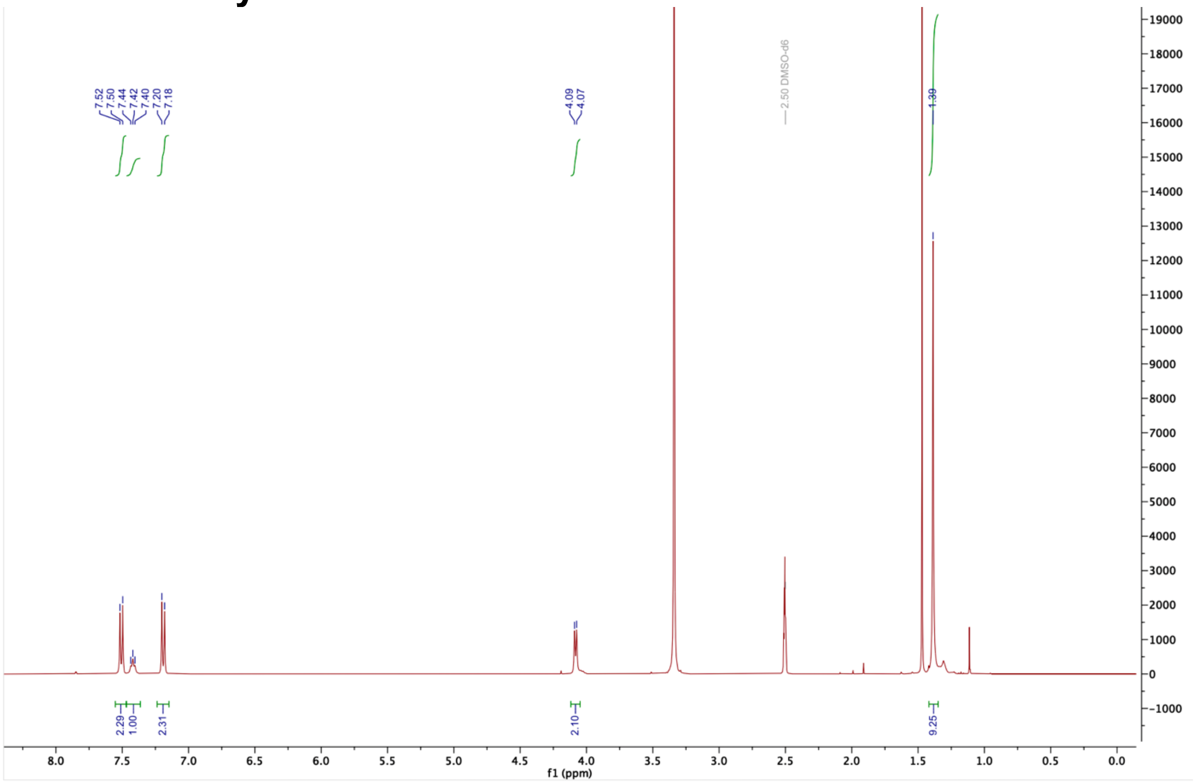

Figure A1.1.1 ^{1}H NMR of compound 3

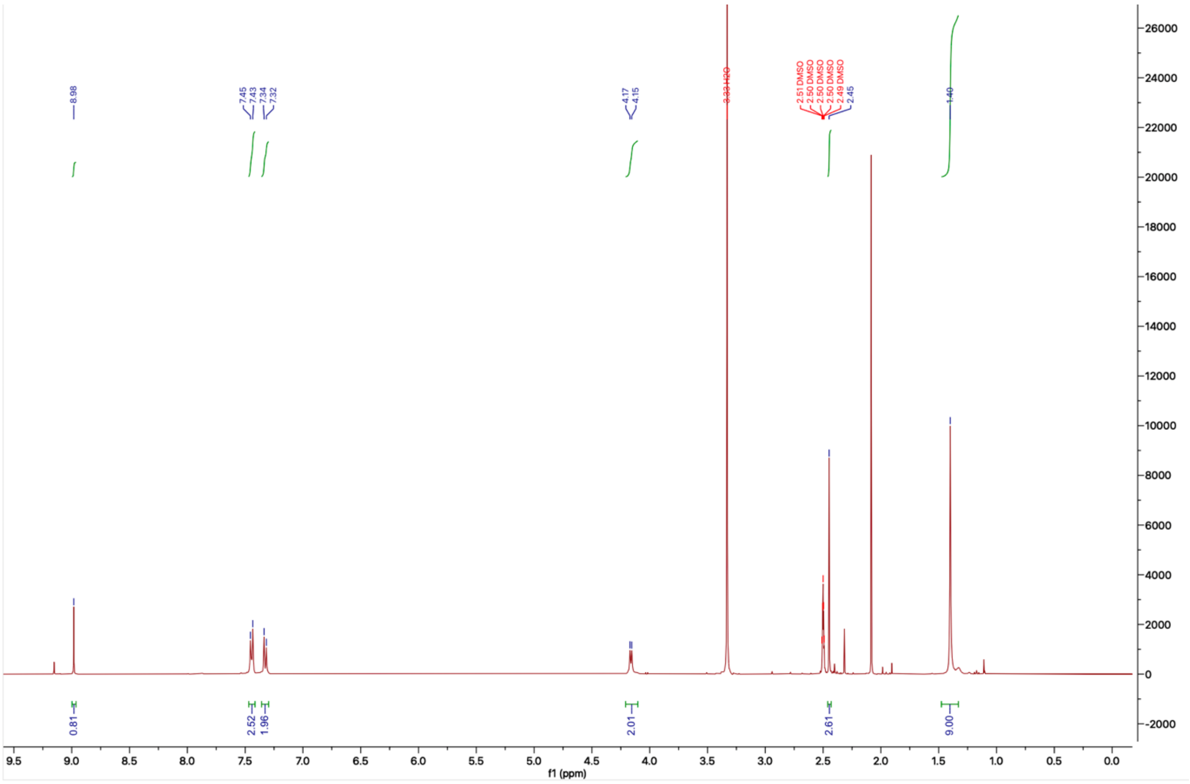

A1.1.2 ^{1}H NMR of compound 5

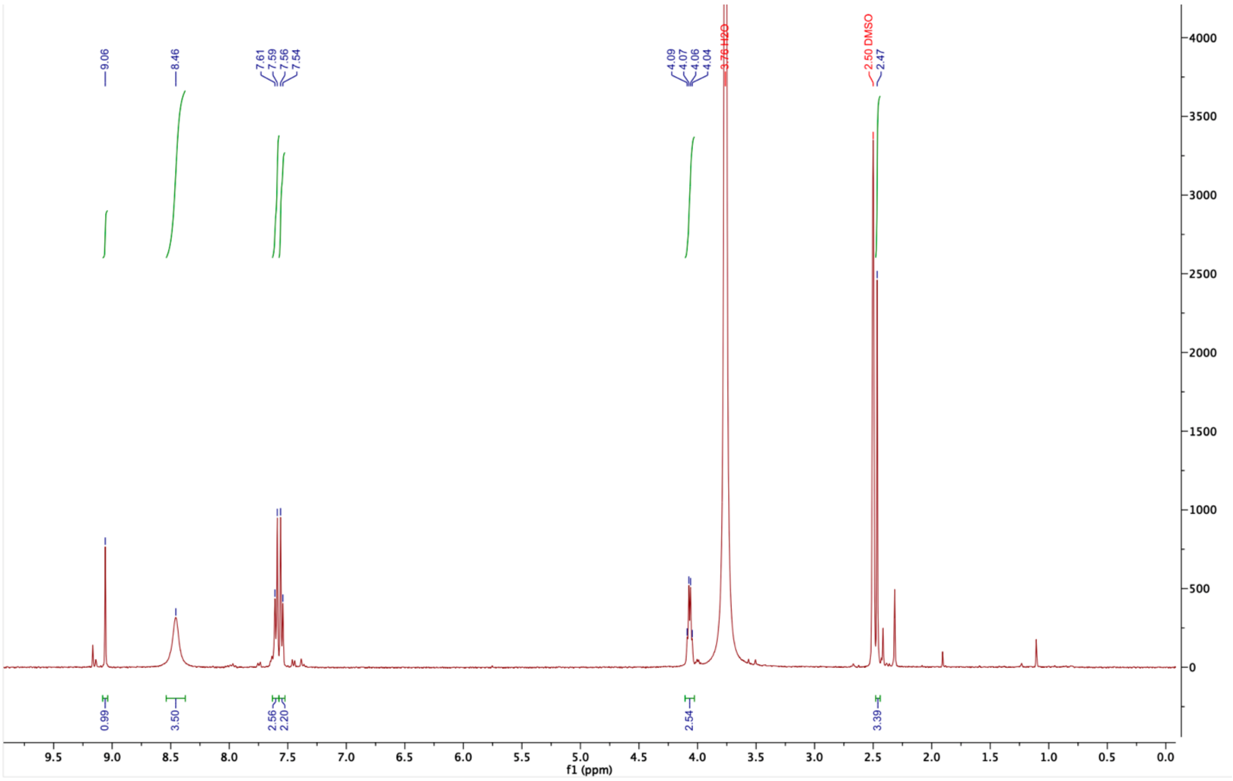

Figure A1.1.3 ^{1}H NMR of compound 6

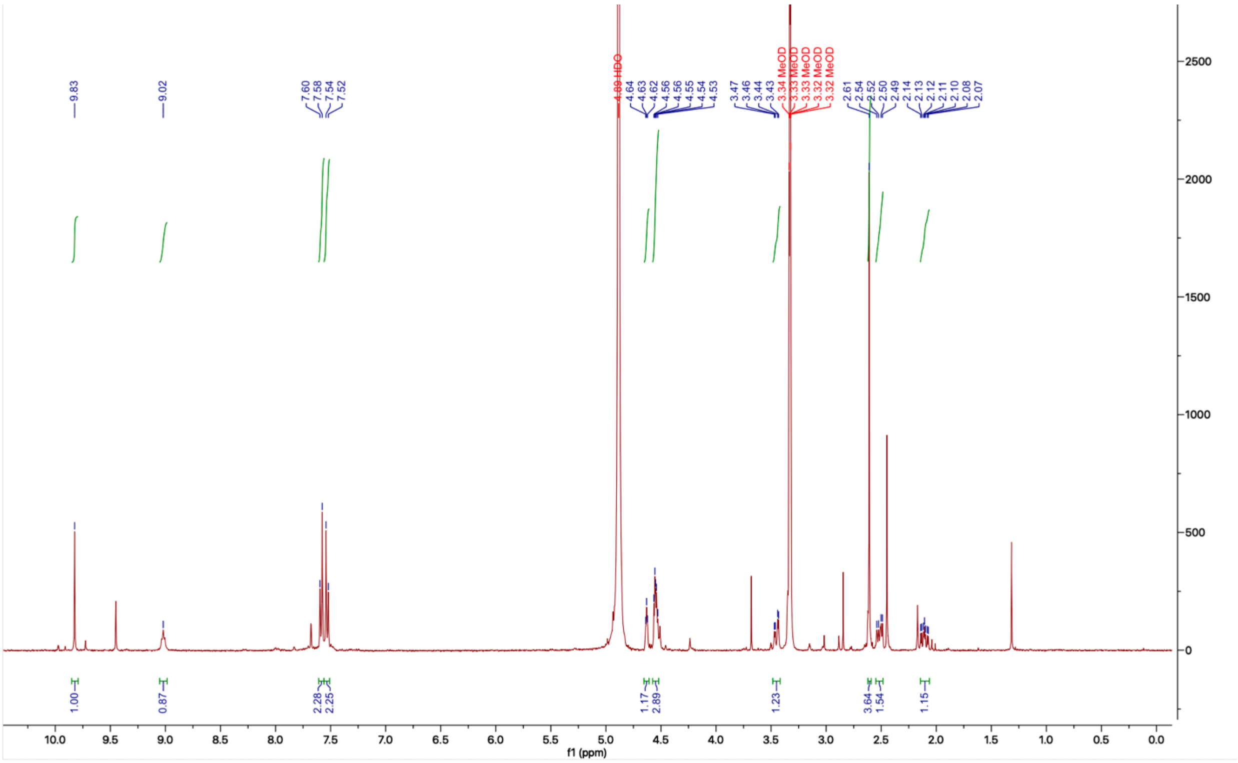

Figure A1.1.4 ^{1}H NMR of compound 9

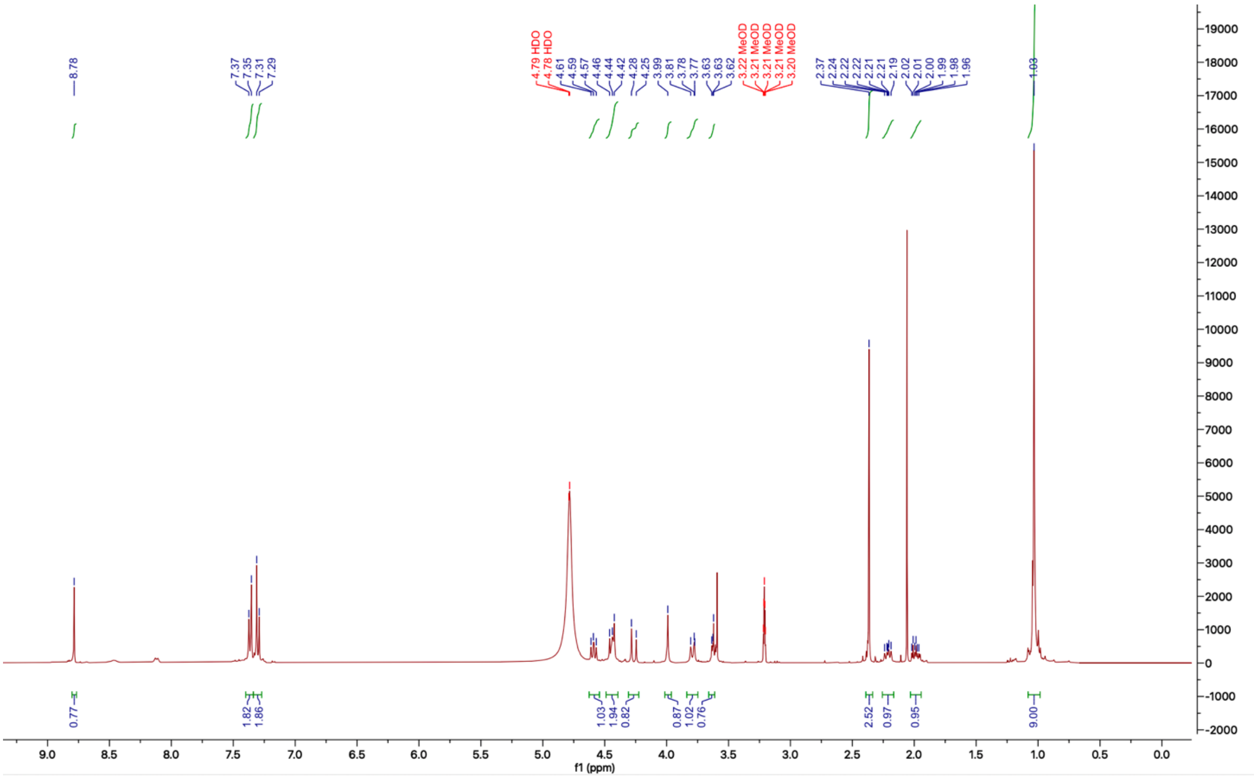

Figure A1.1.5 ^{1}H NMR of compound 1 (VH032)

A1.2 HPLC

Table A1.2.1 HPLC trace of peptides

Compound	HPLC trace
TAT-14 (purified)	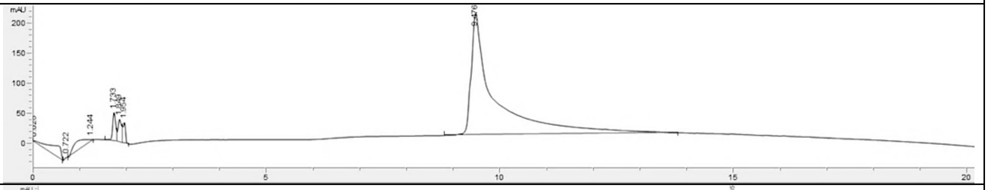
PROTAC1 synthesis: TAT-14 test	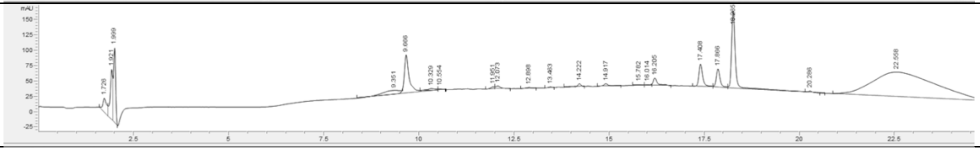
PROTAC1 synthesis: TAT14/diglycolic acid conjugate (13) test	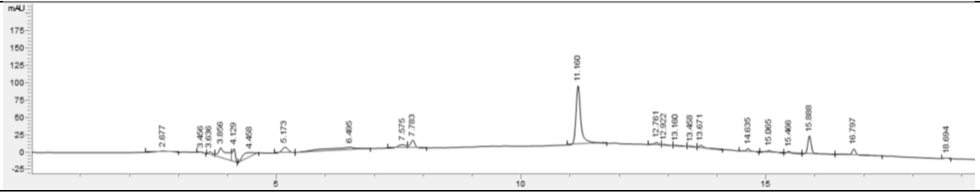

PROTAC1 synthesis: TAT-14/PEG/benzylamine (15) test	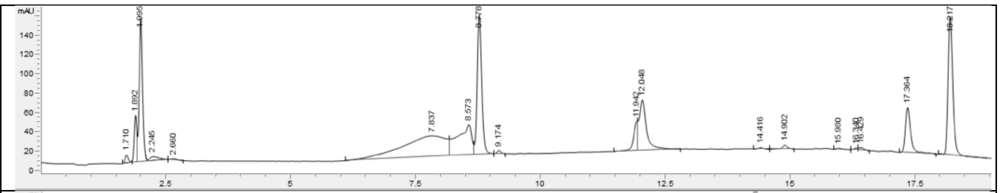
PROTAC 2 synthesis: TAT-14 test	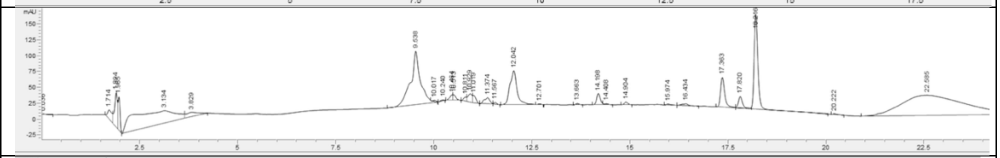
PROTAC2 synthesis: TAT-14/glutaric linker conjugate (17) test	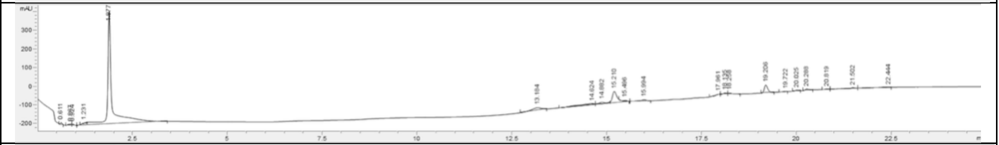
PROTAC2 synthesis: PROTAC 2 full cleavage (crude)	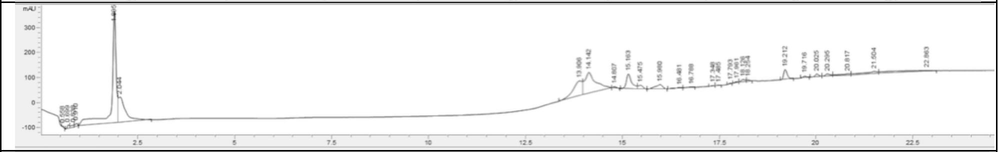
PROTAC2 optimised synthesis: TAT-14 test (crude)	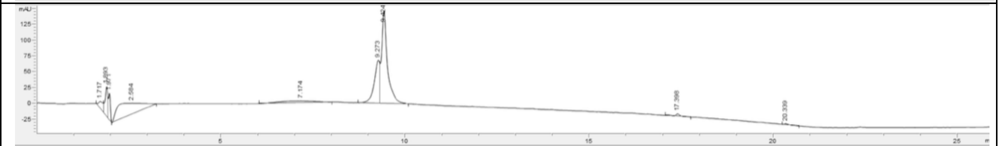
PROTAC2 optimised synthesis: TAT-14/glutaric linker conjugate (17) (crude)	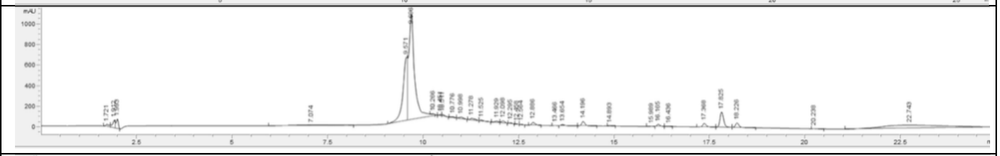
PROTAC2 optimised synthesis: PROTAC2 (crude)	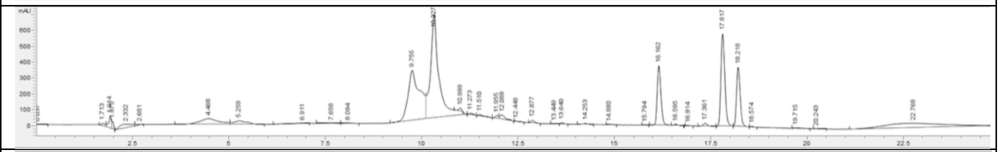
PROTAC2 optimised synthesis: PROTAC2 (purified)	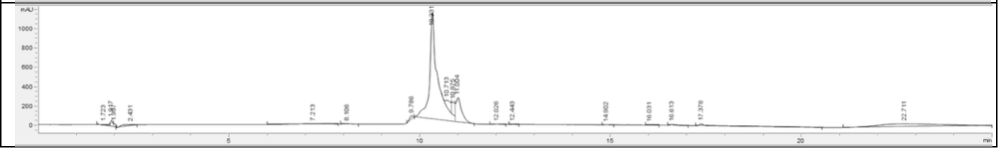

A1.3. MALDI-TOF

Table A1.3.1 MALDI-TOF spectra of peptides

Compound	MALDI-TOF spectra
TAT-14 (purified)	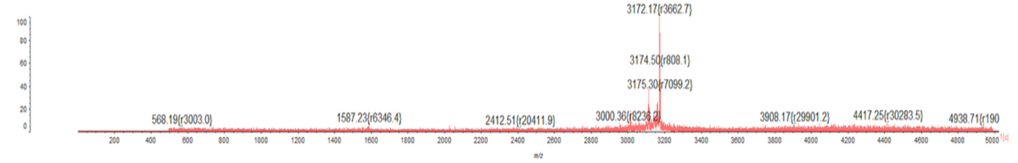
PROTAC1 development: TAT-14 test (crude)	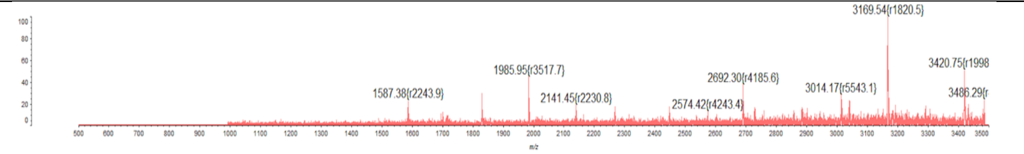

<table>
<tr><td><i>PROTAC2 synthesis: TAT-14 test (crude)</i></td><td>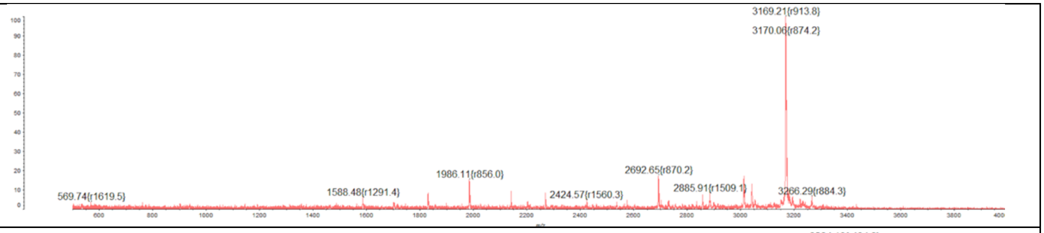 </td></tr>
<tr><td><i>PROTAC2 synthesis: TAT-14/glutaric linker conjugate (17) test (crude)</i></td><td>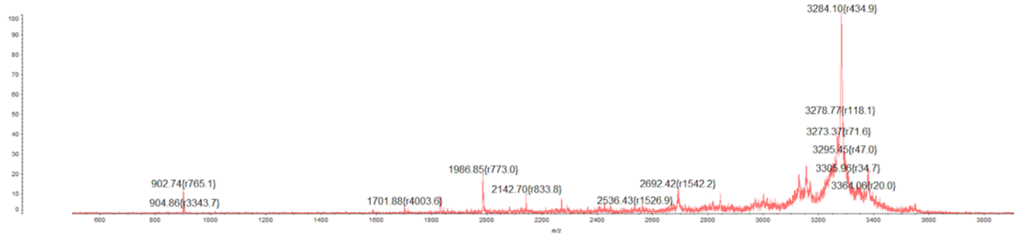 </td></tr>
<tr><td><i>PROTAC2 optimised synthesis: TAT-14 test (crude)</i></td><td>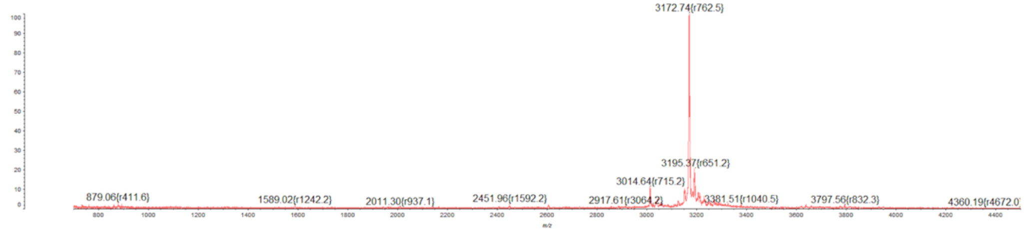 </td></tr>
<tr><td><i>PROTAC2 optimised synthesis: TAT-14/glutaric linker conjugate (17) test (crude)</i></td><td>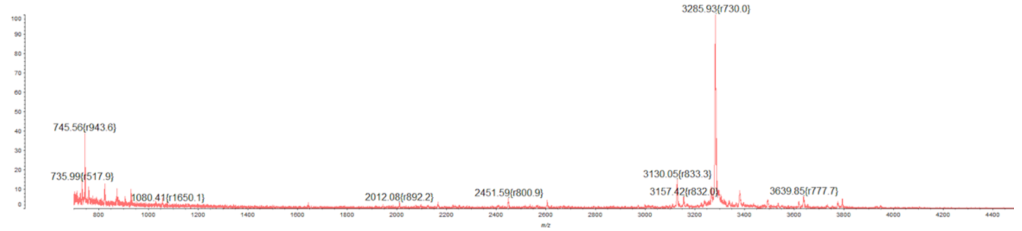 </td></tr>
<tr><td><i>PROTAC2 optimised synthesis: PROTAC2 (purified)</i></td><td>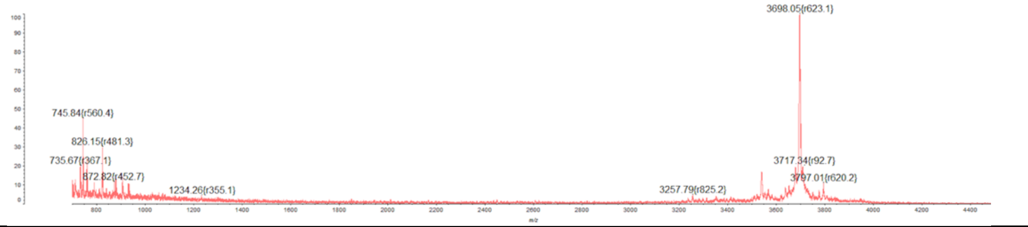 </td></tr>
</table>

Appendix 2 – Biological Data

A2.1 – RT-qPCR

HO-1 mRNA expression measured by RT-qPCR in THP-1 cells following TAT-14 (75 µM and 100 µM), DMF (30 µM) and DMSO (control) treatment. Data plotted for **Figure 2.6.** Melt curve analysis was conducted (see table **A2.1.1**).

Table A2.1.1 Melt curves of genes used with replicates, n=3.

Gene	Dissociation (melt) curve
GAPDH	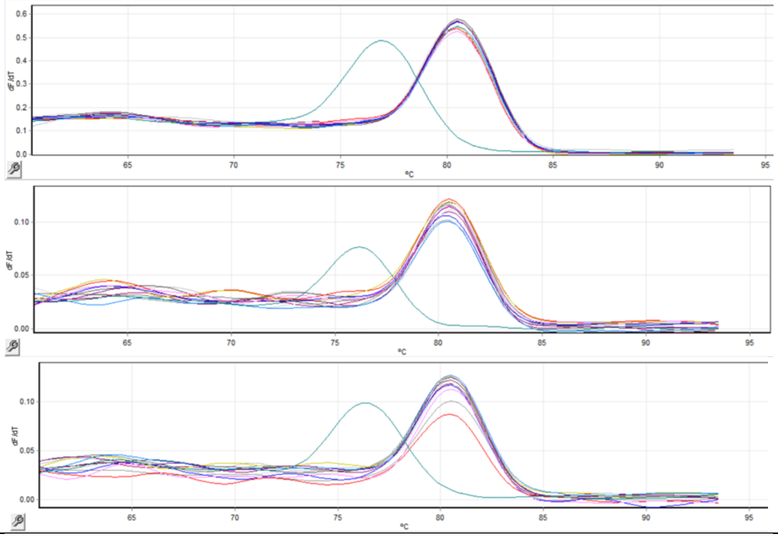
HO-1	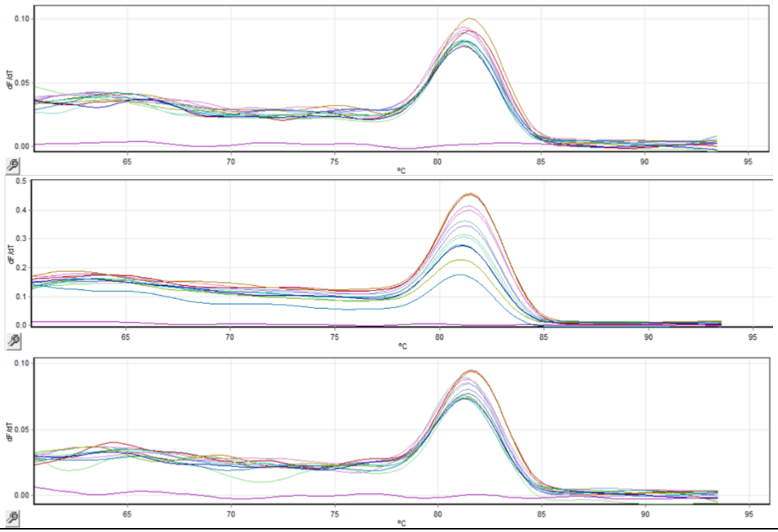

HO-1 and NQO1 mRNA expression measured by RT-qPCR in THP-1 cells following PROTAC2 (75 µM and 100 µM), TAT-14 (75 µM) and DMSO (control) treatment. Data plotted for **Figure 2.17A** and **2.17B**. Melt curve analysis was conducted (see **table A2.2.2**).

Table A2.2.2. Melt curve analysis of genes used with replicates, n=3.

Gene	Dissociation (melt) curve
GAPDH	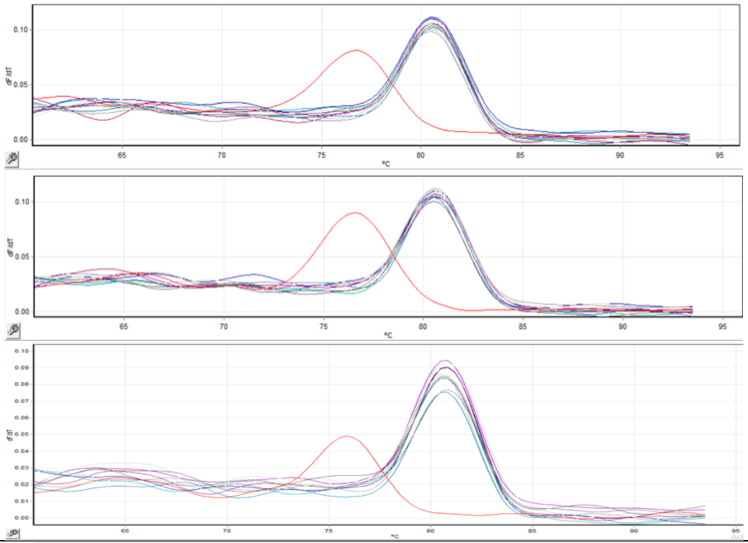
HO-1	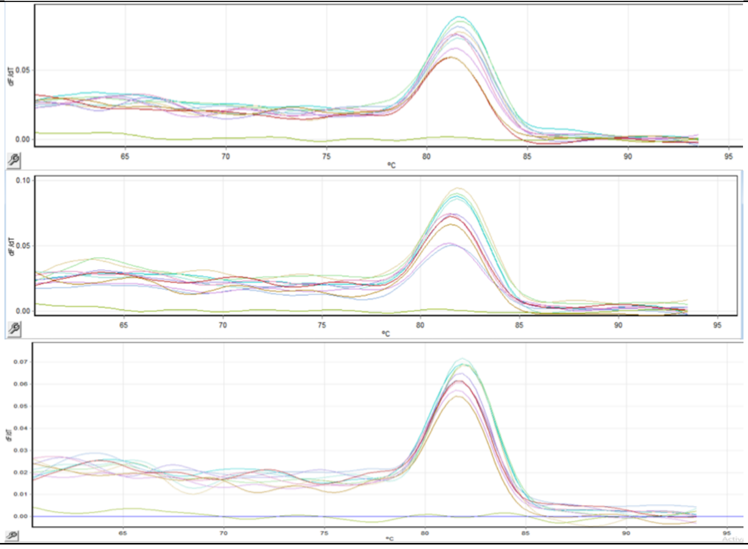

NQO-1	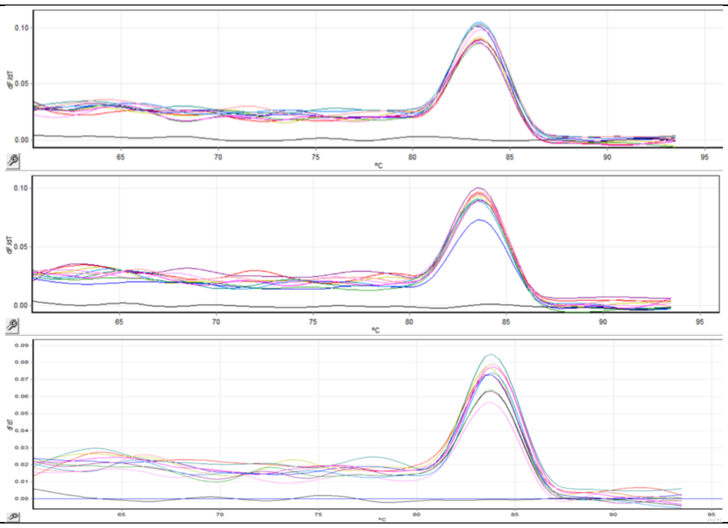0.10 0.05 0.00 dF/dT 65 70 75 80 85 90 95 °C 0.09 0.08 0.07 0.06 0.05 0.04 0.03 0.02 0.01

References

(1) Chen, L.; Deng, H.; Cui, H.; Fang, J.; Zuo, Z.; Deng, J.; Li, Y.; Wang, X.; Zhao, L. Inflammatory Responses and Inflammation-Associated Diseases in Organs. *Oncotarget* **2018**, *9* (6), 7204–7218. https://doi.org/10.18632/oncotarget.23208.

(2) Furman, D.; Campisi, J.; Verdin, E.; Carrera-Bastos, P.; Targ, S.; Franceschi, C.; Ferrucci, L.; Gilroy, D. W.; Fasano, A.; Miller, G. W.; Miller, A. H.; Mantovani, A.; Weyand, C. M.; Barzilai, N.; Goronzy, J. J.; Rando, T. A.; Effros, R. B.; Lucia, A.; Kleinstreuer, N.; Slavich, G. M. Chronic Inflammation in the Etiology of Disease across the Life Span. *Nat Med* **2019**, *25* (12), 1822–1832. https://doi.org/10.1038/s41591-019-0675-0.

(3) Chavda, V. P.; Feehan, J.; Apostolopoulos, V. Inflammation: The Cause of All Diseases. *Cells* **2024**, *13* (22), 1906. https://doi.org/10.3390/cells13221906.

(4) Yan, Z.; Shao, T. Chronic Inflammation in Chronic Kidney Disease. *Nephron* **2024**, *148* (3), 143–151. https://doi.org/10.1159/000534447.

(5) Lewis, J. D.; Parlett, L. E.; Jonsson Funk, M. L.; Brensinger, C.; Pate, V.; Wu, Q.; Dawwas, G. K.; Weiss, A.; Constant, B. D.; McCauley, M.; Haynes, K.; Yang, J. Y.; Schaubel, D. E.; Hurtado-Lorenzo, A.; Kappelman, M. D. Incidence, Prevalence, and Racial and Ethnic Distribution of Inflammatory Bowel Disease in the United States. *Gastroenterology* **2023**, *165* (5), 1197-1205.e2. https://doi.org/10.1053/j.gastro.2023.07.003.

(6) Li, D.; Wu, M. Pattern Recognition Receptors in Health and Diseases. *Sig Transduct Target Ther* **2021**, *6* (1). https://doi.org/10.1038/s41392-021-00687-0.

(7) Soares, C. L. R.; Wilairatana, P.; Silva, L. R.; Moreira, P. S.; Vilar Barbosa, N. M. M.; Da Silva, P. R.; Coutinho, H. D. M.; De Menezes, I. R. A.; Felipe, C. F. B. Biochemical Aspects of the Inflammatory Process: A Narrative Review. *Biomedicine & Pharmacotherapy* **2023**, *168*, 115764. https://doi.org/10.1016/j.biopha.2023.115764.

(8) Liu, T.; Zhang, L.; Joo, D.; Sun, S.-C. NF-κB Signaling in Inflammation. *Sig Transduct Target Ther* **2017**, *2* (1). https://doi.org/10.1038/sigtrans.2017.23.

(9) Immanuel, J.; Yun, S. Vascular Inflammatory Diseases and Endothelial Phenotypes. *Cells* **2023**, *12* (12), 1640. https://doi.org/10.3390/cells12121640.

(10) Cambier, S.; Gouwy, M.; Proost, P. The Chemokines CXCL8 and CXCL12: Molecular and Functional Properties, Role in Disease and Efforts towards Pharmacological Intervention. *Cell Mol Immunol* **2023**, *20* (3), 217–251. https://doi.org/10.1038/s41423-023-00974-6.

(11)Kolaczkowska, E.; Kubes, P. Neutrophil Recruitment and Function in Health and Inflammation. *Nat Rev Immunol* **2013**, *13* (3), 159–175. https://doi.org/10.1038/nri3399.

(12) Zeng, M. Y.; Miralda, I.; Armstrong, C. L.; Uriarte, S. M.; Bagaitkar, J. The Roles of NADPH Oxidase in Modulating Neutrophil Effector Responses. *Molecular Oral Microbiology* **2019**, *34* (2), 27–38. https://doi.org/10.1111/omi.12252.

(13) Tran, N.; Mills, E. L. Redox Regulation of Macrophages. *Redox Biology* **2024**, *72*, 103123. https://doi.org/10.1016/j.redox.2024.103123.

(14) Turner, M. D.; Nedjai, B.; Hurst, T.; Pennington, D. J. Cytokines and Chemokines: At the Crossroads of Cell Signalling and Inflammatory Disease. *Biochimica et Biophysica Acta (BBA) - Molecular Cell Research* **2014**, *1843* (11), 2563–2582. https://doi.org/10.1016/j.bbamcr.2014.05.014.

(15) Kany, S.; Vollrath, J. T.; Relja, B. Cytokines in Inflammatory Disease. *IJMS* **2019**, *20* (23), 6008. https://doi.org/10.3390/ijms20236008.

(16) Koh, C.-H.; Lee, S.; Kwak, M.; Kim, B.-S.; Chung, Y. CD8 T-Cell Subsets: Heterogeneity, Functions, and Therapeutic Potential. *Exp Mol Med* **2023**, *55* (11), 2287–2299. https://doi.org/10.1038/s12276-023-01105-x.

(17) Headland, S. E.; Norling, L. V. The Resolution of Inflammation: Principles and Challenges. *Seminars in Immunology* **2015**, *27* (3), 149–160. https://doi.org/10.1016/j.smim.2015.03.014.

(18) Dean, R. A.; Cox, J. H.; Bellac, C. L.; Doucet, A.; Starr, A. E.; Overall, C. M. Macrophage-Specific Metalloelastase (MMP-12) Truncates and Inactivates ELR+ CXC Chemokines and Generates CCL2, -7, -8, and -13 Antagonists: Potential Role of the Macrophage in Terminating Polymorphonuclear Leukocyte Influx. *Blood* **2008**, *112* (8), 3455–3464. https://doi.org/10.1182/blood-2007-12-129080.

(19) Ivashkiv, L. B. Epigenetic Regulation of Macrophage Polarization and Function. *Trends in Immunology* **2013**, *34* (5), 216–223. https://doi.org/10.1016/j.it.2012.11.001.

(20) Watanabe, S.; Alexander, M.; Misharin, A. V.; Budinger, G. R. S. The Role of Macrophages in the Resolution of Inflammation. *Journal of Clinical Investigation* **2019**, *129* (7), 2619–2628. https://doi.org/10.1172/jci124615.

(21) Basil, M. C.; Levy, B. D. Specialized Pro-Resolving Mediators: Endogenous Regulators of Infection and Inflammation. *Nat Rev Immunol* **2016**, *16* (1), 51–67. https://doi.org/10.1038/nri.2015.4.

(22) Julliard, W. A.; Myo, Y. P. A.; Perelas, A.; Jackson, P. D.; Thatcher, T. H.; Sime, P. J. Specialized Pro-Resolving Mediators as Modulators of Immune Responses. *Seminars in Immunology* **2022**, *59*, 101605. https://doi.org/10.1016/j.smim.2022.101605.

(23) Deng, Z.; Fan, T.; Xiao, C.; Tian, H.; Zheng, Y.; Li, C.; He, J. TGF-β Signaling in Health, Disease and Therapeutics. *Sig Transduct Target Ther* **2024**, *9* (1). https://doi.org/10.1038/s41392-024-01764-w.

(24) Savill, J. S.; Wyllie, A. H.; Henson, J. E.; Walport, M. J.; Henson, P. M.; Haslett, C. Macrophage Phagocytosis of Aging Neutrophils in Inflammation. Programmed Cell Death in the Neutrophil Leads to Its Recognition by Macrophages. *J. Clin. Invest.* **1989**, *83* (3), 865–875. https://doi.org/10.1172/jci113970.

(25) Herrero-Cervera, A.; Soehnlein, O.; Kenne, E. Neutrophils in Chronic Inflammatory Diseases. *Cell Mol Immunol* **2022**, *19* (2), 177–191. https://doi.org/10.1038/s41423-021-00832-3.

(26) Giovenzana, A.; Codazzi, V.; Pandolfo, M.; Petrelli, A. T Cell Trafficking in Human Chronic Inflammatory Diseases. *iScience* **2024**, *27* (8), 110528. https://doi.org/10.1016/j.isci.2024.110528.

(27) Gupta, L.; Thomas, J.; Ravichandran, R.; Singh, M.; Nag, A.; Panjiyar, B. K. Inflammation in Cardiovascular Disease: A Comprehensive Review of Biomarkers and Therapeutic Targets. *Cureus* **2023**. https://doi.org/10.7759/cureus.45483.

(28) Moore, K. J.; Sheedy, F. J.; Fisher, E. A. Macrophages in Atherosclerosis: A Dynamic Balance. *Nat Rev Immunol* **2013**, *13* (10), 709–721. https://doi.org/10.1038/nri3520.

(29) Kountouras, J. Innate Immunity and Nonalcoholic Fatty Liver Disease. *aog* **2023**. https://doi.org/10.20524/aog.2023.0793.

(30) Liaskou, E.; Wilson, D. V.; Oo, Y. H. Innate Immune Cells in Liver Inflammation. *Mediators of Inflammation* **2012**, *2012*, 1–21. https://doi.org/10.1155/2012/949157.

(31) Nathan, C. Points of Control in Inflammation. *Nature* **2002**, *420* (6917), 846–852. https://doi.org/10.1038/nature01320.

(32) Elbehiry, A.; Marzouk, E.; Aldubaib, M.; Abalkhail, A.; Anagreyyah, S.; Anajirih, N.; Almuzaini, A. M.; Rawway, M.; Alfadhel, A.; Draz, A.; Abu-Okail, A. Helicobacter Pylori Infection: Current Status and Future Prospects on Diagnostic, Therapeutic and Control Challenges. *Antibiotics (Basel)* **2023**, *12* (2), 191. https://doi.org/10.3390/antibiotics12020191.

(33) Babiker, A.; Hassan, M.; Muhammed, S.; Taylor, G.; Poonia, B.; Shah, A.; Bagchi, S. Inflammatory and Cardiovascular Diseases Biomarkers in Chronic Hepatitis C Virus Infection: A Review. *Clinical Cardiology* **2020**, *43* (3), 222–234. https://doi.org/10.1002/clc.23299.

(34) Khanna, D.; Khanna, S.; Khanna, P.; Kahar, P.; Patel, B. M. Obesity: A Chronic Low-Grade Inflammation and Its Markers. *Cureus* **2022**. https://doi.org/10.7759/cureus.22711.

(35) Tristan Asensi, M.; Napoletano, A.; Sofi, F.; Dinu, M. Low-Grade Inflammation and Ultra-Processed Foods Consumption: A Review. *Nutrients* **2023**, *15* (6), 1546. https://doi.org/10.3390/nu15061546.

(36) Burini, R. C.; Anderson, E.; Durstine, J. L.; Carson, J. A. Inflammation, Physical Activity, and Chronic Disease: An Evolutionary Perspective. *Sports Medicine and Health Science* **2020**, *2* (1), 1–6. https://doi.org/10.1016/j.smhs.2020.03.004.
(37) Fulton, S.; Décarie-Spain, L.; Fioramonti, X.; Guiard, B.; Nakajima, S. The Menace of Obesity to Depression and Anxiety Prevalence. *Trends in Endocrinology & Metabolism* **2022**, *33* (1), 18–35. https://doi.org/10.1016/j.tem.2021.10.005.
(38) Elisia, I.; Lam, V.; Cho, B.; Hay, M.; Li, M. Y.; Yeung, M.; Bu, L.; Jia, W.; Norton, N.; Lam, S.; Krystal, G. The Effect of Smoking on Chronic Inflammation, Immune Function and Blood Cell Composition. *Sci Rep* **2020**, *10* (1), 19480. https://doi.org/10.1038/s41598-020-76556-7.
(39) Lee, J.; Taneja, V.; Vassallo, R. Cigarette Smoking and Inflammation: Cellular and Molecular Mechanisms. *J Dent Res* **2012**, *91* (2), 142–149. https://doi.org/10.1177/0022034511421200.
(40) Placha, D.; Jampilek, J. Chronic Inflammatory Diseases, Anti-Inflammatory Agents and Their Delivery Nanosystems. *Pharmaceutics* **2021**, *13* (1), 64. https://doi.org/10.3390/pharmaceutics13010064.
(41) Kothari, M.; Wanjari, A.; Acharya, S.; Karwa, V.; Chavhan, R.; Kumar, S.; Kadu, A.; Patil, R. A Comprehensive Review of Monoclonal Antibodies in Modern Medicine: Tracing the Evolution of a Revolutionary Therapeutic Approach. *Cureus* **2024**. https://doi.org/10.7759/cureus.61983.
(42) Melo, A. T.; Campanilho-Marques, R.; Fonseca, J. E. Golimumab (Anti-TNF Monoclonal Antibody): Where We Stand Today. *Human Vaccines & Immunotherapeutics* **2021**, *17* (6), 1586–1598. https://doi.org/10.1080/21645515.2020.1836919.
(43) McInnes, I. B.; Gravallese, E. M. Immune-Mediated Inflammatory Disease Therapeutics: Past, Present and Future. *Nat Rev Immunol* **2021**, *21* (10), 680–686. https://doi.org/10.1038/s41577-021-00603-1.
(44) Solitano, V.; Yuan, Y.; Singh, S.; Ma, C.; Nardone, O. M.; Fiorino, G.; Acosta Felquer, M. L.; Barra, L.; D'Agostino, M.-A.; Pope, J.; Peyrin-Biroulet, L.; Danese, S.; Jairath, V. Efficacy and Safety of Advanced Combination Treatment in Immune-Mediated Inflammatory Disease: A Systematic Review and Meta-Analysis of Randomized Controlled Trials. *Journal of Autoimmunity* **2024**, *149*, 103331. https://doi.org/10.1016/j.jaut.2024.103331.
(45) Stoker, A. M. H.; Logghe, L.; Van Der Ende-van Loon, M. C. M.; Schoon, E. J.; Schreuder, R.-M.; Stronkhorst, A.; Gilissen, L. P. L. Relapse Rates after Withdrawal versus Maintaining Biologic Therapy in IBD Patients with Prolonged Remission. *Clin Exp Med* **2023**, *23* (6), 2789–2797. https://doi.org/10.1007/s10238-023-00994-6.
(46) Wongrakpanich, S.; Wongrakpanich, A.; Melhado, K.; Rangaswami, J. A Comprehensive Review of Non-Steroidal Anti-Inflammatory Drug Use in The Elderly. *Aging Dis* **2018**, *9* (1), 143–150. https://doi.org/10.14336/AD.2017.0306.
(47) Stone, S.; Malanga, G. A.; Capella, T. Corticosteroids: Review of the History, the Effectiveness, and Adverse Effects in the Treatment of Joint Pain. *Pain Physician* **2021**, *24* (S1), S233–S246.
(48) Checa, J.; Aran, J. M. Reactive Oxygen Species: Drivers of Physiological and Pathological Processes. *JIR* **2020**, *Volume 13*, 1057–1073. https://doi.org/10.2147/JIR.S275595.
(49) Ngo, V.; Duennwald, M. L. Nrf2 and Oxidative Stress: A General Overview of Mechanisms and Implications in Human Disease. *Antioxidants* **2022**, *11* (12), 2345. https://doi.org/10.3390/antiox11122345.
(50) Averill-Bates, D. Reactive Oxygen Species and Cell Signaling. Review. *Biochimica et Biophysica Acta (BBA) - Molecular Cell Research* **2024**, *1871* (2), 119573. https://doi.org/10.1016/j.bbamcr.2023.119573.
(51) Espinosa-Diez, C.; Miguel, V.; Mennerich, D.; Kietzmann, T.; Sánchez-Pérez, P.; Cadenas, S.; Lamas, S. Antioxidant Responses and Cellular Adjustments to Oxidative Stress. *Redox Biology* **2015**, *6*, 183–197. https://doi.org/10.1016/j.redox.2015.07.008.

(52) Tu, D.; Velagapudi, R.; Gao, Y.; Hong, J.-S.; Zhou, H.; Gao, H.-M. Activation of Neuronal NADPH Oxidase NOX2 Promotes Inflammatory Neurodegeneration. *Free Radical Biology and Medicine* **2023**, *200*, 47–58. https://doi.org/10.1016/j.freeradbiomed.2023.03.001.

(53) Geng, L.; Fan, L. M.; Liu, F.; Smith, C.; Li, J.-M. Nox2 Dependent Redox-Regulation of Microglial Response to Amyloid-β Stimulation and Microgliosis in Aging. *Sci Rep* **2020**, *10* (1), 1582. https://doi.org/10.1038/s41598-020-58422-8.

(54) Shi, X.; Li, P.; Herb, M.; Liu, H.; Wang, M.; Wang, X.; Feng, Y.; Van Beers, T.; Xia, N.; Li, H.; Prokosch, V. Pathological High Intraocular Pressure Induces Glial Cell Reactive Proliferation Contributing to Neuroinflammation of the Blood-Retinal Barrier via the NOX2/ET-1 Axis-Controlled ERK1/2 Pathway. *J Neuroinflammation* **2024**, *21* (1), 105. https://doi.org/10.1186/s12974-024-03075-x.

(55) Jiang, S.; Zhang, B.; Wen, S.; Cheng, S.; Shen, Y.; Xie, S.; Xie, Z.; Jiang, W. NOX2 Mediates NLRP3/ROS Facilitating Nasal Mucosal Epithelial Inflammation in Chronic Rhinosinusitis with Nasal Polyps. *Heliyon* **2024**, *10* (18), e38029. https://doi.org/10.1016/j.heliyon.2024.e38029.

(56) Chen, Y.; Ye, X.; Escames, G.; Lei, W.; Zhang, X.; Li, M.; Jing, T.; Yao, Y.; Qiu, Z.; Wang, Z.; Acuña-Castroviejo, D.; Yang, Y. The NLRP3 Inflammasome: Contributions to Inflammation-Related Diseases. *Cell Mol Biol Lett* **2023**, *28* (1), 51. https://doi.org/10.1186/s11658-023-00462-9.

(57) Hsu, C.-K.; Lee, I.-T.; Lin, C.-C.; Hsiao, L.-D.; Yang, C.-M. Nox2/ROS-Dependent Human Antigen R Translocation Contributes to TNF-α-Induced SOCS-3 Expression in Human Tracheal Smooth Muscle Cells. *American Journal of Physiology-Lung Cellular and Molecular Physiology* **2014**, *306* (6), L521–L533. https://doi.org/10.1152/ajplung.00274.2013.

(58) Yan Wang, Y. W.; Wanpin Nie, W. N.; Kai Yao, K. Y.; Zheng Wang, Z. W.; Hao He, H. H. Interleukin 6 Induces Expression of NADPH Oxidase 2 in Human Aortic Endothelial Cells via Long Noncoding RNA MALAT1. *Pharmazie* **2016**, No. 10, 592–597. https://doi.org/10.1691/ph.2016.6598.

(59) Moi, P.; Chan, K.; Asunis, I.; Cao, A.; Kan, Y. W. Isolation of NF-E2-Related Factor 2 (Nrf2), a NF-E2-like Basic Leucine Zipper Transcriptional Activator That Binds to the Tandem NF-E2/AP1 Repeat of the Beta-Globin Locus Control Region. *Proc. Natl. Acad. Sci. U.S.A.* **1994**, *91* (21), 9926–9930. https://doi.org/10.1073/pnas.91.21.9926.

(60) Chan, K.; Lu, R.; Chang, J. C.; Kan, Y. W. NRF2, a Member of the NFE2 Family of Transcription Factors, Is Not Essential for Murine Erythropoiesis, Growth, and Development. *Proc. Natl. Acad. Sci. U.S.A.* **1996**, *93* (24), 13943–13948. https://doi.org/10.1073/pnas.93.24.13943.

(61) Morgenstern, C.; Lastres-Becker, I.; Demirdöğen, B. C.; Costa, V. M.; Daiber, A.; Foresti, R.; Motterlini, R.; Kalyoncu, S.; Arioz, B. I.; Genc, S.; Jakubowska, M.; Trougakos, I. P.; Piechota-Polanczyk, A.; Mickael, M.; Santos, M.; Kensler, T. W.; Cuadrado, A.; Copple, I. M. Biomarkers of NRF2 Signalling: Current Status and Future Challenges. *Redox Biology* **2024**, *72*, 103134. https://doi.org/10.1016/j.redox.2024.103134.

(62) He, F.; Ru, X.; Wen, T. NRF2, a Transcription Factor for Stress Response and Beyond. *IJMS* **2020**, *21* (13), 4777. https://doi.org/10.3390/ijms21134777.

(63) Zhang, H.; Forman, H. J. Reexamination of the Electrophile Response Element Sequences and Context Reveals a Lack of Consensus in Gene Function. *Biochimica et Biophysica Acta (BBA) - Gene Regulatory Mechanisms* **2010**, *1799* (7), 496–501. https://doi.org/10.1016/j.bbagrm.2010.05.003.

(64) Itoh, K.; Chiba, T.; Takahashi, S.; Ishii, T.; Igarashi, K.; Katoh, Y.; Oyake, T.; Hayashi, N.; Satoh, K.; Hatayama, I.; Yamamoto, M.; Nabeshima, Y. An Nrf2/Small Maf Heterodimer Mediates the Induction of Phase II Detoxifying Enzyme Genes through Antioxidant Response Elements. *Biochemical and Biophysical Research Communications* **1997**, *236* (2), 313–322. https://doi.org/10.1006/bbrc.1997.6943.

(65) Bianchet, M. A.; Faig, M.; Amzel, L. M. Structure and Mechanism of NAD[P]H:Quinone Acceptor Oxidoreductases (NQO). In *Methods in Enzymology*; Elsevier, 2004; Vol. 382, pp 144–174. https://doi.org/10.1016/S0076-6879(04)82009-3.

(66) Tedeschi, G.; Chen, S.; Massey, V. DT-Diaphorase. *Journal of Biological Chemistry* **1995**, *270* (3), 1198–1204. https://doi.org/10.1074/jbc.270.3.1198.

(67) Alam, J.; Stewart, D.; Touchard, C.; Boinapally, S.; Choi, A. M. K.; Cook, J. L. Nrf2, a Cap'n'Collar Transcription Factor, Regulates Induction of the Heme Oxygenase-1 Gene. *Journal of Biological Chemistry* **1999**, *274* (37), 26071–26078. https://doi.org/10.1074/jbc.274.37.26071.

(68) Pae, H.-O.; Chung, H.-T. Heme Oxygenase-1: Its Therapeutic Roles in Inflammatory Diseases. *Immune Netw* **2009**, *9* (1), 12. https://doi.org/10.4110/in.2009.9.1.12.

(69) Jena, A. B.; Samal, R. R.; Bhol, N. K.; Duttaroy, A. K. Cellular Red-Ox System in Health and Disease: The Latest Update. *Biomedicine & Pharmacotherapy* **2023**, *162*, 114606. https://doi.org/10.1016/j.biopha.2023.114606.

(70) Vitali, S. H.; Fernandez-Gonzalez, A.; Nadkarni, J.; Kwong, A.; Rose, C.; Mitsialis, S. A.; Kourembanas, S. Heme Oxygenase-1 Dampens the Macrophage Sterile Inflammasome Response and Regulates Its Components in the Hypoxic Lung. *American Journal of Physiology-Lung Cellular and Molecular Physiology* **2020**, *318* (1), L125–L134. https://doi.org/10.1152/ajplung.00074.2019.

(71) Zhou, R.; Tardivel, A.; Thorens, B.; Choi, I.; Tschopp, J. Thioredoxin-Interacting Protein Links Oxidative Stress to Inflammasome Activation. *Nat Immunol* **2010**, *11* (2), 136–140. https://doi.org/10.1038/ni.1831.

(72) Potteti, H. R.; Venkareddy, L. K.; Noone, P. M.; Ankireddy, A.; Tamatam, C. R.; Mehta, D.; Tiruppathi, C.; Reddy, S. P. Nrf2 Regulates Anti-Inflammatory A20 Deubiquitinase Induction by LPS in Macrophages in Contextual Manner. *Antioxidants* **2021**, *10* (6), 847. https://doi.org/10.3390/antiox10060847.

(73) Li, Z.; Wang, Q.; Zhang, Z.; Zhang, X.; Wu, X.; Li, L.; Zhang, Y.; Yu, Y. A20, as a Downstream Factor of Nrf2, Is Involved in the Anti-Neuroinflammatory and Antidepressant-like Effects of Luteolin. *Journal of Functional Foods* **2022**, *99*, 105305. https://doi.org/10.1016/j.jff.2022.105305.

(74) Liu, M.; Grigoryev, D. N.; Crow, M. T.; Haas, M.; Yamamoto, M.; Reddy, S. P.; Rabb, H. Transcription Factor Nrf2 Is Protective during Ischemic and Nephrotoxic Acute Kidney Injury in Mice. *Kidney International* **2009**, *76* (3), 277–285. https://doi.org/10.1038/ki.2009.157.

(75) Yoh, K.; Hirayama, A.; Ishizaki, K.; Yamada, A.; Takeuchi, M.; Yamagishi, S.; Morito, N.; Nakano, T.; Ojima, M.; Shimohata, H.; Itoh, K.; Takahashi, S.; Yamamoto, M. Hyperglycemia Induces Oxidative and Nitrosative Stress and Increases Renal Functional Impairment in Nrf2-deficient Mice. *Genes to Cells* **2008**, *13* (11), 1159–1170. https://doi.org/10.1111/j.1365-2443.2008.01234.x.

(76) Freigang, S.; Ampenberger, F.; Spohn, G.; Heer, S.; Shamshiev, A. T.; Kisielow, J.; Hersberger, M.; Yamamoto, M.; Bachmann, M. F.; Kopf, M. Nrf2 Is Essential for Cholesterol Crystal-induced Inflammasome Activation and Exacerbation of Atherosclerosis. *Eur J Immunol* **2011**, *41* (7), 2040–2051. https://doi.org/10.1002/eji.201041316.

(77) Yagishita, Y.; Fukutomi, T.; Sugawara, A.; Kawamura, H.; Takahashi, T.; Pi, J.; Uruno, A.; Yamamoto, M. Nrf2 Protects Pancreatic β-Cells From Oxidative and Nitrosative Stress in Diabetic Model Mice. *Diabetes* **2014**, *63* (2), 605–618. https://doi.org/10.2337/db13-0909.

(78) Okada, K.; Warabi, E.; Sugimoto, H.; Horie, M.; Gotoh, N.; Tokushige, K.; Hashimoto, E.; Utsunomiya, H.; Takahashi, H.; Ishii, T.; Yamamoto, M.; Shoda, J. Deletion of Nrf2 Leads to Rapid Progression of Steatohepatitis in Mice Fed Atherogenic plus High-Fat Diet. *J Gastroenterol* **2013**, *48* (5), 620–632. https://doi.org/10.1007/s00535-012-0659-z.

(79) Yagishita, Y.; Uruno, A.; Chartoumpekis, D. V.; Kensler, T. W.; Yamamoto, M. Nrf2 Represses the Onset of Type 1 Diabetes in Non-Obese Diabetic Mice. *Journal of Endocrinology* **2019**, *240* (3), 403–416. https://doi.org/10.1530/joe-18-0355.

(80) Miyazaki, Y.; Shimizu, A.; Pastan, I.; Taguchi, K.; Naganuma, E.; Suzuki, T.; Hosoya, T.; Yokoo, T.; Saito, A.; Miyata, T.; Yamamoto, M.; Matsusaka, T. Keap1 Inhibition Attenuates Glomerulosclerosis. *Nephrology Dialysis Transplantation* **2014**, *29* (4), 783–791. https://doi.org/10.1093/ndt/gfu002.

(81) De Plano, L. M.; Calabrese, G.; Rizzo, M. G.; Oddo, S.; Caccamo, A. The Role of the Transcription Factor Nrf2 in Alzheimer's Disease: Therapeutic Opportunities. *Biomolecules* **2023**, *13* (3), 549. https://doi.org/10.3390/biom13030549.

(82) Yuhan, L.; Khaleghi Ghadiri, M.; Gorji, A. Impact of NQO1 Dysregulation in CNS Disorders. *J Transl Med* **2024**, *22* (1), 4. https://doi.org/10.1186/s12967-023-04802-3.

(83) Rojo, A. I.; Pajares, M.; Rada, P.; Nuñez, A.; Nevado-Holgado, A. J.; Killik, R.; Van Leuven, F.; Ribe, E.; Lovestone, S.; Yamamoto, M.; Cuadrado, A. NRF2 Deficiency Replicates Transcriptomic Changes in Alzheimer's Patients and Worsens APP and TAU Pathology. *Redox Biology* **2017**, *13*, 444–451. https://doi.org/10.1016/j.redox.2017.07.006.

(84) Bahn, G.; Park, J.-S.; Yun, U. J.; Lee, Y. J.; Choi, Y.; Park, J. S.; Baek, S. H.; Choi, B. Y.; Cho, Y. S.; Kim, H. K.; Han, J.; Sul, J. H.; Baik, S.-H.; Lim, J.; Wakabayashi, N.; Bae, S. H.; Han, J.-W.; Arumugam, T. V.; Mattson, M. P.; Jo, D.-G. NRF2/ARE Pathway Negatively Regulates BACE1 Expression and Ameliorates Cognitive Deficits in Mouse Alzheimer's Models. *Proc. Natl. Acad. Sci. U.S.A.* **2019**, *116* (25), 12516–12523. https://doi.org/10.1073/pnas.1819541116.

(85) Ren, P.; Chen, J.; Li, B.; Zhang, M.; Yang, B.; Guo, X.; Chen, Z.; Cheng, H.; Wang, P.; Wang, S.; Wang, N.; Zhang, G.; Wu, X.; Ma, D.; Guan, D.; Zhao, R. Nrf2 Ablation Promotes Alzheimer's Disease-Like Pathology in APP/PS1 Transgenic Mice: The Role of Neuroinflammation and Oxidative Stress. *Oxidative Medicine and Cellular Longevity* **2020**, *2020*, 1–13. https://doi.org/10.1155/2020/3050971.

(86) Oksanen, M.; Hyötyläinen, I.; Trontti, K.; Rolova, T.; Wojciechowski, S.; Koskuvi, M.; Viitanen, M.; Levonen, A.; Hovatta, I.; Roybon, L.; Lehtonen, Š.; Kanninen, K. M.; Hämäläinen, R. H.; Koistinaho, J. NF-E2-related Factor 2 Activation Boosts Antioxidant Defenses and Ameliorates Inflammatory and Amyloid Properties in Human Presenilin-1 Mutated Alzheimer's Disease Astrocytes. *Glia* **2020**, *68* (3), 589–599. https://doi.org/10.1002/glia.23741.

(87) Gibson, G. E.; Luchsinger, J. A.; Cirio, R.; Chen, H.; Franchino-Elder, J.; Hirsch, J. A.; Bettendorff, L.; Chen, Z.; Flowers, S. A.; Gerber, L. M.; Grandville, T.; Schupf, N.; Xu, H.; Stern, Y.; Habeck, C.; Jordan, B.; Fonzetti, P. Benfotiamine and Cognitive Decline in Alzheimer's Disease: Results of a Randomized Placebo-Controlled Phase IIa Clinical Trial. *JAD* **2020**, *78* (3), 989–1010. https://doi.org/10.3233/JAD-200896.

(88) Qiu, D.; Song, S.; Chen, N.; Bian, Y.; Yuan, C.; Zhang, W.; Duan, H.; Shi, Y. NQO1 Alleviates Renal Fibrosis by Inhibiting the TLR4/NF-κB and TGF-β/Smad Signaling Pathways in Diabetic Nephropathy. *Cellular Signalling* **2023**, *108*, 110712. https://doi.org/10.1016/j.cellsig.2023.110712.

(89) Di Francesco, A.; Choi, Y.; Bernier, M.; Zhang, Y.; Diaz-Ruiz, A.; Aon, M. A.; Kalafut, K.; Ehrlich, M. R.; Murt, K.; Ali, A.; Pearson, K. J.; Levan, S.; Preston, J. D.; Martin-Montalvo, A.; Martindale, J. L.; Abdelmohsen, K.; Michel, C. R.; Willmes, D. M.; Henke, C.; Navas, P.; Villalba, J. M.; Siegel, D.; Gorospe, M.; Fritz, K.; Biswal, S.; Ross, D.; De Cabo, R. NQO1 Protects Obese Mice through Improvements in Glucose and Lipid Metabolism. *npj Aging Mech Dis* **2020**, *6* (1). https://doi.org/10.1038/s41514-020-00051-6.

(90) Chen, W.; Wu, Z.; Cheng, Z.; Zhang, Y.; Luo, Q.; Yin, M. HO-1 Represses NF-κB Signaling Pathway to Mediate Microglia Polarization and Phagocytosis in Intracerebral Hemorrhage. *Neuroscience* **2025**, *566*, 17–27. https://doi.org/10.1016/j.neuroscience.2024.12.020.

(91) Yet, S.-F.; Layne, M. D.; Liu, X.; Chen, Y.-H.; Ith, B.; Sibinga, N. E. S.; Perrella, M. A. Absence of Heme Oxygenase-1 Exacerbates Atherosclerotic Lesion Formation and Vascular Remodeling. *FASEB j.* **2003**, *17* (12), 1759–1761. https://doi.org/10.1096/fj.03-0187fje.

(92) Pechlaner, R.; Willeit, P.; Summerer, M.; Santer, P.; Egger, G.; Kronenberg, F.; Demetz, E.; Weiss, G.; Tsimikas, S.; Witztum, J. L.; Willeit, K.; Iglseder, B.; Paulweber, B.; Kedenko, L.; Haun, M.; Meisinger, C.; Gieger, C.; Müller-Nurasyid, M.; Peters, A.; Willeit, J.; Kiechl, S. Heme Oxygenase-1 Gene Promoter Microsatellite Polymorphism Is Associated With Progressive Atherosclerosis and Incident Cardiovascular Disease. *ATVB* **2015**, *35* (1), 229–236. https://doi.org/10.1161/atvbaha.114.304729.

(93) Zhang, Q.; Liu, J.; Duan, H.; Li, R.; Peng, W.; Wu, C. Activation of Nrf2/HO-1 Signaling: An Important Molecular Mechanism of Herbal Medicine in the Treatment of Atherosclerosis via the Protection of Vascular Endothelial Cells from Oxidative Stress. *Journal of Advanced Research* **2021**, *34*, 43–63. https://doi.org/10.1016/j.jare.2021.06.023.

(94) Li, N.; Hao, L.; Li, S.; Deng, J.; Yu, F.; Zhang, J.; Nie, A.; Hu, X. The NRF-2/HO-1 Signaling Pathway: A Promising Therapeutic Target for Metabolic Dysfunction-Associated Steatotic Liver Disease. *JIR* **2024**, *Volume 17*, 8061–8083. https://doi.org/10.2147/JIR.S490418.

(95) Yuan, L.; Wang, Y.; Li, N.; Yang, X.; Sun, X.; Tian, H.; Zhang, Y. Mechanism of Action and Therapeutic Implications of Nrf2/HO-1 in Inflammatory Bowel Disease. *Antioxidants* **2024**, *13* (8), 1012. https://doi.org/10.3390/antiox13081012.

(96) O'Rourke, S. A.; Shanley, L. C.; Dunne, A. The Nrf2-HO-1 System and Inflammaging. *Front. Immunol.* **2024**, *15*, 1457010. https://doi.org/10.3389/fimmu.2024.1457010.

(97) Zhang, M.; Nakamura, K.; Kageyama, S.; Lawal, A. O.; Gong, K. W.; Bhetraratana, M.; Fujii, T.; Sulaiman, D.; Hirao, H.; Bolisetty, S.; Kupiec-Weglinski, J. W.; Araujo, J. A. Myeloid HO-1 Modulates Macrophage Polarization and Protects against Ischemia-Reperfusion Injury. *JCI Insight* **2018**, *3* (19). https://doi.org/10.1172/jci.insight.120596.

(98) Wang, Y.; Fu, X.; Zeng, L.; Hu, Y.; Gao, R.; Xian, S.; Liao, S.; Huang, J.; Yang, Y.; Liu, J.; Jin, H.; Klaunig, J.; Lu, Y.; Zhou, S. Activation of Nrf2/HO-1 Signaling Pathway Exacerbates Cholestatic Liver Injury. *Commun Biol* **2024**, *7* (1), 621. https://doi.org/10.1038/s42003-024-06243-0.

(99) Buendia, I.; Michalska, P.; Navarro, E.; Gameiro, I.; Egea, J.; León, R. Nrf2–ARE Pathway: An Emerging Target against Oxidative Stress and Neuroinflammation in Neurodegenerative Diseases. *Pharmacology & Therapeutics* **2016**, *157*, 84–104. https://doi.org/10.1016/j.pharmthera.2015.11.003.

(100) Khan, S. U.; Khan, S. U.; Suleman, M.; Khan, M. U.; Khan, M. S.; Arbi, F. M.; Hussain, T.; Mohammed Alsuhaibani, A.; S Refat, M. Natural Allies for Heart Health: Nrf2 Activation and Cardiovascular Disease Management. *Current Problems in Cardiology* **2024**, *49* (1), 102084. https://doi.org/10.1016/j.cpcardiol.2023.102084.

(101) Nezu, M.; Suzuki, N. Roles of Nrf2 in Protecting the Kidney from Oxidative Damage. *IJMS* **2020**, *21* (8), 2951. https://doi.org/10.3390/ijms21082951.

(102) Liu, Q.; Gao, Y.; Ci, X. Role of Nrf2 and Its Activators in Respiratory Diseases. *Oxidative Medicine and Cellular Longevity* **2019**, *2019*, 1–17. https://doi.org/10.1155/2019/7090534.

(103) Piotrowska, M.; Swierczynski, M.; Fichna, J.; Piechota-Polanczyk, A. The Nrf2 in the Pathophysiology of the Intestine: Molecular Mechanisms and Therapeutic Implications for Inflammatory Bowel Diseases. *Pharmacological Research* **2021**, *163*, 105243. https://doi.org/10.1016/j.phrs.2020.105243.

(104) Li, B.; Wang, Y.; Jiang, X.; Du, H.; Shi, Y.; Xiu, M.; Liu, Y.; He, J. Natural Products Targeting Nrf2/ARE Signaling Pathway in the Treatment of Inflammatory Bowel Disease. *Biomedicine & Pharmacotherapy* **2023**, *164*, 114950. https://doi.org/10.1016/j.biopha.2023.114950.

(105) Glorieux, C.; Enríquez, C.; González, C.; Aguirre-Martínez, G.; Buc Calderon, P. The Multifaceted Roles of NRF2 in Cancer: Friend or Foe? *Antioxidants* **2024**, *13* (1), 70. https://doi.org/10.3390/antiox13010070.

(106) Pei, Y.; Yin, J.; Liu, J.; Liu, D.; Wu, Q.; Cai, X.; Han, M.; Tian, Y.; Yang, L.; Liu, S. The Role of NRF2 in Human Cancers: Pre-Clinical Insights Paving the Way for Clinical Trials.

Journal of Pharmaceutical Analysis **2025**, 101358. https://doi.org/10.1016/j.jpha.2025.101358.

(107) Ibrahim, L.; Mesgarzadeh, J.; Xu, I.; Powers, E. T.; Wiseman, R. L.; Bollong, M. J. Defining the Functional Targets of Cap‘n’Collar Transcription Factors NRF1, NRF2, and NRF3. *Antioxidants* **2020**, *9* (10), 1025. https://doi.org/10.3390/antiox9101025.

(108) Canning, P.; Sorrell, F. J.; Bullock, A. N. Structural Basis of Keap1 Interactions with Nrf2. *Free Radical Biology and Medicine* **2015**, *88*, 101–107. https://doi.org/10.1016/j.freeradbiomed.2015.05.034.

(109) Karunatilleke, N. C.; Fast, C. S.; Ngo, V.; Brickenden, A.; Duennwald, M. L.; Konermann, L.; Choy, W.-Y. Nrf2, the Major Regulator of the Cellular Oxidative Stress Response, Is Partially Disordered. *Int J Mol Sci* **2021**, *22* (14), 7434. https://doi.org/10.3390/ijms22147434.

(110) Hayes, J. D.; Dayalan Naidu, S.; Dinkova-Kostova, A. T. Regulating Nrf2 Activity: Ubiquitin Ligases and Signaling Molecules in Redox Homeostasis. *Trends in Biochemical Sciences* **2025**, *50* (3), 179–205. https://doi.org/10.1016/j.tibs.2024.12.010.

(111) Itoh, K.; Wakabayashi, N.; Katoh, Y.; Ishii, T.; Igarashi, K.; Engel, J. D.; Yamamoto, M. Keap1 Represses Nuclear Activation of Antioxidant Responsive Elements by Nrf2 through Binding to the Amino-Terminal Neh2 Domain. *Genes Dev.* **1999**, *13* (1), 76–86. https://doi.org/10.1101/gad.13.1.76.

(112) Tong, K. I.; Katoh, Y.; Kusunoki, H.; Itoh, K.; Tanaka, T.; Yamamoto, M. Keap1 Recruits Neh2 through Binding to ETGE and DLG Motifs: Characterization of the Two-Site Molecular Recognition Model. *Molecular and Cellular Biology* **2006**, *26* (8), 2887–2900. https://doi.org/10.1128/MCB.26.8.2887-2900.2006.

(113) Nioi, P.; Nguyen, T.; Sherratt, P. J.; Pickett, C. B. The Carboxy-Terminal Neh3 Domain of Nrf2 Is Required for Transcriptional Activation. *Molecular and Cellular Biology* **2005**, *25* (24), 10895–10906. https://doi.org/10.1128/MCB.25.24.10895-10906.2005.

(114) Poh, J.; Ponsford, A. H.; Boyd, J.; Woodsmith, J.; Stelzl, U.; Wanker, E.; Harper, N.; MacEwan, D.; Sanderson, C. M. A Functionally Defined High-Density NRF2 Interactome Reveals New Conditional Regulators of ARE Transactivation. *Redox Biology* **2020**, *37*, 101686. https://doi.org/10.1016/j.redox.2020.101686.

(115) Sun, Z.; Chin, Y. E.; Zhang, D. D. Acetylation of Nrf2 by P300/CBP Augments Promoter-Specific DNA Binding of Nrf2 during the Antioxidant Response. *Molecular and Cellular Biology* **2009**, *29* (10), 2658–2672. https://doi.org/10.1128/MCB.01639-08.

(116) Katoh, Y.; Itoh, K.; Yoshida, E.; Miyagishi, M.; Fukamizu, A.; Yamamoto, M. Two Domains of Nrf2 Cooperatively Bind CBP, a CREB Binding Protein, and Synergistically Activate Transcription. *Genes to Cells* **2001**, *6* (10), 857–868. https://doi.org/10.1046/j.1365-2443.2001.00469.x.

(117) Karunatilleke, N. C.; Brickenden, A.; Choy, W. Molecular Basis of the Interactions between the Disordered NEH4 and NEH5 Domains of NRF2 and CBP /P300 in Oxidative Stress Response. *Protein Science* **2024**, *33* (9), e5137. https://doi.org/10.1002/pro.5137.

(118) Zhang, J.; Ohta, T.; Maruyama, A.; Hosoya, T.; Nishikawa, K.; Maher, J. M.; Shibahara, S.; Itoh, K.; Yamamoto, M. BRG1 Interacts with Nrf2 To Selectively Mediate *HO-1* Induction in Response to Oxidative Stress. *Molecular and Cellular Biology* **2006**, *26* (21), 7942–7952. https://doi.org/10.1128/MCB.00700-06.

(119) McMahon, M.; Thomas, N.; Itoh, K.; Yamamoto, M.; Hayes, J. D. Redox-Regulated Turnover of Nrf2 Is Determined by at Least Two Separate Protein Domains, the Redox-Sensitive Neh2 Degron and the Redox-Insensitive Neh6 Degron. *Journal of Biological Chemistry* **2004**, *279* (30), 31556–31567. https://doi.org/10.1074/jbc.M403061200.

(120) Rada, P.; Rojo, A. I.; Chowdhry, S.; McMahon, M.; Hayes, J. D.; Cuadrado, A. SCF/β-TrCP Promotes Glycogen Synthase Kinase 3-Dependent Degradation of the Nrf2 Transcription Factor in a Keap1-Independent Manner. *Molecular and Cellular Biology* **2011**, *31* (6), 1121–1133. https://doi.org/10.1128/MCB.01204-10.

(121) Wang, H.; Liu, K.; Geng, M.; Gao, P.; Wu, X.; Hai, Y.; Li, Y.; Li, Y.; Luo, L.; Hayes, J. D.; Wang, X. J.; Tang, X. RXRα Inhibits the NRF2-ARE Signaling Pathway through a

Direct Interaction with the Neh7 Domain of NRF2. *Cancer Research* **2013**, *73* (10), 3097–3108. https://doi.org/10.1158/0008-5472.CAN-12-3386.

(122) Stewart, D.; Killeen, E.; Naquin, R.; Alam, S.; Alam, J. Degradation of Transcription Factor Nrf2 via the Ubiquitin-Proteasome Pathway and Stabilization by Cadmium. *Journal of Biological Chemistry* **2003**, *278* (4), 2396–2402. https://doi.org/10.1074/jbc.M209195200.

(123) Itoh, K.; Wakabayashi, N.; Katoh, Y.; Ishii, T.; O'Connor, T.; Yamamoto, M. Keap1 Regulates Both Cytoplasmic-nuclear Shuttling and Degradation of Nrf2 in Response to Electrophiles. *Genes to Cells* **2003**, *8* (4), 379–391. https://doi.org/10.1046/j.1365-2443.2003.00640.x.

(124) Kobayashi, A.; Kang, M.-I.; Okawa, H.; Ohtsuji, M.; Zenke, Y.; Chiba, T.; Igarashi, K.; Yamamoto, M. Oxidative Stress Sensor Keap1 Functions as an Adaptor for Cul3-Based E3 Ligase To Regulate Proteasomal Degradation of Nrf2. *Molecular and Cellular Biology* **2004**, *24* (16), 7130–7139. https://doi.org/10.1128/MCB.24.16.7130-7139.2004.

(125) Choo, Y. Y.; Hagen, T. Mechanism of Cullin3 E3 Ubiquitin Ligase Dimerization. *PLoS ONE* **2012**, *7* (7), e41350. https://doi.org/10.1371/journal.pone.0041350.

(126) Dhanoa, B. S.; Cogliati, T.; Satish, A. G.; Bruford, E. A.; Friedman, J. S. Update on the Kelch-like (KLHL) Gene Family. *Hum Genomics* **2013**, *7* (1), 13. https://doi.org/10.1186/1479-7364-7-13.

(127) Shi, X.; Xiang, S.; Cao, J.; Zhu, H.; Yang, B.; He, Q.; Ying, M. Kelch-like Proteins: Physiological Functions and Relationships with Diseases. *Pharmacological Research* **2019**, *148*, 104404. https://doi.org/10.1016/j.phrs.2019.104404.

(128) Ogura, T.; Tong, K. I.; Mio, K.; Maruyama, Y.; Kurokawa, H.; Sato, C.; Yamamoto, M. Keap1 Is a Forked-Stem Dimer Structure with Two Large Spheres Enclosing the Intervening, Double Glycine Repeat, and C-Terminal Domains. *Proc. Natl. Acad. Sci. U.S.A.* **2010**, *107* (7), 2842–2847. https://doi.org/10.1073/pnas.0914036107.

(129) Zipper, L. M.; Mulcahy, R. T. The Keap1 BTB/POZ Dimerization Function Is Required to Sequester Nrf2 in Cytoplasm. *Journal of Biological Chemistry* **2002**, *277* (39), 36544–36552. https://doi.org/10.1074/jbc.M206530200.

(130) Cleasby, A.; Yon, J.; Day, P. J.; Richardson, C.; Tickle, I. J.; Williams, P. A.; Callahan, J. F.; Carr, R.; Concha, N.; Kerns, J. K.; Qi, H.; Sweitzer, T.; Ward, P.; Davies, T. G. Structure of the BTB Domain of Keap1 and Its Interaction with the Triterpenoid Antagonist CDDO. *PLoS ONE* **2014**, *9* (6), e98896. https://doi.org/10.1371/journal.pone.0098896.

(131) Adamson, R. J.; Payne, N. C.; Bartual, S. G.; Mazitschek, R.; Bullock, A. N. Structural and Biochemical Characterization Establishes a Detailed Understanding of KEAP1-CUL3 Complex Assembly. *Free Radical Biology and Medicine* **2023**, *204*, 215–225. https://doi.org/10.1016/j.freeradbiomed.2023.04.021.

(132) Li, X.; Zhang, D.; Hannink, M.; Beamer, L. J. Crystal Structure of the Kelch Domain of Human Keap1. *Journal of Biological Chemistry* **2004**, *279* (52), 54750–54758. https://doi.org/10.1074/jbc.m410073200.

(133) Lo, S.-C.; Li, X.; Henzl, M. T.; Beamer, L. J.; Hannink, M. Structure of the Keap1:Nrf2 Interface Provides Mechanistic Insight into Nrf2 Signaling. *EMBO J* **2006**, *25* (15), 3605–3617. https://doi.org/10.1038/sj.emboj.7601243.

(134) Padmanabhan, B.; Tong, K. I.; Ohta, T.; Nakamura, Y.; Scharlock, M.; Ohtsuji, M.; Kang, M.-I.; Kobayashi, A.; Yokoyama, S.; Yamamoto, M. Structural Basis for Defects of Keap1 Activity Provoked by Its Point Mutations in Lung Cancer. *Molecular Cell* **2006**, *21* (5), 689–700. https://doi.org/10.1016/j.molcel.2006.01.013.

(135) Tong, K. I.; Padmanabhan, B.; Kobayashi, A.; Shang, C.; Hirotsu, Y.; Yokoyama, S.; Yamamoto, M. Different Electrostatic Potentials Define ETGE and DLG Motifs as Hinge and Latch in Oxidative Stress Response. *Molecular and Cellular Biology* **2007**, *27* (21), 7511–7521. https://doi.org/10.1128/mcb.00753-07.

(136) Fukutomi, T.; Takagi, K.; Mizushima, T.; Ohuchi, N.; Yamamoto, M. Kinetic, Thermodynamic, and Structural Characterizations of the Association between Nrf2-

DLGex Degron and Keap1. *Molecular and Cellular Biology* **2014**, *34* (5), 832–846. https://doi.org/10.1128/mcb.01191-13.

(137) Robertson, H.; Hayes, J. D.; Sutherland, C. A Partnership with the Proteasome; the Destructive Nature of GSK3. *Biochemical Pharmacology* **2018**, *147*, 77–92. https://doi.org/10.1016/j.bcp.2017.10.016.

(138) Chowdhry, S.; Zhang, Y.; McMahon, M.; Sutherland, C.; Cuadrado, A.; Hayes, J. D. Nrf2 Is Controlled by Two Distinct β-TrCP Recognition Motifs in Its Neh6 Domain, One of Which Can Be Modulated by GSK-3 Activity. *Oncogene* **2013**, *32* (32), 3765–3781. https://doi.org/10.1038/onc.2012.388.

(139) Salazar, M.; Rojo, A. I.; Velasco, D.; De Sagarra, R. M.; Cuadrado, A. Glycogen Synthase Kinase-3β Inhibits the Xenobiotic and Antioxidant Cell Response by Direct Phosphorylation and Nuclear Exclusion of the Transcription Factor Nrf2. *Journal of Biological Chemistry* **2006**, *281* (21), 14841–14851. https://doi.org/10.1074/jbc.m513737200.

(140) Zhang, J.; Zhang, J.; Ni, H.; Wang, Y.; Katwal, G.; Zhao, Y.; Sun, K.; Wang, M.; Li, Q.; Chen, G.; Miao, Y.; Gong, N. Downregulation of XBP1 Protects Kidney against Ischemia-Reperfusion Injury via Suppressing HRD1-Mediated NRF2 Ubiquitylation. *Cell Death Discov.* **2021**, *7* (1). https://doi.org/10.1038/s41420-021-00425-z.

(141) Wu, T.; Zhao, F.; Gao, B.; Tan, C.; Yagishita, N.; Nakajima, T.; Wong, P. K.; Chapman, E.; Fang, D.; Zhang, D. D. Hrd1 Suppresses Nrf2-Mediated Cellular Protection during Liver Cirrhosis. *Genes Dev.* **2014**, *28* (7), 708–722. https://doi.org/10.1101/gad.238246.114.

(142) Lo, J. Y.; Spatola, B. N.; Curran, S. P. WDR23 Regulates NRF2 Independently of KEAP1. *PLoS Genet* **2017**, *13* (4), e1006762. https://doi.org/10.1371/journal.pgen.1006762.

(143) Rushworth, S. A.; MacEwan, D. J.; O'Connell, M. A. Lipopolysaccharide-Induced Expression of NAD(P)H:Quinone Oxidoreductase 1 and Heme Oxygenase-1 Protects against Excessive Inflammatory Responses in Human Monocytes. *The Journal of Immunology* **2008**, *181* (10), 6730–6737. https://doi.org/10.4049/jimmunol.181.10.6730.

(144) Tong, K. I.; Katoh, Y.; Kusunoki, H.; Itoh, K.; Tanaka, T.; Yamamoto, M. Keap1 Recruits Neh2 through Binding to ETGE and DLG Motifs: Characterization of the Two-Site Molecular Recognition Model. *Mol Cell Biol* **2006**, *26* (8), 2887–2900. https://doi.org/10.1128/MCB.26.8.2887-2900.2006.

(145) Baird, L.; Llères, D.; Swift, S.; Dinkova-Kostova, A. T. Regulatory Flexibility in the Nrf2-Mediated Stress Response Is Conferred by Conformational Cycling of the Keap1-Nrf2 Protein Complex. *Proc. Natl. Acad. Sci. U.S.A.* **2013**, *110* (38), 15259–15264. https://doi.org/10.1073/pnas.1305687110.

(146) Horie, Y.; Suzuki, T.; Inoue, J.; Iso, T.; Wells, G.; Moore, T. W.; Mizushima, T.; Dinkova-Kostova, A. T.; Kasai, T.; Kamei, T.; Koshiba, S.; Yamamoto, M. Molecular Basis for the Disruption of Keap1–Nrf2 Interaction via Hinge & Latch Mechanism. *Commun Biol* **2021**, *4* (1), 576. https://doi.org/10.1038/s42003-021-02100-6.

(147) Chen, J.; Feng, D.; Zhu, R.; Li, H.; Chen, L. Advances in KEAP1-Based PROTACs as Emerging Therapeutic Modalities: Structural Basis and Progress. *Redox Biology* **2025**, *85*, 103781. https://doi.org/10.1016/j.redox.2025.103781.

(148) Wakabayashi, N.; Dinkova-Kostova, A. T.; Holtzclaw, W. D.; Kang, M.-I.; Kobayashi, A.; Yamamoto, M.; Kensler, T. W.; Talalay, P. Protection against Electrophile and Oxidant Stress by Induction of the Phase 2 Response: Fate of Cysteines of the Keap1 Sensor Modified by Inducers. *Proc. Natl. Acad. Sci. U.S.A.* **2004**, *101* (7), 2040–2045. https://doi.org/10.1073/pnas.0307301101.

(149) Dinkova-Kostova, A. T.; Holtzclaw, W. D.; Cole, R. N.; Itoh, K.; Wakabayashi, N.; Katoh, Y.; Yamamoto, M.; Talalay, P. Direct Evidence That Sulfhydryl Groups of Keap1 Are the Sensors Regulating Induction of Phase 2 Enzymes That Protect against Carcinogens and Oxidants. *Proc. Natl. Acad. Sci. U.S.A.* **2002**, *99* (18), 11908–11913. https://doi.org/10.1073/pnas.172398899.

(150) Zhang, D. D.; Hannink, M. Distinct Cysteine Residues in Keap1 Are Required for Keap1-Dependent Ubiquitination of Nrf2 and for Stabilization of Nrf2 by Chemopreventive Agents and Oxidative Stress. *Molecular and Cellular Biology* **2003**, *23* (22), 8137–8151. https://doi.org/10.1128/MCB.23.22.8137-8151.2003.

(151) Hong, F.; Freeman, M. L.; Liebler, D. C. Identification of Sensor Cysteines in Human Keap1 Modified by the Cancer Chemopreventive Agent Sulforaphane. *Chem. Res. Toxicol.* **2005**, *18* (12), 1917–1926. https://doi.org/10.1021/tx0502138.

(152) Hong, F.; Sekhar, K. R.; Freeman, M. L.; Liebler, D. C. Specific Patterns of Electrophile Adduction Trigger Keap1 Ubiquitination and Nrf2 Activation. *Journal of Biological Chemistry* **2005**, *280* (36), 31768–31775. https://doi.org/10.1074/jbc.m503346200.

(153) Marino, S. M.; Gladyshev, V. N. Analysis and Functional Prediction of Reactive Cysteine Residues. *Journal of Biological Chemistry* **2012**, *287* (7), 4419–4425. https://doi.org/10.1074/jbc.r111.275578.

(154) Canning, P.; Cooper, C. D. O.; Krojer, T.; Murray, J. W.; Pike, A. C. W.; Chaikuad, A.; Keates, T.; Thangaratnarajah, C.; Hojzan, V.; Marsden, B. D.; Gileadi, O.; Knapp, S.; Von Delft, F.; Bullock, A. N. Structural Basis for Cul3 Protein Assembly with the BTB-Kelch Family of E3 Ubiquitin Ligases. *Journal of Biological Chemistry* **2013**, *288* (11), 7803–7814. https://doi.org/10.1074/jbc.m112.437996.

(155) Yamamoto, T.; Suzuki, T.; Kobayashi, A.; Wakabayashi, J.; Maher, J.; Motohashi, H.; Yamamoto, M. Physiological Significance of Reactive Cysteine Residues of Keap1 in Determining Nrf2 Activity. *Molecular and Cellular Biology* **2008**, *28* (8), 2758–2770. https://doi.org/10.1128/mcb.01704-07.

(156) Saito, R.; Suzuki, T.; Hiramoto, K.; Asami, S.; Naganuma, E.; Suda, H.; Iso, T.; Yamamoto, H.; Morita, M.; Baird, L.; Furusawa, Y.; Negishi, T.; Ichinose, M.; Yamamoto, M. Characterizations of Three Major Cysteine Sensors of Keap1 in Stress Response. *Molecular and Cellular Biology* **2016**, *36* (2), 271–284. https://doi.org/10.1128/MCB.00868-15.

(157) Sato, M.; Yaguchi, N.; Iijima, T.; Muramatsu, A.; Baird, L.; Suzuki, T.; Yamamoto, M. Sensor Systems of KEAP1 Uniquely Detecting Oxidative and Electrophilic Stresses Separately In Vivo. *Redox Biology* **2024**, *77*, 103355. https://doi.org/10.1016/j.redox.2024.103355.

(158) Katsuragi, Y.; Ichimura, Y.; Komatsu, M. Regulation of the Keap1–Nrf2 Pathway by P62/SQSTM1. *Current Opinion in Toxicology* **2016**, *1*, 54–61. https://doi.org/10.1016/j.cotox.2016.09.005.

(159) Cui, W.; Bai, Y.; Luo, P.; Miao, L.; Cai, L. Preventive and Therapeutic Effects of MG132 by Activating Nrf2-ARE Signaling Pathway on Oxidative Stress-Induced Cardiovascular and Renal Injury. *Oxidative Medicine and Cellular Longevity* **2013**, *2013*, 1–10. https://doi.org/10.1155/2013/306073.

(160) Cuadrado, A.; Kügler, S.; Lastres-Becker, I. Pharmacological Targeting of GSK-3 and NRF2 Provides Neuroprotection in a Preclinical Model of Tauopathy. *Redox Biology* **2018**, *14*, 522–534. https://doi.org/10.1016/j.redox.2017.10.010.

(161) Robledinos-Antón, N.; Fernández-Ginés, R.; Manda, G.; Cuadrado, A. Activators and Inhibitors of NRF2: A Review of Their Potential for Clinical Development. *Oxid Med Cell Longev* **2019**, *2019*, 9372182. https://doi.org/10.1155/2019/9372182.

(162) Amoroso, R.; Maccallini, C.; Bellezza, I. Activators of Nrf2 to Counteract Neurodegenerative Diseases. *Antioxidants* **2023**, *12* (3), 778. https://doi.org/10.3390/antiox12030778.

(163) Dayalan Naidu, S.; Dinkova-Kostova, A. T. KEAP1, a Cysteine-Based Sensor and a Drug Target for the Prevention and Treatment of Chronic Disease. *Open Biol.* **2020**, *10* (6). https://doi.org/10.1098/rsob.200105.

(164) Kansanen, E.; Bonacci, G.; Schopfer, F. J.; Kuosmanen, S. M.; Tong, K. I.; Leinonen, H.; Woodcock, S. R.; Yamamoto, M.; Carlberg, C.; Ylä-Herttuala, S.; Freeman, B. A.; Levonen, A.-L. Electrophilic Nitro-Fatty Acids Activate NRF2 by a KEAP1 Cysteine 151-

Independent Mechanism. *Journal of Biological Chemistry* **2011**, *286* (16), 14019–14027. https://doi.org/10.1074/jbc.m110.190710.

(165) Salvatore, S. R.; Vitturi, D. A.; Fazzari, M.; Jorkasky, D. K.; Schopfer, F. J. Evaluation of 10-Nitro Oleic Acid Bio-Elimination in Rats and Humans. *Sci Rep* **2017**, *7* (1), 39900. https://doi.org/10.1038/srep39900.

(166) Liu, H.; Jia, Z.; Soodvilai, S.; Guan, G.; Wang, M.-H.; Dong, Z.; Symons, J. D.; Yang, T. Nitro-Oleic Acid Protects the Mouse Kidney from Ischemia and Reperfusion Injury. *American Journal of Physiology-Renal Physiology* **2008**, *295* (4), F942–F949. https://doi.org/10.1152/ajprenal.90236.2008.

(167) Garner, R. M.; Mould, D. R.; Chieffo, C.; Jorkasky, D. K. Pharmacokinetic and Pharmacodynamic Effects of Oral CXA -10, a Nitro Fatty Acid, After Single and Multiple Ascending Doses in Healthy and Obese Subjects. *Clinical Translational Sci* **2019**, *12* (6), 667–676. https://doi.org/10.1111/cts.12672.

(168) Bresciani, G.; Manai, F.; Davinelli, S.; Tucci, P.; Saso, L.; Amadio, M. Novel Potential Pharmacological Applications of Dimethyl Fumarate—an Overview and Update. *Front. Pharmacol.* **2023**, *14*, 1264842. https://doi.org/10.3389/fphar.2023.1264842.

(169) Wang, Y.; Bhargava, P. Diroximel Fumarate to Treat Multiple Sclerosis. *Drugs of Today* **2020**, *56* (7), 431. https://doi.org/10.1358/dot.2020.56.7.3151521.

(170) Berger, A. A.; Sottosanti, E. R.; Winnick, A.; Izygon, J.; Berardino, K.; Cornett, E. M.; Kaye, A. D.; Varrassi, G.; Viswanath, O.; Urits, I. Monomethyl Fumarate (MMF, Bafiertam) for the Treatment of Relapsing Forms of Multiple Sclerosis (MS). *Neurology International* **2021**, *13* (2), 207–223. https://doi.org/10.3390/neurolint13020022.

(171) Egbujor, M. C.; Buttari, B.; Profumo, E.; Telkoparan-Akillilar, P.; Saso, L. An Overview of NRF2-Activating Compounds Bearing α,β-Unsaturated Moiety and Their Antioxidant Effects. *IJMS* **2022**, *23* (15), 8466. https://doi.org/10.3390/ijms23158466.

(172) Wundes, A.; Wray, S.; Gold, R.; Singer, B. A.; Jasinska, E.; Ziemssen, T.; De Seze, J.; Repovic, P.; Chen, H.; Hanna, J.; Messer, J.; Miller, C.; Naismith, R. T. Improved Gastrointestinal Profile with Diroximel Fumarate Is Associated with a Positive Impact on Quality of Life Compared with Dimethyl Fumarate: Results from the Randomized, Double-Blind, Phase III EVOLVE-MS-2 Study. *Ther Adv Neurol Disord* **2021**, *14*, 1756286421993999. https://doi.org/10.1177/1756286421993999.

(173) Merchant, H. J.; Forteath, C.; Gallagher, J. R.; Dinkova-Kostova, A. T.; Ashford, M. L. J.; McCrimmon, R. J.; McNeilly, A. D. Activation of the Nrf2 Pathway by Sulforaphane Improves Hypoglycaemia-Induced Cognitive Impairment in a Rodent Model of Type 1 Diabetes. *Antioxidants* **2025**, *14* (3), 308. https://doi.org/10.3390/antiox14030308.

(174) Zhou, Z.; Dong, J.; Qiu, Y.; Zhang, G.; Wei, K.; He, L.; Sun, Y.; Jiang, H.; Zhang, S.; Guo, X.; Wang, J.; Chen, D. Sulforaphane Decreases Oxidative Stress and Inhibits NLRP3 Inflammasome Activation in a Mouse Model of Ulcerative Colitis. *Biomedicine & Pharmacotherapy* **2024**, *175*, 116706. https://doi.org/10.1016/j.biopha.2024.116706.

(175) Bai, B.; Tu, P.; Weng, J.; Zhang, Y.; Lin, Q.; Muskat, M. N.; Wang, J.; Tang, X.; Cheng, X. Identification of Food-Derived Electrophilic Chalcones as Nrf2 Activators Using Comprehensive Virtual Screening Techniques. *Antioxidants* **2025**, *14* (5), 546. https://doi.org/10.3390/antiox14050546.

(176) Cascajosa-Lira, A.; Prieto, A. I.; Pichardo, S.; Jos, A.; Cameán, A. M. Protective Effects of Sulforaphane against Toxic Substances and Contaminants: A Systematic Review. *Phytomedicine* **2024**, *130*, 155731. https://doi.org/10.1016/j.phymed.2024.155731.

(177) Yuan, J.-M.; Kensler, T. W.; Dacic, S.; Hartman, D. J.; Wang, R.; Balogh, P. A.; Sufka, P.; Turner, M. A.; Fuhrer, K.; Seigh, L.; Pham, Y. T.-H.; Adams-Haduch, J.; Valacchi, G.; Singh, S. V.; Herman, J. G.; Wilson, D. O. Randomized Phase II Clinical Trial of Sulforaphane in Former Smokers at High Risk for Lung Cancer. *Cancer Prevention Research* **2025**, *18* (6), 335–345. https://doi.org/10.1158/1940-6207.CAPR-24-0386.

(178) Dello Russo, C.; Scott, K. A.; Pirmohamed, M. Dimethyl Fumarate Induced Lymphopenia in Multiple Sclerosis: A Review of the Literature. *Pharmacology & Therapeutics* **2021**, *219*, 107710. https://doi.org/10.1016/j.pharmthera.2020.107710.

(179) Vinogradova, E. V.; Zhang, X.; Remillard, D.; Lazar, D. C.; Suciu, R. M.; Wang, Y.; Bianco, G.; Yamashita, Y.; Crowley, V. M.; Schafroth, M. A.; Yokoyama, M.; Konrad, D. B.; Lum, K. M.; Simon, G. M.; Kemper, E. K.; Lazear, M. R.; Yin, S.; Blewett, M. M.; Dix, M. M.; Nguyen, N.; Shokhirev, M. N.; Chin, E. N.; Lairson, L. L.; Melillo, B.; Schreiber, S. L.; Forli, S.; Teijaro, J. R.; Cravatt, B. F. An Activity-Guided Map of Electrophile-Cysteine Interactions in Primary Human T Cells. *Cell* **2020**, *182* (4), 1009-1026.e29. https://doi.org/10.1016/j.cell.2020.07.001.

(180) Gunther, K.; Profeta, V.; Keita, M.; Park, C.; Wells, M.; Sharma, S.; Schadt, K.; Lynch, D. R. Safety Monitoring of Omaveloxolone in Friedreich Ataxia: Results from One Year of Clinical Treatment. *Neurol Ther* **2025**, *14* (3), 1105–1114. https://doi.org/10.1007/s40120-025-00749-3.

(181) Hancock, R.; Bertrand, H. C.; Tsujita, T.; Naz, S.; El-Bakry, A.; Laoruchupong, J.; Hayes, J. D.; Wells, G. Peptide Inhibitors of the Keap1–Nrf2 Protein–Protein Interaction. *Free Radical Biology and Medicine* **2012**, *52* (2), 444–451. https://doi.org/10.1016/j.freeradbiomed.2011.10.486.

(182) Inoyama, D.; Chen, Y.; Huang, X.; Beamer, L. J.; Kong, A.-N. T.; Hu, L. Optimization of Fluorescently Labeled Nrf2 Peptide Probes and the Development of a Fluorescence Polarization Assay for the Discovery of Inhibitors of Keap1-Nrf2 Interaction. *SLAS Discovery* **2012**, *17* (4), 435–447. https://doi.org/10.1177/1087057111430124.

(183) Chen, K.; Huang, L.; Shen, B. Rational Cyclization-Based Minimization of Entropy Penalty upon the Binding of Nrf2-Derived Linear Peptides to Keap1: A New Strategy to Improve Therapeutic Peptide Activity against Sepsis. *Biophysical Chemistry* **2019**, *244*, 22–28. https://doi.org/10.1016/j.bpc.2018.11.002.

(184) Lu, M.-C.; Jiao, Q.; Liu, T.; Tan, S.-J.; Zhou, H.-S.; You, Q.-D.; Jiang, Z.-Y. Discovery of a Head-to-Tail Cyclic Peptide as the Keap1-Nrf2 Protein-Protein Interaction Inhibitor with High Cell Potency. *European Journal of Medicinal Chemistry* **2018**, *143*, 1578–1589. https://doi.org/10.1016/j.ejmech.2017.10.052.

(185) Salim, H.; Song, J.; Sahni, A.; Pei, D. Development of a Cell-Permeable Cyclic Peptidyl Inhibitor against the Keap1–Nrf2 Interaction. *J. Org. Chem.* **2020**, *85* (3), 1416–1424. https://doi.org/10.1021/acs.joc.9b02367.

(186) Steel, R.; Cowan, J.; Payerne, E.; O'Connell, M. A.; Searcey, M. Anti-Inflammatory Effect of a Cell-Penetrating Peptide Targeting the Nrf2/Keap1 Interaction. *ACS Med. Chem. Lett.* **2012**, *3* (5), 407–410. https://doi.org/10.1021/ml300041g.

(187) Jiang, Z.-Y.; Xu, L.; Lu, M.-C.; Chen, Z.-Y.; Yuan, Z.-W.; Xu, X.-L.; Guo, X.-K.; Zhang, X.-J.; Sun, H.-P.; You, Q.-D. Structure–Activity and Structure–Property Relationship and Exploratory in Vivo Evaluation of the Nanomolar Keap1–Nrf2 Protein–Protein Interaction Inhibitor. *J. Med. Chem.* **2015**, *58* (16), 6410–6421. https://doi.org/10.1021/acs.jmedchem.5b00185.

(188) Lu, M.-C.; Zhao, J.; Liu, Y.-T.; Liu, T.; Tao, M.-M.; You, Q.-D.; Jiang, Z.-Y. CPUY192018, a Potent Inhibitor of the Keap1-Nrf2 Protein-Protein Interaction, Alleviates Renal Inflammation in Mice by Restricting Oxidative Stress and NF-κB Activation. *Redox Biology* **2019**, *26*, 101266. https://doi.org/10.1016/j.redox.2019.101266.

(189) Lu, M.-C.; Ji, J.-A.; Jiang, Y.-L.; Chen, Z.-Y.; Yuan, Z.-W.; You, Q.-D.; Jiang, Z.-Y. An Inhibitor of the Keap1-Nrf2 Protein-Protein Interaction Protects NCM460 Colonic Cells and Alleviates Experimental Colitis. *Sci Rep* **2016**, *6* (1). https://doi.org/10.1038/srep26585.

(190) Jiang, C.-S.; Zhuang, C.-L.; Zhu, K.; Zhang, J.; Muehlmann, L. A.; Figueiró Longo, J. P.; Azevedo, R. B.; Zhang, W.; Meng, N.; Zhang, H. Identification of a Novel Small-Molecule Keap1–Nrf2 PPI Inhibitor with Cytoprotective Effects on LPS-Induced Cardiomyopathy. *Journal of Enzyme Inhibition and Medicinal Chemistry* **2018**, *33* (1), 833–841. https://doi.org/10.1080/14756366.2018.1461856.

(191) Aparici, M.; Bravo, M.; Calama, E.; García-González, V.; Domènech, T.; Córdoba, M.; Roger, I.; Cortijo, J.; Góngora-Benítez, M.; Paradís-Bas, M.; Collins, B.; Davis, A. M.; Albericio, F.; Puig, C. Pharmacological Characterization of a Novel Peptide Inhibitor of

the Keap1-Nrf2 Protein-Protein Interaction. *Biochemical Pharmacology* **2022**, *204*, 115226. https://doi.org/10.1016/j.bcp.2022.115226.

(192) Sakamoto, K. M.; Kim, K. B.; Kumagai, A.; Mercurio, F.; Crews, C. M.; Deshaies, R. J. Protacs: Chimeric Molecules That Target Proteins to the Skp1–Cullin–F Box Complex for Ubiquitination and Degradation. *Proc. Natl. Acad. Sci. U.S.A.* **2001**, *98* (15), 8554–8559. https://doi.org/10.1073/pnas.141230798.

(193) Wang, Y.; Jiang, X.; Feng, F.; Liu, W.; Sun, H. Degradation of Proteins by PROTACs and Other Strategies. *Acta Pharmaceutica Sinica B* **2020**, *10* (2), 207–238. https://doi.org/10.1016/j.apsb.2019.08.001.

(194) Ciechanover, A. The Ubiquitin-Proteasome Proteolytic Pathway. *Cell* **1994**, *79* (1), 13–21. https://doi.org/10.1016/0092-8674(94)90396-4.

(195) Haas, A. L.; Warms, J. V.; Hershko, A.; Rose, I. A. Ubiquitin-Activating Enzyme. Mechanism and Role in Protein-Ubiquitin Conjugation. *J Biol Chem* **1982**, *257* (5), 2543–2548.

(196) Hershko, A.; Heller, H.; Elias, S.; Ciechanover, A. Components of Ubiquitin-Protein Ligase System. Resolution, Affinity Purification, and Role in Protein Breakdown. *J Biol Chem* **1983**, *258* (13), 8206–8214.

(197) Scheffner, M.; Nuber, U.; Huibregtse, J. M. Protein Ubiquitination Involving an E1–E2–E3 Enzyme Ubiquitin Thioester Cascade. *Nature* **1995**, *373* (6509), 81–83. https://doi.org/10.1038/373081a0.

(198) Thrower, J. S. Recognition of the Polyubiquitin Proteolytic Signal. *The EMBO Journal* **2000**, *19* (1), 94–102. https://doi.org/10.1093/emboj/19.1.94.

(199) Baumeister, W.; Walz, J.; Zühl, F.; Seemüller, E. The Proteasome: Paradigm of a Self-Compartmentalizing Protease. *Cell* **1998**, *92* (3), 367–380. https://doi.org/10.1016/S0092-8674(00)80929-0.

(200) Vlasschaert, C.; Cook, D.; Xia, X.; Gray, D. A. The Evolution and Functional Diversification of the Deubiquitinating Enzyme Superfamily. *Genome Biology and Evolution* **2017**, *9* (3), 558–573. https://doi.org/10.1093/gbe/evx020.

(201) Min, J.-H.; Yang, H.; Ivan, M.; Gertler, F.; Kaelin, W. G.; Pavletich, N. P. Structure of an HIF-1α-pVHL Complex: Hydroxyproline Recognition in Signaling. *Science* **2002**, *296* (5574), 1886–1889. https://doi.org/10.1126/science.1073440.

(202) Galdeano, C.; Gadd, M. S.; Soares, P.; Scaffidi, S.; Van Molle, I.; Birced, I.; Hewitt, S.; Dias, D. M.; Ciulli, A. Structure-Guided Design and Optimization of Small Molecules Targeting the Protein–Protein Interaction between the von Hippel–Lindau (VHL) E3 Ubiquitin Ligase and the Hypoxia Inducible Factor (HIF) Alpha Subunit with in Vitro Nanomolar Affinities. *J. Med. Chem.* **2014**, *57* (20), 8657–8663. https://doi.org/10.1021/jm5011258.

(203) Frost, J.; Galdeano, C.; Soares, P.; Gadd, M. S.; Grzes, K. M.; Ellis, L.; Epemolu, O.; Shimamura, S.; Bantscheff, M.; Grandi, P.; Read, K. D.; Cantrell, D. A.; Rocha, S.; Ciulli, A. Potent and Selective Chemical Probe of Hypoxic Signalling Downstream of HIF-α Hydroxylation via VHL Inhibition. *Nat Commun* **2016**, *7* (1). https://doi.org/10.1038/ncomms13312.

(204) Gadd, M. S.; Testa, A.; Lucas, X.; Chan, K.-H.; Chen, W.; Lamont, D. J.; Zengerle, M.; Ciulli, A. Structural Basis of PROTAC Cooperative Recognition for Selective Protein Degradation. *Nat Chem Biol* **2017**, *13* (5), 514–521. https://doi.org/10.1038/nchembio.2329.

(205) Li, G.; Ma, L.; Feng, C.; Yin, H.; Bao, J.; Wu, D.; Zhang, Z.; Li, X.; Li, Z.; Yang, C.; Wang, H.; Fang, F.; Hu, X.; Li, M.; Xu, L.; Xu, Y.; Liang, H.; Yang, T.; Wang, J.; Pan, J. MZ1, a BRD4 Inhibitor, Exerted Its Anti-Cancer Effects by Suppressing SDC1 in Glioblastoma. *BMC Cancer* **2024**, *24* (1). https://doi.org/10.1186/s12885-024-11966-8.

(206) Li, C.; Chen, Y.; Huang, W.; Qiu, Y.; Huang, S.; Zhou, Y.; Zhou, F.; Xu, J.; Ren, X.; Zhang, J.; Wang, Z.; Ding, M.; Ding, K. Structure-Based Design of “Head-to-Tail” Macrocyclic PROTACs. *JACS Au* **2024**, *4* (12), 4866–4882. https://doi.org/10.1021/jacsau.4c00831.

(207) Raina, K.; Lu, J.; Qian, Y.; Altieri, M.; Gordon, D.; Rossi, A. M. K.; Wang, J.; Chen, X.; Dong, H.; Siu, K.; Winkler, J. D.; Crew, A. P.; Crews, C. M.; Coleman, K. G. PROTAC-Induced BET Protein Degradation as a Therapy for Castration-Resistant Prostate Cancer. *Proc. Natl. Acad. Sci. U.S.A.* **2016**, *113* (26), 7124–7129. https://doi.org/10.1073/pnas.1521738113.

(208) Gandhi, L.; Camidge, D. R.; Ribeiro De Oliveira, M.; Bonomi, P.; Gandara, D.; Khaira, D.; Hann, C. L.; McKeegan, E. M.; Litvinovich, E.; Hemken, P. M.; Dive, C.; Enschede, S. H.; Nolan, C.; Chiu, Y.-L.; Busman, T.; Xiong, H.; Krivoshik, A. P.; Humerickhouse, R.; Shapiro, G. I.; Rudin, C. M. Phase I Study of Navitoclax (ABT-263), a Novel Bcl-2 Family Inhibitor, in Patients With Small-Cell Lung Cancer and Other Solid Tumors. *JCO* **2011**, *29* (7), 909–916. https://doi.org/10.1200/jco.2010.31.6208.

(209) Khan, S.; Zhang, X.; Lv, D.; Zhang, Q.; He, Y.; Zhang, P.; Liu, X.; Thummuri, D.; Yuan, Y.; Wiegand, J. S.; Pei, J.; Zhang, W.; Sharma, A.; McCurdy, C. R.; Kuruvilla, V. M.; Baran, N.; Ferrando, A. A.; Kim, Y.; Rogojina, A.; Houghton, P. J.; Huang, G.; Hromas, R.; Konopleva, M.; Zheng, G.; Zhou, D. A Selective BCL-XL PROTAC Degrader Achieves Safe and Potent Antitumor Activity. *Nat Med* **2019**, *25* (12), 1938–1947. https://doi.org/10.1038/s41591-019-0668-z.

(210) He, Y.; Koch, R.; Budamagunta, V.; Zhang, P.; Zhang, X.; Khan, S.; Thummuri, D.; Ortiz, Y. T.; Zhang, X.; Lv, D.; Wiegand, J. S.; Li, W.; Palmer, A. C.; Zheng, G.; Weinstock, D. M.; Zhou, D. DT2216—a Bcl-xL-Specific Degrader Is Highly Active against Bcl-xL-Dependent T Cell Lymphomas. *J Hematol Oncol* **2020**, *13* (1). https://doi.org/10.1186/s13045-020-00928-9.

(211) Mahadevan, D.; Barve, M.; Mahalingam, D.; Parekh, J.; Kurman, M.; Strauss, J.; Tremaine, L.; Hromas, R.; Sills, J.; McCulloch, J.; Harkey, J.; Suberg, S.; Zimmerman, L.; Zheng, G.; Zhou, D. Abstract CT063: First in Human Phase 1 Study of DT2216, a Selective BCL-xL Degrader, in Patients with Relapsed/Refractory Solid Malignancies (NCT04886622). *Cancer Research* **2025**, *85* (8_Supplement_2), CT063–CT063. https://doi.org/10.1158/1538-7445.am2025-ct063.

(212) Siveen, K. S.; Sikka, S.; Surana, R.; Dai, X.; Zhang, J.; Kumar, A. P.; Tan, B. K. H.; Sethi, G.; Bishayee, A. Targeting the STAT3 Signaling Pathway in Cancer: Role of Synthetic and Natural Inhibitors. *Biochimica et Biophysica Acta (BBA) - Reviews on Cancer* **2014**, *1845* (2), 136–154. https://doi.org/10.1016/j.bbcan.2013.12.005.

(213) Feldman, T.; Marchi, E.; Smith, S. D.; Olszewski, A. J.; Huen, A. O.; Epstein-Peterson, Z. D.; Stevens, D. A.; Starodub, A. N.; Feldman, E. J.; Rodriguez, C. P.; Reneau, J. C.; Brammer, J. E.; Mattour, A. H.; Pinter-Brown, L. C.; Perea, R.; Henrick, P.; Dey, J.; Fasciano, A.; Karnik, R.; Agarwal, S.; Gollerkeri, A.; Gollob, J.; Shastri, A.; Barta, S. K. Safety, Pharmacokinetics, Pharmacodynamics and Clinical Activity of KT-333, a Targeted Protein Degrader of STAT3, in Patients with Relapsed or Refractory Lymphomas, Leukemia, and Solid Tumors. *Blood* **2024**, *144* (Supplement 1), 4433–4433. https://doi.org/10.1182/blood-2024-210301.

(214) Hamilton, E. P.; Ma, C.; De Laurentiis, M.; Iwata, H.; Hurvitz, S. A.; Wander, S. A.; Danso, M.; Lu, D. R.; Perkins Smith, J.; Liu, Y.; Tran, L.; Anderson, S.; Campone, M. VERITAC-2: A Phase III Study of Vepdegestrant, a PROTAC ER Degrader, versus Fulvestrant in ER+/HER2- Advanced Breast Cancer. *Future Oncology* **2024**, *20* (32), 2447–2455. https://doi.org/10.1080/14796694.2024.2377530.

(215) Kroupova, A.; Spiteri, V. A.; Rutter, Z. J.; Furihata, H.; Darren, D.; Ramachandran, S.; Chakraborti, S.; Haubrich, K.; Pethe, J.; Gonzales, D.; Wijaya, A. J.; Rodriguez-Rios, M.; Sturbaut, M.; Lynch, D. M.; Farnaby, W.; Nakasone, M. A.; Zollman, D.; Ciulli, A. Design of a Cereblon Construct for Crystallographic and Biophysical Studies of Protein Degraders. *Nat Commun* **2024**, *15* (1). https://doi.org/10.1038/s41467-024-52871-9.

(216) Snyder, L. B.; Neklesa, T. K.; Willard, R. R.; Gordon, D. A.; Pizzano, J.; Vitale, N.; Robling, K.; Dorso, M. A.; Moghrabi, W.; Landrette, S.; Gedrich, R.; Lee, S. H.; Taylor, I. C. A.; Houston, J. G. Preclinical Evaluation of Bavdegalutamide (ARV-110), a Novel PROteolysis TArgeting Chimera Androgen Receptor Degrader. *Molecular Cancer Therapeutics* **2025**, *24* (4), 511–522. https://doi.org/10.1158/1535-7163.mct-23-0655.

(217) Gao, X.; Burris Iii, H. A.; Vuky, J.; Dreicer, R.; Sartor, A. O.; Sternberg, C. N.; Percent, I. J.; Hussain, M. H. A.; Rezazadeh Kalebasty, A.; Shen, J.; Heath, E. I.; Abesada-Terk, G.; Gandhi, S. G.; McKean, M.; Lu, H.; Berghorn, E.; Gedrich, R.; Chirnomas, S. D.; Vogelzang, N. J.; Petrylak, D. P. Phase 1/2 Study of ARV-110, an Androgen Receptor (AR) PROTAC Degrader, in Metastatic Castration-Resistant Prostate Cancer (mCRPC). *JCO* **2022**, *40* (6_suppl), 17–17. https://doi.org/10.1200/jco.2022.40.6_suppl.017.

(218) Seymour, J. F.; Cheah, C. Y.; Parrondo, R.; Thompson, M. C.; Stevens, D. A.; Lasica, M.; Wang, M. L.; Kumar, A.; Trotman, J.; Alwan, M.; Ding, W.; By, K.; Tariq, B.; Chen, X.; Fabre, S.; Paik, J.; Agarwal, A.; Tam, C. S. First Results from a Phase 1, First-in-Human Study of the Bruton's Tyrosine Kinase (BTK) Degrader Bgb-16673 in Patients (Pts) with Relapsed or Refractory (R/R) B-Cell Malignancies (BGB-16673-101). *Blood* **2023**, *142* (Supplement 1), 4401–4401. https://doi.org/10.1182/blood-2023-180109.

(219) Bondeson, D. P.; Mares, A.; Smith, I. E. D.; Ko, E.; Campos, S.; Miah, A. H.; Mulholland, K. E.; Routly, N.; Buckley, D. L.; Gustafson, J. L.; Zinn, N.; Grandi, P.; Shimamura, S.; Bergamini, G.; Faelth-Savitski, M.; Bantscheff, M.; Cox, C.; Gordon, D. A.; Willard, R. R.; Flanagan, J. J.; Casillas, L. N.; Votta, B. J.; Den Besten, W.; Famm, K.; Kruidenier, L.; Carter, P. S.; Harling, J. D.; Churcher, I.; Crews, C. M. Catalytic in Vivo Protein Knockdown by Small-Molecule PROTACs. *Nat Chem Biol* **2015**, *11* (8), 611–617. https://doi.org/10.1038/nchembio.1858.

(220) Winter, G. E.; Buckley, D. L.; Paulk, J.; Roberts, J. M.; Souza, A.; Dhe-Paganon, S.; Bradner, J. E. Phthalimide Conjugation as a Strategy for in Vivo Target Protein Degradation. *Science* **2015**, *348* (6241), 1376–1381. https://doi.org/10.1126/science.aab1433.

(221) Bai, L.; Zhou, H.; Xu, R.; Zhao, Y.; Chinnaswamy, K.; McEachern, D.; Chen, J.; Yang, C.-Y.; Liu, Z.; Wang, M.; Liu, L.; Jiang, H.; Wen, B.; Kumar, P.; Meagher, J. L.; Sun, D.; Stuckey, J. A.; Wang, S. A Potent and Selective Small-Molecule Degrader of STAT3 Achieves Complete Tumor Regression In Vivo. *Cancer Cell* **2019**, *36* (5), 498-511.e17. https://doi.org/10.1016/j.ccell.2019.10.002.

(222) Zhang, Y.; Ming, A.; Wang, J.; Chen, W.; Fang, Z. PROTACs Targeting Androgen Receptor Signaling: Potential Therapeutic Agents for Castration-Resistant Prostate Cancer. *Pharmacological Research* **2024**, *205*, 107234. https://doi.org/10.1016/j.phrs.2024.107234.

(223) Gough, S. M.; Flanagan, J. J.; Teh, J.; Andreoli, M.; Rousseau, E.; Pannone, M.; Bookbinder, M.; Willard, R.; Davenport, K.; Bortolon, E.; Cadelina, G.; Gordon, D.; Pizzano, J.; Macaluso, J.; Soto, L.; Corradi, J.; Digianantonio, K.; Drulyte, I.; Morgan, A.; Quinn, C.; Békés, M.; Ferraro, C.; Chen, X.; Wang, G.; Dong, H.; Wang, J.; Langley, D. R.; Houston, J.; Gedrich, R.; Taylor, I. C. Oral Estrogen Receptor PROTAC Vepdegestrant (ARV-471) Is Highly Efficacious as Monotherapy and in Combination with CDK4/6 or PI3K/mTOR Pathway Inhibitors in Preclinical ER+ Breast Cancer Models. *Clinical Cancer Research* **2024**, *30* (16), 3549–3563. https://doi.org/10.1158/1078-0432.ccr-23-3465.

(224) Zengerle, M.; Chan, K.-H.; Ciulli, A. Selective Small Molecule Induced Degradation of the BET Bromodomain Protein BRD4. *ACS Chem. Biol.* **2015**, *10* (8), 1770–1777. https://doi.org/10.1021/acschembio.5b00216.

(225) Lin, Y.; Liu, J.; Tian, X.; Wang, J.; Su, H.; Xiang, J.; Cao, T.; Wang, Y.; Xie, Q.; Yu, X. Design, Synthesis, and Biological Evaluation of Novel BTK-Targeting Proteolysis Targeting Chimeras (PROTACs) with Enhanced Pharmacokinetic Properties. *European Journal of Medicinal Chemistry* **2025**, *289*, 117420. https://doi.org/10.1016/j.ejmech.2025.117420.

(226) Sobierajski, T.; Małolepsza, J.; Pichlak, M.; Gendaszewska-Darmach, E.; Błażewska, K. M. The Impact of E3 Ligase Choice on PROTAC Effectiveness in Protein Kinase Degradation. *Drug Discovery Today* **2024**, *29* (7), 104032. https://doi.org/10.1016/j.drudis.2024.104032.

(227) Syahputra, E. W.; Lee, H.; Cho, H.; Park, H. J.; Park, K.-S.; Hwang, D. PROTAC Delivery Strategies for Overcoming Physicochemical Properties and Physiological

Barriers in Targeted Protein Degradation. *Pharmaceutics* **2025**, *17* (4), 501. https://doi.org/10.3390/pharmaceutics17040501.

(228) Poongavanam, V.; Atilaw, Y.; Siegel, S.; Giese, A.; Lehmann, L.; Meibom, D.; Erdelyi, M.; Kihlberg, J. Linker-Dependent Folding Rationalizes PROTAC Cell Permeability. *J. Med. Chem.* **2022**, *65* (19), 13029–13040. https://doi.org/10.1021/acs.jmedchem.2c00877.

(229) Chen, J.; Qiu, M.; Ma, F.; Yang, L.; Glass, Z.; Xu, Q. Enhanced Protein Degradation by Intracellular Delivery of Pre-Fused PROTACs Using Lipid-like Nanoparticles. *Journal of Controlled Release* **2021**, *330*, 1244–1249. https://doi.org/10.1016/j.jconrel.2020.11.032.

(230) Wang, F.; Zhan, Y.; Li, M.; Wang, L.; Zheng, A.; Liu, C.; Wang, H.; Wang, T. Cell-Permeable PROTAC Degraders against KEAP1 Efficiently Suppress Hepatic Stellate Cell Activation through the Antioxidant and Anti-Inflammatory Pathway. *ACS Pharmacol. Transl. Sci.* **2023**, *6* (1), 76–87. https://doi.org/10.1021/acsptsci.2c00165.

(231) Davies, T. G.; Wixted, W. E.; Coyle, J. E.; Griffiths-Jones, C.; Hearn, K.; McMenamin, R.; Norton, D.; Rich, S. J.; Richardson, C.; Saxty, G.; Willems, H. M. G.; Woolford, A. J.-A.; Cottom, J. E.; Kou, J.-P.; Yonchuk, J. G.; Feldser, H. G.; Sanchez, Y.; Foley, J. P.; Bolognese, B. J.; Logan, G.; Podolin, P. L.; Yan, H.; Callahan, J. F.; Heightman, T. D.; Kerns, J. K. Monoacidic Inhibitors of the Kelch-like ECH-Associated Protein 1: Nuclear Factor Erythroid 2-Related Factor 2 (KEAP1:NRF2) Protein–Protein Interaction with High Cell Potency Identified by Fragment-Based Discovery. *J. Med. Chem.* **2016**, *59* (8), 3991–4006. https://doi.org/10.1021/acs.jmedchem.6b00228.

(232) Park, S. Y.; Gurung, R.; Hwang, J. H.; Kang, J.-H.; Jung, H. J.; Zeb, A.; Hwang, J.-I.; Park, S. J.; Maeng, H.-J.; Shin, D.; Oh, S. H. Development of KEAP1-Targeting PROTAC and Its Antioxidant Properties: In Vitro and in Vivo. *Redox Biology* **2023**, *64*, 102783. https://doi.org/10.1016/j.redox.2023.102783.

(233) Chen, H.; Nguyen, N. H.; Magtoto, C. M.; Cobbold, S. A.; Bidgood, G. M.; Meza Guzman, L. G.; Richardson, L. W.; Corbin, J.; Au, A. E.; Lechtenberg, B. C.; Feltham, R.; Sutherland, K. D.; Grohmann, C.; Nicholson, S. E.; Sleebs, B. E. Design and Characterization of a Heterobifunctional Degrader of KEAP1. *Redox Biology* **2023**, *59*, 102552. https://doi.org/10.1016/j.redox.2022.102552.

(234) Bricelj, A.; Dora Ng, Y. L.; Ferber, D.; Kuchta, R.; Müller, S.; Monschke, M.; Wagner, K. G.; Krönke, J.; Sosič, I.; Gütschow, M.; Steinebach, C. Influence of Linker Attachment Points on the Stability and Neosubstrate Degradation of Cereblon Ligands. *ACS Med. Chem. Lett.* **2021**, *12* (11), 1733–1738. https://doi.org/10.1021/acsmedchemlett.1c00368.

(235) Ma, J.; Mi, C.; Wang, K. S.; Lee, J. J.; Jin, X. Zinc Finger Protein 91 (ZFP91) Activates HIF-1α *via* NF-κB/P65 to Promote Proliferation and Tumorigenesis of Colon Cancer. *Oncotarget* **2016**, *7* (24), 36551–36562. https://doi.org/10.18632/oncotarget.9070.

(236) Qi, J.-L.; He, J.-R.; Liu, C.-B.; Jin, S.-M.; Yang, X.; Bai, H.-M.; Ma, Y.-B. SQSTM1/P62 Regulate Breast Cancer Progression and Metastasis by Inducing Cell Cycle Arrest and Regulating Immune Cell Infiltration. *Genes & Diseases* **2022**, *9* (5), 1332–1344. https://doi.org/10.1016/j.gendis.2021.03.008.

(237) Yan, W.; Pan, B.-S.; Shao, J.; Lin, H.; Li, H. Feasible Column Chromatography-Free, Multi-Gram Scale Synthetic Process of VH032 Amine, Which Could Enable Rapid PROTAC Library Construction. *ACS Omega* **2022**, *7* (30), 26015–26021. https://doi.org/10.1021/acsomega.2c00245.

(238) Dinkova-Kostova, A. T.; Copple, I. M. Advances and Challenges in Therapeutic Targeting of NRF2. *Trends in Pharmacological Sciences* **2023**, *44* (3), 137–149. https://doi.org/10.1016/j.tips.2022.12.003.

(239) Ziegler, A.; Nervi, P.; Dürrenberger, M.; Seelig, J. The Cationic Cell-Penetrating Peptide CPP^{TAT} Derived from the HIV-1 Protein TAT Is Rapidly Transported into Living Fibroblasts: Optical, Biophysical, and Metabolic Evidence. *Biochemistry* **2005**, *44* (1), 138–148. https://doi.org/10.1021/bi0491604.

(240) Jones, S. W.; Christison, R.; Bundell, K.; Voyce, C. J.; Brockbank, S. M. V.; Newham, P.; Lindsay, M. A. Characterisation of Cell-penetrating Peptide-mediated Peptide Delivery. *British J Pharmacology* **2005**, *145* (8), 1093–1102. https://doi.org/10.1038/sj.bjp.0706279.

(241) Gori, A.; Lodigiani, G.; Colombarolli, S. G.; Bergamaschi, G.; Vitali, A. Cell Penetrating Peptides: Classification, Mechanisms, Methods of Study, and Applications. *ChemMedChem* **2023**, *18* (17), e202300236. https://doi.org/10.1002/cmdc.202300236.

(242) Cowan, J. Targeting Nrf2 in Inflammation and Cancer. Ph.D. Thesis, The University of East Anglia, Norwich, 2015. https://ueaeprints.uea.ac.uk/id/eprint/53467 (accessed 2025-07-06).

(243) Chanput, W.; Mes, J. J.; Wichers, H. J. THP-1 Cell Line: An in Vitro Cell Model for Immune Modulation Approach. *International Immunopharmacology* **2014**, *23* (1), 37–45. https://doi.org/10.1016/j.intimp.2014.08.002.

(244) Hu, H.; Cai, Y.; Shi, Y.; Zhang, S.; Yu, X.; Ma, T.; Liao, S. Dimethyl Fumarate Covalently Modifies Cys673 of NLRP3 to Exert Anti-Inflammatory Effects. *iScience* **2024**, *27* (4), 109544. https://doi.org/10.1016/j.isci.2024.109544.

(245) Manai, F.; Amadio, M. Dimethyl Fumarate Triggers the Antioxidant Defense System in Human Retinal Endothelial Cells through Nrf2 Activation. *Antioxidants* **2022**, *11* (10), 1924. https://doi.org/10.3390/antiox11101924.

(246) Qi, D.; Chen, P.; Bao, H.; Zhang, L.; Sun, K.; Song, S.; Li, T. Dimethyl Fumarate Protects against Hepatic Ischemia-Reperfusion Injury by Alleviating Ferroptosis via the NRF2/SLC7A11/HO-1 Axis. *Cell Cycle* **2023**, *22* (7), 818–828. https://doi.org/10.1080/15384101.2022.2155016.

(247) Giunta, S.; D'Amico, A. G.; Maugeri, G.; Bucolo, C.; Romano, G. L.; Rossi, S.; Eandi, C. M.; Pricoco, E.; D'Agata, V. Drug-Repurposing Strategy for Dimethyl Fumarate. *Pharmaceuticals* **2023**, *16* (7), 974. https://doi.org/10.3390/ph16070974.

(248) Silva, A.; Pereira, M.; Carrascal, M. A.; Brites, G.; Neves, B.; Moreira, P.; Resende, R.; Silva, M. M.; Santos, A. E.; Pereira, C.; Cruz, M. T. Calcium Modulation, Anti-Oxidant and Anti-Inflammatory Effect of Skin Allergens Targeting the Nrf2 Signaling Pathway in Alzheimer's Disease Cellular Models. *IJMS* **2020**, *21* (20), 7791. https://doi.org/10.3390/ijms21207791.

(249) Bennett Saidu, N. E.; Bretagne, M.; Mansuet, A. L.; Just, P.-A.; Leroy, K.; Cerles, O.; Chouzenoux, S.; Nicco, C.; Damotte, D.; Alifano, M.; Borghese, B.; Goldwasser, F.; Batteux, F.; Alexandre, J. Dimethyl Fumarate Is Highly Cytotoxic in KRAS Mutated Cancer Cells but Spares Non-Tumorigenic Cells. *Oncotarget* **2018**, *9* (10), 9088–9099. https://doi.org/10.18632/oncotarget.24144.

(250) Troup, R. I.; Fallan, C.; Baud, M. G. J. Current Strategies for the Design of PROTAC Linkers: A Critical Review. *Exploration of Targeted Anti-tumor Therapy* **2020**, *1* (5). https://doi.org/10.37349/etat.2020.00018.

(251) Ishida, T.; Ciulli, A. E3 Ligase Ligands for PROTACs: How They Were Found and How to Discover New Ones. *SLAS Discovery* **2021**, *26* (4), 484–502. https://doi.org/10.1177/2472555220965528.

(252) Lu, M.; Ji, J.; Lv, Y.; Zhao, J.; Liu, Y.; Jiao, Q.; Liu, T.; Mou, Y.; You, Q.; Jiang, Z. Bivalent Inhibitors of the BTB E3 Ligase KEAP1 Enable Instant NRF2 Activation to Suppress Acute Inflammatory Response. *Cell Chemical Biology* **2024**, *31* (6), 1188-1202.e10. https://doi.org/10.1016/j.chembiol.2023.12.005.

(253) Zografou-Barredo, N. A.; Hallatt, A. J.; Goujon-Ricci, J.; Cano, C. A Beginner's Guide to Current Synthetic Linker Strategies towards VHL-Recruiting PROTACs. *Bioorganic & Medicinal Chemistry* **2023**, *88–89*, 117334. https://doi.org/10.1016/j.bmc.2023.117334.

(254) Liu, X.-W.; Shi, J.-L.; Yan, J.-X.; Wei, J.-B.; Peng, K.; Dai, L.; Li, C.-G.; Wang, B.-Q.; Shi, Z.-J. Reigoselective Arylation of Thiazole Derivatives at 5-Position via Pd Catalysis under Ligand-Free Conditions. *Org. Lett.* **2013**, *15* (22), 5774–5777. https://doi.org/10.1021/ol4027073.

(255) Berlin, M.; Cantley, J.; Bookbinder, M.; Bortolon, E.; Broccatelli, F.; Cadelina, G.; Chan, E. W.; Chen, H.; Chen, X.; Cheng, Y.; Cheung, T. K.; Davenport, K.; DiNicola, D.;

Gordon, D.; Hamman, B. D.; Harbin, A.; Haskell, R.; He, M.; Hole, A. J.; Januario, T.; Kerry, P. S.; Koenig, S. G.; Li, L.; Merchant, M.; Pérez-Dorado, I.; Pizzano, J.; Quinn, C.; Rose, C. M.; Rousseau, E.; Soto, L.; Staben, L. R.; Sun, H.; Tian, Q.; Wang, J.; Wang, W.; Ye, C. S.; Ye, X.; Zhang, P.; Zhou, Y.; Yauch, R.; Dragovich, P. S. PROTACs Targeting BRM (SMARCA2) Afford Selective *In Vivo* Degradation over BRG1 (SMARCA4) and Are Active in BRG1 Mutant Xenograft Tumor Models. *J. Med. Chem.* **2024**, *67* (2), 1262–1313. https://doi.org/10.1021/acs.jmedchem.3c01781.

(256) Siokatas, C.; Lampropoulou, A.; Smina, A.; Soupsana, K.; Kontostathi, M.; Karra, A.-V.; Karampelas, T.; Politou, A. S.; Christoforidis, S.; Tamvakopoulos, C.; Sarli, V. Developing MYC Degraders Bearing the Von Hippel–Lindau Ligand to Target the “Undruggable” MYC. *ACS Pharmacol. Transl. Sci.* **2024**, *7* (12), 3955–3968. https://doi.org/10.1021/acsptsci.4c00452.

(257) Chiang, S.-K.; Chen, S.-E.; Chang, L.-C. The Role of HO-1 and Its Crosstalk with Oxidative Stress in Cancer Cell Survival. *Cells* **2021**, *10* (9), 2401. https://doi.org/10.3390/cells10092401.

(258) Zhao, J.; Yan, S.; Ma, X.; Song, Y.; Pan, Y. Nrf2 Regulates the Activation of THP-1 Cells Induced by Chloral Hydrate. *Ecotoxicology and Environmental Safety* **2023**, *256*, 114841. https://doi.org/10.1016/j.ecoenv.2023.114841.

(259) Liu, X.; Zhang, X.; Lv, D.; Yuan, Y.; Zheng, G.; Zhou, D. Assays and Technologies for Developing Proteolysis Targeting Chimera Degraders. *Future Med. Chem.* **2020**, *12* (12), 1155–1179. https://doi.org/10.4155/fmc-2020-0073.